PASSIVE WIRELESS SURFACE ACOUSTIC WAVE SENSORS FOR MONITORING SEQUESTRATION SITES CO_2 EMISSION

FINAL TECHNICAL REPORT

PROJECT PERFORMANCE PERIOD: December 1, 2009 – November 30, 2012

SUBMITTED BY

Yizhong Wang
Minking K. Chyu
Qing-Ming Wang

REPORT SUBMITTAL DATE: February 14, 2013

DEPARTMENT OF MECHANICAL ENGINEERING AND MATERIALS SCIENCE
617 BENEDUM HALL 3700 OHARA STREET
PITTSBURGH, PA 15261

PREPARED FOR

U.S. DEPARTMENT OF ENERGY
NATIONAL ENERGY TECHNOLOGY LABORATORY
PITTSBURGH, PENNSYLVANIA 15236
(DOE AWARD NO. DE-FE0002138)

DISCLAIMER

ABSTRACT

University of Pittsburgh's Transducer lab has teamed with the U.S. Department of Energy's National Energy Technology Laboratory (DOE NETL) to conduct a comprehensive study to develop/evaluate low-cost, efficient CO_2 measuring technologies for geological sequestration sites leakage monitoring.

A passive wireless CO_2 sensing system based on surface acoustic wave technology and carbon nanotube nanocomposite was developed. Surface acoustic wave device was studied to determine the optimum parameters. Delay line structure was adopted as basic sensor structure. CNT polymer nanocomposite was fabricated and tested under different temperature and strain condition for natural environment impact evaluation. Nanocomposite resistance increased for 5 times under pure strain, while the temperature dependence of resistance for CNT solely was -1375ppm/℃. The overall effect of temperature on nanocomposite resistance was -1000ppm/℃. The gas response of the nanocomposite was about 10% resistance increase under pure CO_2. The sensor frequency change was around 300ppm for pure CO_2. With paralyne packaging, the sensor frequency change from relative humidity of 0% to 100% at room temperature decreased from over 1000ppm to less than 100ppm. The lowest detection limit of the sensor is 1% gas concentration, with 36ppm frequency change. Wireless module was tested and showed over one foot transmission distance at preferred parallel orientation.

TABLE OF CONTENTS

ABSTRACT III
TABLE OF CONTENTS IV
LIST OF FIGURES VI
LIST OF TABLES X
LIST OF EQUATIONS X
EXECUTIVE SUMMARY 1
1.0 INTRODUCTION 3
1.1 Motivations 3
1.2 Research Objectives 5
1.2.1 Task 1 5
1.2.2 Task 2 6
1.2.3 Task 3 6
2.0 BACKGROUND 8
2.1 Carbon Dioxide Sequestration 8
2.2 Carbon Dioxide Sensor 9
2.2.1 NDIR CO_2 Sensor 9
2.2.2 Chemical CO_2 Sensor 11
2.3 Surface Acoustic Wave (SAW) Sensor 12
2.4 Carbon Nanotubes (CNTs) 14
2.4.1 Types of CNTs 14
2.4.2 Fabrication of CNTs 16
2.5 Gas Sensing Nanocomposites 16
2.4.1 Nanocomposites 16
2.4.2 CNT nanocomposite sensor 17
3.0 FABRICATION AND CHARACTERIZATION OF SAW FLOW SENSOR 18
3.1 Background 18
3.2 Theoretical Analysis 19
3.2.1 Pressure on Chamber Induced by Flow 19
3.2.2 Initial Deformation of the Resonator 21
3.2.3 The unperturbed SAW mode 23
3.2.4 Frequency shift on pre-stressed substrate 24
3.3 Surface Acoustic Wave Sensor Design 25
3.3.1 Piezoelectric Substrate Material 25
3.3.2 Design of the SAW sensor 26
3.3.3 Design and fabrication of the testing system 29
3.4 Experiment Results and Conclusion 31
4.0 CNT NANOCOMPOSITE FABRICATION AND CHARACTERIZATION 34
4.1 Introduction 34

4.2 Fabrication of CNT nanocomposite and Percolation Threshold Study 35
4.2.1 Fabrication of CNT Nanocomposite 36
4.2.2 CNT Nanocomposite Percolation Threshold 36
4.3 CNT Nanocomposite Response to Temperature Change 40
4.4 CNT Nanocomposite Response to Strain 48
4.4.1 Test Preparation 48
4.4.2 Impedance Measurements 49
4.4.3 DC Gauge Factor Test Results 53
4.4.4 Impedance Parameters Gauge Factor Test Results 55
4.4.5 Gauge Factor Summary 58
4.4.6 Experiment Discussion 58
4.5 Conclusion 59
5.0 NANOCOMPOSITE CO_2 RESPONSE AND SAW CO_2 SENSOR PERFORMANCE 61
5.1 Introduction 61
5.2 Gas Testing Platform Construction and Improvement 61
5.3 SAW CO2 Sensor Assessment 65
5.4 CNT-PI Nanocomposite Response to CO_2 70
5.4.1 Nanocomposite Fabrication 70
5.4.2 Nanocomposite Gas Response 70
5.4.3 Nanocomposite Gas Response Improvement 74
5.5 SAW Sensor CO_2 Response Assessment and Characterization 77
5.5.1 SAW Sensor Performance Assessment 77
5.5.2 SAW Sensor Fabrication 78
5.5.3 SAW Sensor Performance Test Results 81
5.6 SAW Sensor Packaging 82
5.6.1 Humidity Impact on SAW Sensor Performance 82
5.6.2 Parylene Packaging for SAW Sensor 88
5.7 Conclusion 92
6.0 WIRELESS SENSING MODULE DESIGN AND CHARACTERIZATION 93
6.1 Introduction 93
6.2 Antenna Design 95
6.3 Antenna Construction 95
6.4 Antenna Characterization 97
6.5 Conclusion 106
7.0 Conclusions 107
8.0 REFERENCES 109

LIST OF FIGURES

Figure 2. 1 (a) Breakdown of CO_2 emission sources in the U.S. in 2006. (b) CO_2 emission by sectors in the U.S. in 2006. 8
Figure 2. 2 CO_2 storage. 9
Figure 2. 3 Typical NDIR CO_2 sensor structure. 10
Figure 2. 4 Response of Micro balance type CO_2 sensor with (a) 65nm (b) 62nm PAPO coating. 11
Figure 2. 5 Structure of capacitor type CO_2 sensor. 12
Figure 2. 6 Structure of SAW sensor. 13
Figure 2. 7 Typical swCNT structure. (a) Armchair (n, n). (b) Zigzag (n, 0). (c) Chiral (n, m). 15
Figure 2. 8 Typical three layer mwCNT with armchair structure. 16
Figure 3. 1 Pressure Driven Laminar Flow Schematic View. 19
Figure 3. 2 (a) Two plate Couette problem. (b) Short Segment of flow chamber under pressure and dragging force. 20
Figure 3. 3 (a) Bending moment distribution in the unit length of the free body diagram of the resonator in X_3 direction. (b) Approximated uniform bending moment distribution. 22
Figure 3. 4 SAWs propagating along top surface of an elastic half space 23
Figure 3. 5 Theoretical relative error of neglecting the shear stress (a) Error at 10kPa. (b) Error at 40kPa. 28
Figure 3. 6 FEM results about ST-X cut substrate under pressure. (a) Deformation under 10kPa pressure. (b) Strain S_{11} under 10kPa pressure. (c) Strain S_{11} of half plate under 20kPa pressure. 28
Figure 3. 7 The strain S_{11} on the central line of plate bottom from simulation and calculation. (a) FEM result for 20mm × 20mm × 0.3mm sensor. (b) Calculation results for 20mm × 20mm × 0.3mm and 30mm × 30mm × 0.3mm sensors. 28
Figure 3. 8 (a) Simulated and calculated phase change versus flow rate of the chamber. (b) Simulated and calculated frequency shift versus flow rates of the chamber 29
Figure 3. 9 The dimension of chamber 30
Figure 3. 10 (a) Designed SAW sensor with 15um IDT finger and space. (b) Fabricated SAW sensor on 3cm × 3cm quartz crystal substrate. 31
Figure 3. 11 (a) Crosessetional view of the designed experiment setup. (b) Integrated experiment setup. 31
Figure 3. 12 SAW flow sensor reponse. 32
Figure 4. 1. Some of the regular and Archimedean lattices. 37
Figure 4. 2 Impedance spectroscopy of some CNT-Polyimide nanocomposite thin films with different weight ratios. 38
Figure 4. 3 Volume resistivity of nanocomposite thin film with respect to weight ratio. 39
Figure 4. 4 Volume conductivity of nanocomposite thin film with respect to weight ratio. 39
Figure 4. 5 Volume conductivity of CNT-polymer nanocomposite with respect to weight ratio from literature. 40
Figure 4. 6 Impedance of swCNT-polyimide composites(0%swcnt) at different temperature 41

Figure 4. 7 Impedance of swcnt-polyimide composites(0.02%swcnt) at different temperature 42
Figure 4. 8 Impedance of swcnt-polyimide composites(0.05%swcnt) at different temperature 42
Figure 4. 9 Impedance of swcnt-polyimide composites(0.07%swcnt) at different temperature 42
Figure 4. 10 Impedance of swcnt-polyimide composites(0.1%swcnt) at different temperature 43
Figure 4. 11 Impedance of swcnt-polyimide composites(0.2%swcnt) at different temperature 43
Figure 4. 12 Impedance of swcnt-polyimide composites(0.35%swcnt) at different temperature 43
Figure 4. 13 Impedance of swcnt-polyimide composites(0.6%swcnt) at different temperature 44
Figure 4. 14 Impedance of swcnt-polyimide composites(0.7%swcnt) at different temperature 44
Figure 4. 15 Impedance of swcnt-polyimide composites(0.8%swcnt) at different temperature 45
Figure 4. 16 Impedance of swcnt-polyimide composites(1%swcnt) at different temperature 45
Figure 4. 17 Impedance of swcnt-polyimide composites(1.1%swcnt) at different temperature 46
Figure 4. 18 Impedance of swCNT-polyimide composites(1.2%swCNT) at different temperature 46
Figure 4. 19 Equivalent circuit of the swCNT nanocomposite thin film..... 46
Figure 4. 20 Resistance change with temperature for nanocomposites with different CNT concentration. 47
Figure 4. 21 Temperature Coefficient for nanocomposites with different CNT concentration..... 48
Figure 4. 22 Stress Strain testing apparatus..... 49
Figure 4. 23 Test sample. (a) without IDT. (b) with IDT, top one with nanocomposite, bottom one no nanocomposite. 49
Figure 4. 24 Impedance of test sample without IDT, and with CNT concentration of 0.8%. 50
Figure 4. 25 Impedance of test sample without IDT, and with CNT concentration of 1.1%. 50
Figure 4. 26 Impedance of test sample without IDT, and with CNT concentration of 1.4%. 51
Figure 4. 27 Impedance of test sample without IDT, and with CNT concentration of 1.7%. 51
Figure 4. 28 Impedance of test sample without IDT, and with CNT concentration of 2%. 51
Figure 4. 29 Impedance of test sample with IDT, and with CNT concentration of 1.1%. 52
Figure 4. 30 Impedance of test sample with IDT, and with CNT concentration of 1.4%. 52
Figure 4. 31 Impedance of test sample with IDT, and with CNT concentration of 1.7%. 52
Figure 4. 32 Impedance of test sample with IDT, and with CNT concentration of 2%. 53
Figure 4. 33 Gauge factor experiment results for test samples without IDT, the trend line equations are for concentrations of 0.8%, 1.1%, 1.4%, 1.7% and 2% from top to bottom. 54
Figure 4. 34 Gauge factor experiment results for test samples with IDT, the trend line equations are for concentrations of 1.1%, 1.4%, 1.7% and 2% from top to bottom. 54
Figure 4. 35 Gauge factor comparison between two types of test samples. 55
Figure 4. 36 Resistance Gauge factor from impedance measurements for samples without IDTs. 56
Figure 4. 37 Capacitance Gauge factor from impedance measurements for samples without IDTs. ... 56
Figure 4. 38 Resistance Gauge factor from impedance measurements for samples with IDTs. 57
Figure 4. 39 Capacitance Gauge factor from impedance measurements for samples with IDTs. 57
Figure 4. 40 Gauge Factor summary. 58
Figure 4. 41 Strain Sensor Working Mechanism. 59
Figure 5. 1 Gas testing system schematic view. 62
Figure 5. 2 Keithley 238 current source measurement unit. 62

Figure 5. 3 Labview interface for automatic data collection. 63
Figure 5. 4 Gas testing system with automatic data collection. (a) System overview. (b) Test sample. 63
Figure 5. 5 Supplemental testing chamber for faster response. 65
Figure 5. 6 SAW frequency shift corresponding to the thin film conductivity. 69
Figure 5. 7 Volume Conductivity of nanocomposite with different CNT concentration. 69
Figure 5. 8 Real time CO_2 response .for nanocomposite thin film with 0.8wt% CNT concentration.. 71
Figure 5. 9 Real time CO_2 response .for nanocomposite thin film with 1.1wt% CNT concentration.. 71
Figure 5. 10 Real time CO_2 response .for nanocomposite thin film with 1.4wt% CNT concentration.71
Figure 5. 11 Real time CO_2 response .for nanocomposite thin film with 1.7wt% CNT concentration.72
Figure 5. 12 Real time CO_2 response .for nanocomposite thin film with 2wt% CNT concentration... 72
Figure 5. 13 Relative resistivity change of nanocomposite thin films. 72
Figure 5. 14 Relative resistivity change of CNT-PI nanocomposite thin films with 1.1% CNT 73
Figure 5. 15 Relative resistivity change of CNT-PEI nanocomposite thin films with 1.4% CNT and 0.5% corn starch 75
Figure 5. 16 Relative resistivity change of CNT-PEI nanocomposite thin films with 1.4% CNT and 0.8% corn starch 75
Figure 5. 17 Relative resistivity change of CNT-PEI nanocomposite thin films with 1.4% CNT with 1% potato starch 75
Figure 5. 18 Relative resistivity change of CNT-PEI nanocomposite thin films with 1.4% CNT 76
Figure 5. 19 Relative resistivity change of CNT-PEI nanocomposite thin films with 1.4% CNT 76
Figure 5. 20 SAW frequency shift prediction at different CO_2 concentration. 77
Figure 5. 21 SAW frequency shift prediction at different CO_2 concentration in log scale. 78
Figure 5. 22 (a) $LiNbO_3$ substrate right after patterning. (b) LiNbO3 substrate after gold etching and RIE cleaning. 79
Figure 5. 23 IDT after shadow mask process. 80
Figure 5. 24 (a) $LiNbO_3$ sensor from photo lithography process. (b) $LiNbO_3$ sensor from shadow mask process. 80
Figure 5. 25 Sensor Response in linear scale. 81
Figure 5. 26 Sensor Response in log scale. 82
Figure 5. 27 Sensor Response to humidity. 84
Figure 5. 28 Sensor Response at dry air with 0%RH. 85
Figure 5. 29 Sensor Response 11.3%RH. 85
Figure 5. 30 Sensor Response 31%RH. 86
Figure 5. 31 Sensor Response 32.8%RH. 86
Figure 5. 32 Sensor Response 57.6%RH. 87
Figure 5. 33 Sensor Response 75.3%RH. 87
Figure 5. 34 Sensor Response 84.3%RH. 88
Figure 5. 35 Sensor Response 97.3%RH. 88
Figure 5. 36 SAW Sensor Humidity Response comparison after Parylene Coating. 89
Figure 5. 37 Coated SAW Sensor gas response in linear scale. 90

Figure 5. 38 Coated SAW Sensor gas response in log scale. 90
Figure 5. 39 SAW Sensor gas response comparison after coating in linear scale. 91
Figure 5. 40 SAW Sensor gas response comparison after coating in log scale. 91
Figure 6. 1 Typical onchip antenna with simplified structure 93
Figure 6. 2 Integrated Antenna surrounding the sensor. 94
Figure 6. 3 On chip Antenna outside of the sensor. 94
Figure 6. 4 Basic Sensor response of the sample sensor with wireless module (wireless module not connected). 96
Figure 6. 5 Sample sensor connected with wireless module under measurement. 97
Figure 6. 6 Antenna consisting a double-coil and capacitor. 97
Figure 6. 7 Antenna testing circumstances. (A) in series. (B) in parallel. 97
Figure 6. 8 Sensor response with antenna in series configuration at 0mm distance. 98
Figure 6. 9 Sensor response with antenna in series configuration at 5mm distance. 98
Figure 6. 10 Sensor response with antenna in series configuration at 10mm distance. 99
Figure 6. 11 Sensor response with antenna in series configuration at 15mm distance. 99
Figure 6. 12 Sensor response with antenna in parallel configuration at 0mm distance. 100
Figure 6. 13 Sensor response with antenna in parallel configuration at 5mm distance. 100
Figure 6. 14 Sensor response with antenna in parallel configuration at 10mm distance. 101
Figure 6. 15 Sensor response with antenna in parallel configuration at 15mm distance. 101
Figure 6. 16 Sensor response with antenna in parallel configuration at 20mm distance. 102
Figure 6. 17 Sensor response with antenna in parallel configuration at 25mm distance. 102
Figure 6. 18 Sensor response with antenna in parallel configuration at 30mm distance. 103
Figure 6. 19 Sensor response with antenna in parallel configuration at 35mm distance. 103
Figure 6. 20 Sensor response with antenna in parallel configuration at 40mm distance. 104
Figure 6. 21 Sensor response with antenna in parallel configuration at 45mm distance. 104
Figure 6. 22 Sensor response with antenna in parallel configuration at 50mm distance. 105
Figure 6. 23 Antenna performance summary. 105

LIST OF TABLES

Table 2. 1 Common used Piezoelectric Material Properties. 14
Table 5. 1 Relative Humidity of enclosed container with saturated solutions in different temperatures (from Omega). 83
Table 5. 2 Solubility for different salt at different temperature. 83
Table 5. 3 Solution heat and Temperature increase during saturated solution preparation process. 84

LIST OF EQUATIONS

$\Delta f = -C_f (f_0^2 / A)\Delta m$ **Eq. 2. 1**..... 11

-NH_2 + CO_2 + H_2O ↔ -$NH_4^+HCO_3$- **Eq. 2. 2** 12

$$\frac{\Delta\phi}{\phi} = \kappa\left[\underbrace{c_m f_0 \Delta\rho_s}_{mass} + \underbrace{\frac{K^2}{2}\Delta\left(\frac{\sigma_s^2}{\sigma_s^2 + \nu_0^2 C_s^2}\right)}_{conductivity}\right]$$ **Eq. 2. 3**..... 13

$$\frac{\Delta\alpha}{k} = \kappa\frac{K^2}{2}\Delta\left(\frac{\nu_0 C_s \sigma_s}{\sigma_s^2 + \nu_0^2 C_s^2}\right)$$ **Eq. 2. 4** 13

$$d = \frac{a}{\pi}\sqrt{(n^2 + nm + m^2)}$$ **Eq. 2. 5** 15

$$v = V\left(1 - \frac{4y^2}{H^2}\right),$$ **Eq. 3. 1** 20

$$V = -\frac{H^2}{8\mu}\frac{dp}{dx}$$ **Eq. 3. 2**..... 21

$$v = -\frac{1}{2\mu}\frac{dp}{dx}\left(\frac{H^2}{4} - y^2\right)$$ **Eq. 3. 3** 21

$$v = V\left(1 - \frac{4y^2}{H^2}\right), \quad V = \frac{p_0 H^2}{8\mu L}$$ **Eq. 3. 4**..... 21

The flow rate: $$Q=\frac{2VHB}{3}=\frac{p_0H^3B}{12\mu L}$$ **Eq. 3. 5** 21

pressure: $$\sigma_{xx}=\sigma_{yy}=-p(x)=-p_0(L-x)/L-p_1$$ **Eq. 3. 6** 21

shear stress: $$\tau_{xy}=-\tau_0 y,\quad \tau_0=\frac{p_0}{L}$$ **Eq. 3. 7** 21

$$\bar{c}_{11}Aw_{1,1}^{(0)}=N_A-\tau X_1$$
$$\bar{c}_{11}Iw_{2,11}^{(0)}=M$$
Eq. 3. 8 22

$$w_1^{(0)}(0)=0,\ \ w_1^{(0)}(l)=0,$$
$$w_2^{(0)}(0)=0,\ w_2^{(0)}(l)=0,\ w_{2,1}^{(0)}(0)=0,\ w_{2,1}^{(0)}(l)=0$$
Eq. 3. 9 22

$$w_1^{(0)}(X_1)=\frac{\tau(l-X_1)X_1}{2\bar{c}_{11}A}=\frac{\tau(l-X_1)X_1}{2\bar{c}_{11}h},$$
$$w_{2,1}^{(0)}(X_1)=-\frac{pX_1(l-X_1)(l-2X_1)}{12\bar{c}_{11}I}=-\frac{pX_1(l-X_1)(l-2X_1)}{\bar{c}_{11}h^3},$$
$$w_2^{(0)}(X_1)=-\frac{pX_1^2(l-X_1)^2}{24\bar{c}_{11}I}=-\frac{pX_1^2(l-X_1)^2}{2\bar{c}_{11}h^3}$$
Eq. 3. 10 22

$$w_1(X_1)\cong w_1^{(0)}(X_1)-X_2w_{2,1}^{(0)}(X_1),$$
$$w_2(X_1)\cong w_2^{(0)}(X_1),$$
$$w_3(X_1)\cong 0.$$
Eq. 3. 11 23

$$\begin{cases} u_1=\exp(-2\pi\beta\overline{X}_2/\lambda_R)\cos\left(2\pi g\dfrac{\overline{X}_2}{\lambda_R}+\alpha\right)\cos\left[\omega\left(t-\dfrac{\overline{X}_1}{C_R}\right)-\alpha\right] \\ u_2=-r\exp(-2\pi\beta\overline{X}_2/\lambda_R)\cos\left(2\pi g\dfrac{\overline{X}_2}{\lambda_R}+\alpha\right)\sin\left[\omega\left(t-\dfrac{\overline{X}_1}{C_R}\right)-\alpha\right] \end{cases}$$
Eq. 3. 12 24

$$\frac{\Delta\omega}{\omega}\cong\frac{1}{2\omega^2}\frac{\int_V\hat{c}_{K\alpha L\gamma}u_{\alpha,K}u_{\gamma,L}dV}{\int_V\rho_0u_\alpha u_\alpha dV}$$
Eq. 3. 13 24

$$\hat{c}_{K\alpha L\gamma}=T_{KL}^0\delta_{\alpha\gamma}+c_{K\alpha LN}w_{\gamma,N}+c_{KML\gamma}w_{\alpha,M}+c_{K\alpha L\gamma AB}S_{AB}^0$$
Eq. 3. 14 25

$$S_{11}\big|_{X_2=-\frac{h}{2}}=w_{1,1}=\frac{p_0H(l-2X_1)}{4\bar{c}_{11}hL}-\frac{\left(\dfrac{p_0}{2}+p_1\right)\left(l^2-6lX_1+6X_1^2\right)}{2\bar{c}_{11}h^2}$$
Eq. 3. 15 27

$$S_{11}\big|_{X_2=-\frac{h}{2}} = S'_{11}\big|_{X_2=-\frac{h}{2}} + S''_{11}\big|_{X_2=-\frac{h}{2}} \approx S''_{11}\big|_{X_2=-\frac{h}{2}} = -\frac{\left(\frac{p_0}{2}+p_1\right)\left(l^2-6lX_1+6X_1^2\right)}{2\bar{c}_{11}h^2}$$ **Eq. 3. 16**

..... 27

$$\rho = R\frac{A}{\ell}$$ **Eq. 4. 1** 38

and

$$\sigma = \frac{1}{\rho}$$ **Eq. 4. 2** 38

$$\mathrm{Z} = \mathrm{R} + iX = Rs + (1/R_1 + i\omega C_1)^{-1} \text{ or } \mathrm{Z} = \left(R_s + \frac{R_1}{1+\omega^2 C_1{}^2 R_1^2}\right) - j\frac{\omega C R_1^2}{1+\omega^2 C_1{}^2 R_1{}^2}$$ **Eq. 4. 3**

..... 47

$$\phi(x,t) = \phi_0 e^{j(\omega t - kx)}$$ **Eq. 5. 1** 65

$$\phi_0(x) = \phi_0(0)e^{-\gamma x}$$ **Eq. 5. 2** 65

$$\frac{\partial J_x}{\partial x} = -\frac{\partial}{\partial t}\left(\frac{\rho_s}{d}\right)$$ **Eq. 5. 3** 65

$$\rho_s = \frac{kd}{\omega}J_x$$ **Eq. 5. 4** 66

$$J_x = \sigma E_x = -\frac{\partial}{\partial x}(\psi+\phi) = jk\sigma(\psi+\phi)$$ **Eq. 5. 5** 66

$$\psi = \frac{\rho_s}{C_s k} = \frac{\rho_s}{k(\varepsilon_0+\varepsilon_1)}$$ **Eq. 5. 6** 66

$$\rho_s = \frac{jk\sigma d(\varepsilon_0+\varepsilon_1)\phi}{v_0(\varepsilon_0+\varepsilon_1) - j\sigma d}$$ **Eq. 5. 7** 66

$$P_y = -\frac{\partial \rho_s}{\partial t}\frac{\phi_0}{2} = -\frac{j\omega\rho_s\phi_0}{2}$$ **Eq. 5. 8** 66

$$P_y = \frac{\omega k\sigma d(\varepsilon_0+\varepsilon_1)\phi_0{}^2}{2\left[v_0(\varepsilon_0+\varepsilon_1) - j\sigma d\right]}$$ **Eq. 5. 9** 67

$$Z_0 = \phi_0^{\,2} / P_x$$ **Eq. 5. 10** 67

$$U = \frac{P_x}{\omega v_0} = \frac{\phi_0^{\,2}}{2 Z_0 \omega v_0}$$ **Eq. 5. 11** 67

$$P_y = -v_0 \frac{\partial U}{\partial x} = -\frac{1}{\omega} \frac{\partial P_x}{\partial x}$$ **Eq. 5. 12** 67

$$P_y = -\frac{\phi_0}{Z_0 \omega} \frac{\partial \phi_0}{\partial x} = \frac{\gamma \phi_0^{\,2}}{Z_0 \omega}$$ **Eq. 5. 13** 67

$$K^2 = \frac{U_E}{U} = \frac{\frac{1}{2} k(\varepsilon_0 + \varepsilon_1) \phi_0^{\,2}}{P_x / \omega v_0} = Z_0 k(\varepsilon_0 + \varepsilon_1) \omega v_0$$ **Eq. 5. 14** 67

$$P_y = \frac{\gamma \phi_0^{\,2} k(\varepsilon_0 + \varepsilon_1) v_0}{K^2}$$ **Eq. 5. 15** 68

$$\frac{\Delta v}{v_0} \cong -\frac{\beta}{k} = -\frac{K^2}{2} \frac{(\sigma d)^2}{(\sigma d)^2 + v_0^{\,2} (\varepsilon_0 + \varepsilon_1)^2}$$ **Eq. 5. 16** 68

$$\frac{\alpha}{k} \cong \frac{K^2}{2} \frac{v_0 (\varepsilon_0 + \varepsilon_1) \sigma d}{(\sigma d)^2 + v_0^{\,2} (\varepsilon_0 + \varepsilon_1)^2}$$ **Eq. 5. 17** 68

$$\frac{\Delta v}{v_0} = \frac{1}{v_0} \left(\frac{\partial v}{\partial m} \Delta m + \frac{\partial v}{\partial c} \Delta c + \frac{\partial v}{\partial \sigma} \Delta \sigma + \frac{\partial v}{\partial \varepsilon} \Delta \varepsilon + \frac{\partial v}{\partial T} \Delta T + \frac{\partial v}{\partial p} \Delta p \right)$$ **Eq. 5. 18** 68

EXECUTIVE SUMMARY

Background

Global warming has long been hot topic since the past two decades. Rising sea levels, decreasing ice extent, among other unusual phenomena, are signs of the impact of global warming, with the confirmation of apparent average temperature increasing since the industrial revolution, especially during the recent years. Regulations are now developing upon the cost for emissions that can cause global warming, especially CO_2.

As one of the most economical solutions, collecting the CO_2 generated from power plants and dumping them into the mines and oil fields deep under ground, has attracted lots of attention. One of the concerns aroused is the security of the storage sites. There is urgent need for developing a sophisticated system that can monitor the ground leakage in those remote sites.

After surveying all available and possible means for CO_2 sensing, one can reach the conclusion that surface acoustic wave sensor equipped with on-chip sensitive layer is the best choice for low cost wireless monitoring of sequestration sites leakage monitoring with minimum power consumption.

Objectives

The overall goal of the proposed project was to develop low-cost, efficient wireless CO_2 monitoring system for remote sequestration sites. Toward that end, the following specific project objectives were set in concert with the U.S. DOE, for work that was performed in response to the above goal:

- Fabricate the SAW sensor and characterize the impact of different parameters on SAW performance
- Fabricate the CNT nanocomposite and characterize the impact of different parameters on nanocomposite response
- Evaluate the CNT nanocomposite gas response and characterize SAW sensor gas response
- Develop a novel CNT nanocomposite SAW sensor with wireless function

Work Scope

The basis for development of the passive wireless SAW CO_2 sensing system was to evaluate a number of components/processes with the potential to further increasing the sensitivity of the system, and to characterize other factors that might impact the system performance so that proper compensation can be made during the monitoring period.

Key tasks within the project are:

- Bench-scale analysis/characterization of SAW sensor
- Percolation threshold study and nanocomposite synthesis process development
- Analysis/characterization of temperature dependence of nanocomposite
- Analysis/characterization of strain dependence of nanocomposite

- Development of gas sensitive nanocomposite
- Evaluation of humidity on sensor performance and development of packaging method
- Wireless module development

Test Results

Bench-scale SAW sensor test results showed that under pressure induced bending SAW sensor delay time increased linearly with regard to the normal pressure, while the transmission loss did not changed accordingly.

Nanocomposite thin film fabrication process development suggested that the CNT network started to form at about 1.1wt%. It's observed that 24 hours ultrasound bath or one hour agitation with ultrasound mixer was need to evenly disperse the CNT powder into organic solvent.

Nanocomposite temperature study showed that the resistance of the thin film decrease by 1000ppm/℃ under increasing temperature up to 260℃.

Since the thermal expansion coefficients were different for the nanocomposite and the piezoelectric substrate, the strain effect on the thin film was also studied. Test results showed gauge factors around 5. Linked to the thermal expansion coefficients, it was seen that thermal induced strain caused an increasing resistance of about 375ppm/℃. It's concluded that pure temperature effect on CNT network is -1375ppm/℃.

Polyimide-CNT gas response was observed to be around 0.4% resistance increase for pure gas, which converted to 10ppm frequency change. PEI-Starch-CNT showed a stunning 20 times resistance increase and converted to over 1000ppm frequency change. Sensor gas tests suggested that the frequency change for pure gas is about 300ppm and the initial frequency change happened at 1% gas concentration.

Humidity test showed over 1000ppm frequency changed under saturated water vapor for the unprotected sensor. Parylene packaging proved to reduce the humidity response to less than 100ppm while maintaining the gas response of 300ppm for pure gas.

Wireless module was constructed and tested for different orientation. Test results implied best performance under parallel orientation and a transmission over one foot.

Overall Project Conclusions

The overall goal of the proposed project was to develop low-cost, efficient wireless CO_2 monitoring system for remote sequestration sites. Specific project goals have been met with the commensurate project achievement mentioned above. Overall, an efficient and low cost gas sensing system was developed. Processes for each component of the sensing system had been developed and fine tuned. Various factors on the sensor performance had been studied and the corresponding compensations were proposed for more accurate system calibration.

1.0 INTRODUCTION

1.1 Motivations

Global warming has been hot topic since early 1990s. The average global air and ocean temperature had been increasing over the last 100 years and become more severe in the last 30 years. Evidences show that the average temperature has increased over 0.8℃, 0.6℃ of the increase happened in the last three decades [1]. Global warming had a great impact on nature systems, ecology systems and even social systems. Rising sea levels and decreasing in snow and ice extent are consistent with global warming. Earlier timing of spring events, and pole ward and upward shifts in plant and animal ranges, are found to be related with high confidence to recent global warming [2]. The major causes of global warming include greenhouse gases, particulates and soot, and solar variation. Among them, greenhouse gases play an important role because greenhouse gases can greatly enhance the absorption and emission of infrared radiation, thus warming the lower atmosphere and surface of the earth. Greenhouse gases include water vapor, carbon dioxide (CO_2), methane and ozone.

CO_2 causes up to 26% of the greenhouse effect and the CO_2 concentration has been increasing for 36% since 1750 [3]. To reduce the concentration of CO_2 in the atmosphere, carbon sequestration, where CO_2 is captured and stored, is one of the most effective solutions. Currently, the captured CO_2 are stored in three ways: geological storage, where supercritical CO_2 is directly injected into underground geological formations, such as Oil fields, gas fields, saline formations, unmineable coal seams, and saline-filled basalt formations; ocean storage, including storing the CO_2 in solid clathrate hydrates that are already existing on the ocean floor; and mineral storage, where CO_2 reacted with available metal oxides, which in turn produces stable carbonates.

Most of the geological storage sites are in remote area, and the stored CO_2 is assumed to be in steady state for at least thousand years, so the possibility of CO_2 leakage is minimal and the consequence of CO_2 leakage is not supposed to be severe. However, it's still necessary to provide real time monitoring for sequestration sites ground and the injection holes. Since the power supply is limited on sites, passive wireless sensing with minimal power consumption is preferable.

For CO_2 sensing, there are two main principles, one is non dispersive infrared (NDIR) CO_2 sensors and the other is chemical sensors. For NDIR, the main components are an infrared source (lamp), a sample chamber or light tube, a wavelength sample chamber, and gas concentration is measured electro-optically by its absorption of a specific wavelength in the infrared (IR). The IR light is directed through the sample chamber towards the detector. In parallel there is another chamber with an enclosed reference gas, typically nitrogen. The detector has an optical filter in

front of it that eliminates all light except the wavelength that the selected gas molecules can absorb. Ideally other gas molecules do not absorb light at this wavelength, and do not affect the amount of light reaching the detector to compensate for interfering components [4]. NDIR is commonly used in industrial and civil applications, such as coal mines, office buildings. However, due to the nature of operation, the NDIR sensor consumes a lot of energy and can not be running as continuous sensor.

In the mean while, chemical CO_2 gas sensors with sensitive layers based on polymer or heteropolysiloxane have the principal advantage of very low energy consumption and can be reduced in size to fit into microelectronic-based systems [5]. Like any other gas sensor, the major functions in the CO_2 gas sensor are recognition of the CO_2 gas molecule and transduction of that recognition into a useful signal [6]. The recognition of CO_2 gas is essentially the reaction between the CO_2 gas and the sampling module of the sensor, such as aqueous solution or polymer membrane. The reaction produces a change in parameter such pH, resistance, conductivity, or capacitance based on the exchange of ion reactions between the analyte and surface material [7].

To construct a passive wireless sensing system, surface acoustic wave (SAW) sensor naturally becomes the first choice. SAW devices have a piezoelectric substrate excited by comb shape metal patterns called inter digital transducers (IDT). The IDTs convert incoming electrical signals into mechanical waves which propagate along the surface of the device. The space between the input and output IDTs is delay line. The SAW characteristics such as amplitude and frequency depend on the surface perturbations and have been used for sensing. It has been shown that temperature, pressure, mass deposition, conductivity change, elasticity change affect the propagation characteristics of the surface wave. Gas sensing has predominantly been achieved by mass-sensitive SAW sensors using gas absorption enhanced coatings. The mass change is observed as a frequency shift in an oscillator loop. However, the sensitivity is limited using this method. Conductivity change, on the other hand, can be more promising as a sensing parameter. Since the sensing process is induced by incoming signal, the SAW sensor can have zero power consumption when standby. And the incoming signal can be introduced wirelessly, thus further reduce the power needed for the system.

Since SAW is adopted, the gas recognition function needs to be solid state. There are many types of principles and materials including metal oxides, polymers, ceramics, or sol–gel [6]. In typical metal oxide type CO_2 sensor, CO_2 gas causes conductivity change on the film. However the sensing film is only sensitive in elevated temperature, which requires constant heating, thus unsuitable to be used in SAW sensor.

Polymer based nanomaterials and nanostructures have been hot topics due to their importance in basic scientific research and potential technology applications. Many nano-devices such as field-effect transistors, single-electron transistors, metal-semiconductor junctions, and intermolecular crossed junctions using nanowires or nanotubes have been demonstrated. It has

been shown that carbon nanotube (CNT) itself can have conductivity change in response to H_2 and NH_3 and some other strong gases. For weak gases such as CO_2, polymer can be mixed with CNTs to enhance the response. The mechanism is the polymer causes the gas to dissociate into charged ions or complexes, which results in the transfer of electrons, thus causes a conductance or resistance change of the surface layers when exposed to the analyte.

1.2 Research Objectives

The overall goal of this study is fabricating SAW sensor with wireless component, using CNT nanocomposite as sensing element, meanwhile, exploring the application of SAW sensor and CNT nanocomposites for multifunctional applications. Based on the overall goal, there are three main tasks in this study: (1) to fabricate the SAW sensor and characterize the impact of different parameters on SAW performance; (2) to fabricate the CNT nanocomposite and characterize the impact of different parameters on nanocomposite response; (3) to develop a novel CNT nanocomposite SAW sensor with wireless function.

1.2.1 Task 1: to fabricate the SAW sensor and characterize the impact of different parameters on SAW performance.

Specifically, SAW characteristic are studied during the construction of SAW flow sensor. The impact of the piezoelectric material properties on sensor performance, the effect of strain on sensor performance can all be assessed.

Fluid flow sensor has broad applications in various industrial and research operation monitoring and control. It is especially important to have accurate flow measurement in some aero-space technology applications and some of the cutting edge research projects.

For pressure driven laminar flow, the pipe wall is subject to pressure along the flow direction. The pressure on the wall decreases linearly towards the exit. When a sensor is mounted on the pipe wall, the sensor will also be subject to linearly decreased pressure. For sensor with small surface area compared to pipe dimension, the pressure can be assumed to be uniform.

Previous research showed that, for laminar flow, the pressure difference between specific point on pipe wall and flow exit depended linearly on flow rate. Since flow rate depends linearly on pressure, the flow meter essentially functions as a pressure sensor.

There has been some research on SAW pressure sensor design and fabrication. However, the fabricated sensor is based on $LiNbO_3$ and has two-layer chamber structure. Since $LiNbO_3$ is temperature dependant, the pressure sensor is unstable without proper temperature compensation.

The complicated two-layer structure also makes it unsuitable for flow sensor application.

ST-X cut quartz is selected for flow sensor due to its abundance and temperature stability. Plate structure is used for fabrication simplicity.

The results show linear relationship between the SAW delay time and flow rate, as predicted by simulation and theoretical calculation.

1.2.2 Task 2: to fabricate the CNT nanocomposite and characterize the impact of different parameters on nanocomposite response.

To fabricate CNT nanocomposite, the percolation threshold needs to be studied. CNT concentration lower than threshold might not be suitable for gas sensing, since the CNTs might not be interconnected to form a conducting network, thus the performance of the thin film might not be repeated.

Polyimde (PI) is the first choice in nanocomposite fabrication because of its resistance to harsh environment, especially high temperature, thus extending the sensor application range. Since the CO_2 sensor will be deployed in remote area so it is necessary to characterize the nanocomposite performance dependence on temperature. It is also know that piezoelectric material and polymer has different thermal expansion coefficient, so it is expected that at different temperature, the expansion of the SAW device and the nanocomposite on top will be different, thus causing certain strain and stress on the thin film. So it is also necessary to characterize the nanocomposite performance dependence on strain.

It's well known that humidity have an adverse effect on gas sensor performance. It's necessary to study the impact of humidity as well. When the humidity effect is too big to compensate, certain sensor packaging is recommended. Parylene is an ideal packaging material due to its low cost, easy coating process and high gas permeability. Test results confirmed that humidity have relatively minor effect after packaging at certain cost of gas sensing performance.

1.2.3 Task 3: to develop a novel CNT nanocomposite SAW sensor with wireless function.

The key part of SAW sensor development is to study the relationship between conductivity change and different CO_2 concentrations. To successfully characterize the gas response of nanocomposite, gas testing system is set up and modifications are made to improve the testing system performance.

Testing results show that the response of CNT-PI nanocomposite to CO_2 is not sensitive enough to

be used as sensing material. The conductivity only changed 0.4% for pure CO_2 compared to pure air. Thus for SAW sensing system with operating frequency of 52.6MHz, there will only be several hundred Hz change in resonant frequency when exposed to CO_2.

From chemistry point of view, CO_2 is generally not a reactive molecule, and only combines with primary and secondary amines at room temperature and atmosphere pressure to form carbonates, which is essentially an acid-base equilibrium. The best candidate with primary and secondary amines is Poly(ethyleneimine) (PEI), which is a highly branched polymer with 25% primary, 50% secondary and 25% tertiary amino groups. CNT-PEI nanocomposite is then mixed with starch to enhance the performance. Over 40 times performance improvement is observed.

Based on conductivity change of nanocomposite, the performance of SAW sensor can be estimated. Test results show that the SAW sensor performance is within reasonable range of prediction.

Since the gas sensing performance, especially the response time for the sensor, is affected by the parylene packaging, the detailed gas responses for both sensors with and without packaging are both studied. The test results show that packaging help reducing most of the impact of humidity without sacrificing the sensing performance. The packaged sensor has detection limit of 1%.

2.0 BACKGROUND

2.1 Carbon Dioxide Sequestration

As a major contributor for global warming, reducing the concentration of CO_2 is one of the best solutions. Generally the sources of the CO_2 in the Earth's atmosphere can be divided as two groups, naturally occurred CO_2 and human activity related CO_2. In the nature, the main source of CO_2 is animal respiration and ocean-atmosphere exchange. Since the industrial revolution 300 years ago, human activities have increased the CO_2 concentration in the air by 36%, to 390ppm. Fig. 2.1 shows the major CO_2 contributors in the U.S. [8]. Fossil fuel combustion is by far the largest source of CO_2 emissions, with 5,637.9 million tons CO_2 equivalent. The next largest source is non energy use of fuels, which accounts for 138 million tons CO_2 equivalent. The smallest source is Silicon Carbide Production and Consumption, which accounts for 0.2 million tons CO_2 equivalent. There is also a pie chart indicating that CO_2 represents the majority, 84.8%, of all greenhouse gas emissions in 2006 [8].

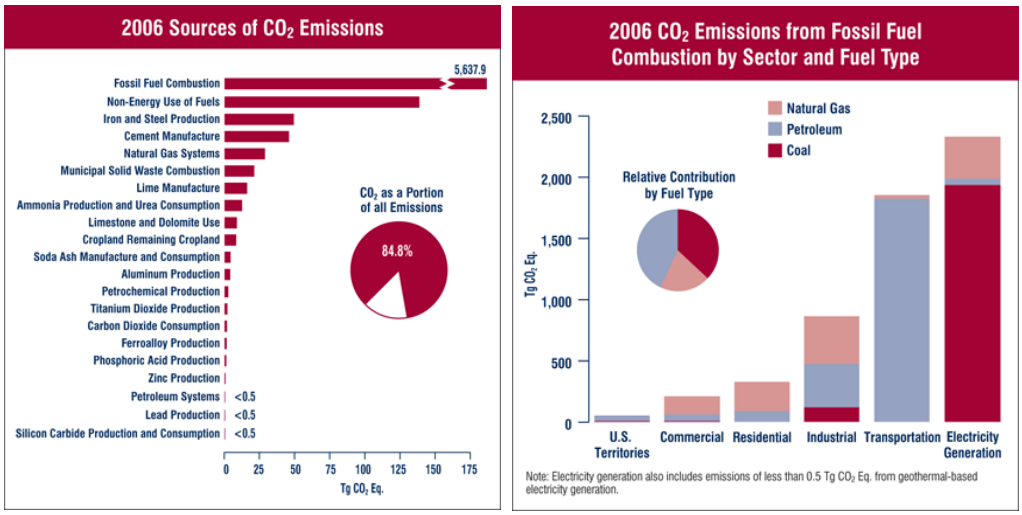

(a) (b)

Figure 2. 1 (a) Breakdown of CO_2 emission sources in the U.S. in 2006. (b) CO_2 emission by sectors in the U.S. in 2006.

To reduce the concentration of CO_2 in the atmosphere, one of the most important ways is CO_2 geological sequestration, by which CO_2 is captured and stored. Currently, the storage sites are mainly oil and gas production facilities, but storage in other types of reservoirs may increase in the future as technologies continue to develop. Fig. 2.2 shows the various ways of CO_2 storage [9]. The world wide geological sequestration capacity can hold up to 100 years CO_2 emissions for the whole world.

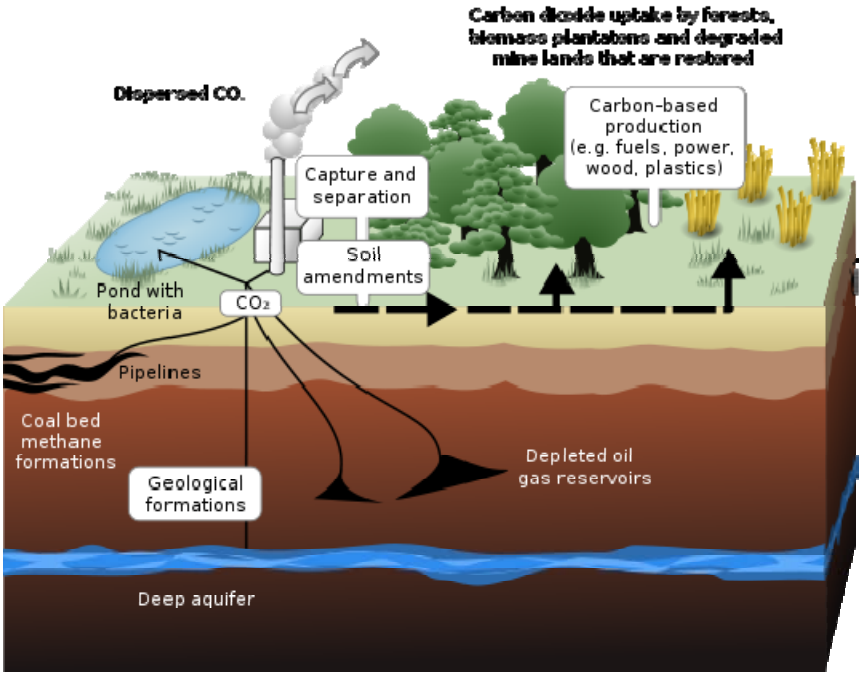

Figure 2. 2 CO_2 storage.

There are many on-going projects for geological sequestration worldwide, including the Midwest Geological Sequestration Consortium (MGSC) in Illinois, USA; Reggane, Algeria; Offshore Norway, the world's first industrial-scale CO_2-capture-and-storage (CCS) operation is under way at Statoil's Sleipner field in Sleipner, Norway; and Otway Basin, Australia [10]. Geological survey also suggests that within 50 miles of every coal-fire power plants-the biggest emission sources in U.S.-there is at least one candidate geological sequestration site.

2.2 Carbon Dioxide Sensor

A carbon dioxide sensor or CO_2 sensor is an instrument for the measurement of carbon dioxide gas. The most common principles for CO_2 sensors are non dispersive infrared gas sensors (NDIR) and chemical gas sensors. Measuring carbon dioxide is important in monitoring indoor air quality and many industrial processes [11].

2.2.1 NDIR CO_2 Sensor

NDIR sensors are commercially from various companies across the world. A typical NDIR sensor is shown in Fig. 2.3. [12].

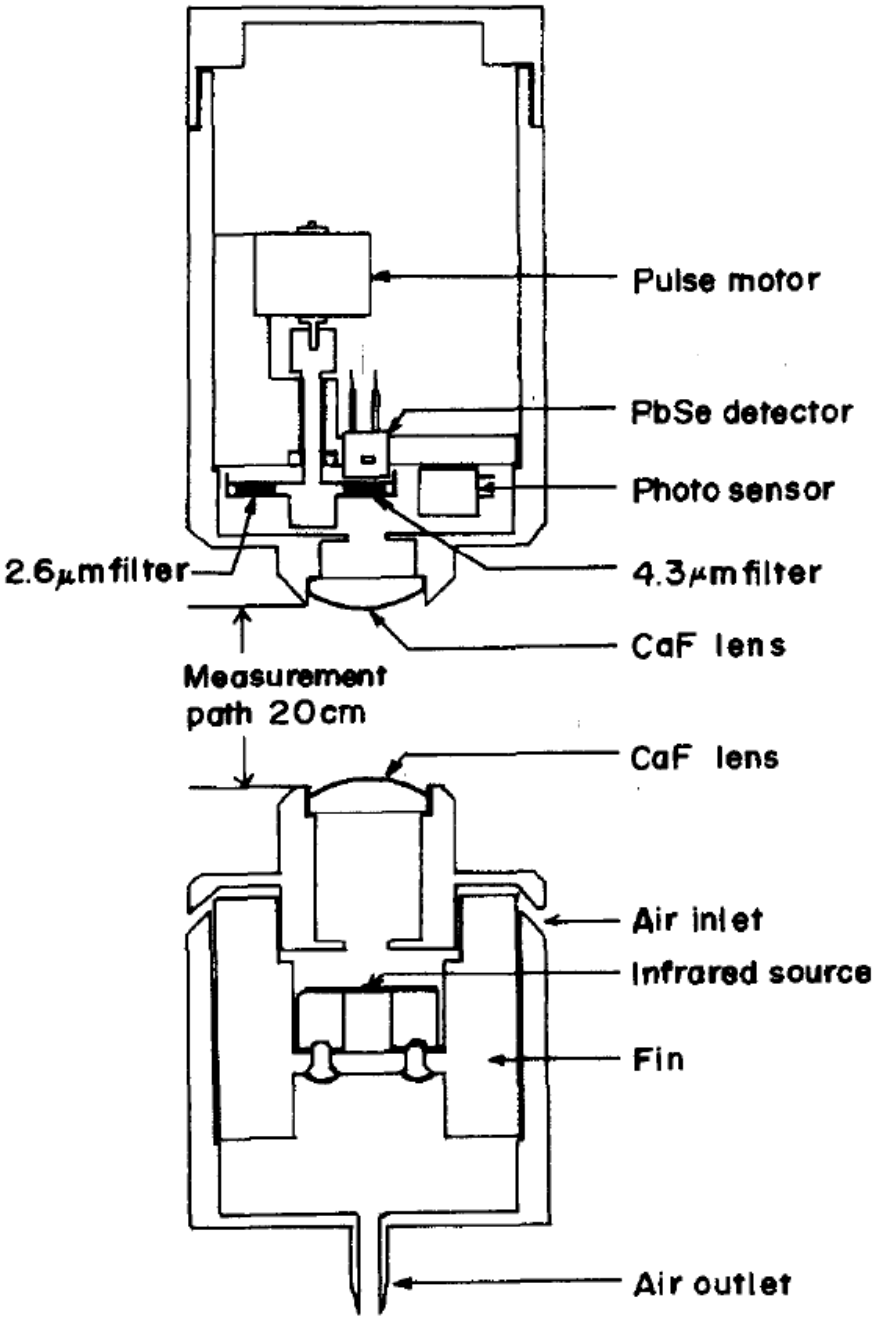

Figure 2. 3 Typical NDIR CO_2 sensor structure.

The broadband infrared radiation produced by the light source passes through a chamber filled with gas, generally methane or carbon dioxide. The gas absorbs radiation of a known wavelength and this absorption is a measure of the concentration of the gas. There is a narrow bandwidth optical filter at the end of the chamber to remove all other wavelengths before it is measured with a detector.

NDIR gas sensor is widely used in various industrial sites and civil applications, such as coal mines and office buildings. NDIR sensor is known as stable and precise detector. However it is not suitable to be used in geological sequestration sites due to its high power command, in the range of 1 watt [13], and difficulty in wireless integration.

2.2.2 Chemical CO_2 Sensor

Chemical CO_2 gas sensors with sensitive layers based on polymer- or heteropolysiloxane have the principal advantage of very low energy consumption and can be reduced in size to fit into microelectronic-based systems [11]. There are many types of chemical sensor available in past and ongoing researches.

2.2.2.1 Micro Balance Type CO2 Mass Sensor [14]

Quartz was used to build a micro balance with resonant frequency of 10MHz. Basically the sensors monitor changes in frequency (Δf) in the fundamental oscillation frequency upon ad/absorption of particles from the gas phase. To a first approximation the change Δf results in an increase in the oscillating mass Δm described by:

$$\Delta f = -C_f (f_0^2 / A)\Delta m \qquad \textbf{Eq. 2. 1}$$

Where A is the electrode surface, C_f is the mass sensitivity constant in our experiments (4.48 x 10^6 cm^2 s g^{-1}), and f_0 the fundamental frequency. This equation holds to a good approximation in the experiments as the maximum thickness of polymeric coatings was below 110 nm. The sensor was kept at 70℃ and so as the incoming test gas. Test results are shown in Fig.2.4.

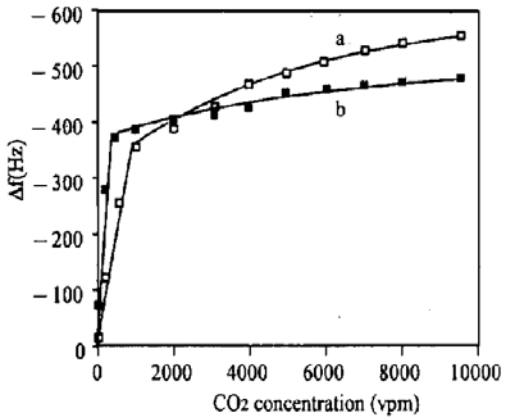

Figure 2. 4 Response of Micro balance type CO_2 sensor with (a) 65nm (b) 62nm PAPO coating.

The main disadvantage of this sensor is the operation of the sensor requires elevated temperature. The test results also shows saturation for gas concentration above 0.1 vol.%. Since the CO_2 concentration in the air is 390ppm, this sensor is not suitable for sequestration sites monitoring.

2.2.2.2 Capacitor Type CO_2 Sensor [15]

A mixture of 70% 3-aminopropyltrimethoxysiloxane (AMO) and 30% propy-ltrimethoxysilane (PTMS) is used as sensing material. The detection is based on the following detection reaction:

$$-NH_2 + CO_2 + H_2O \leftrightarrow -NH_4^+HCO_3- \quad \textbf{Eq. 2. 2}$$

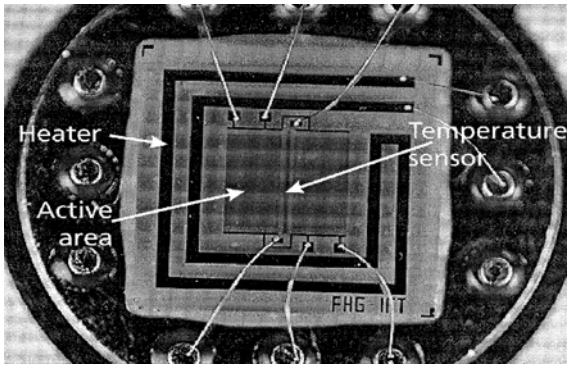

Figure 2. 5 Structure of capacitor type CO_2 sensor.

The reaction requires an energy of 120kJ/mol, so the sensor is equipped with a heater to maintain the operation temperature above 60℃. The measured capacitance of the sensing film shows a resolution of 10ppm.

2.2.2.3 Resistance Type CO2 Sensor [16-18]

Many chemical CO_2 sensors are based on resistance measurement. Many sensing materials have been used, including $BaTiO_3$–CuO [16], $BaCO_3$ [17], Ag_2SO_4 [18] and Na_2CO_3 [18]. Some of them can only be used at elevated temperature.

2.3 Surface Acoustic Wave (SAW) Sensor

SAWs were first explained in 1885 by Lord Rayleigh, who described the surface acoustic mode of propagation and predicted its properties in his classic paper [19]. Named after their discoverer, Rayleigh waves have a longitudinal and a vertical shear component that can couple with any media in contact with the surface. This coupling strongly affects the amplitude and velocity of the wave, allowing SAW sensors to directly sense mass and mechanical properties [20].

SAW devices have a piezoelectric substrate excited by comb shape metal patterns called inter digital transducers (IDT) as shown in Fig.2.6. The IDTs convert incoming electrical signals into mechanical waves which propagate along the surface of the device. The space between the input and output IDTs is delay line. The SAW characteristics such as amplitude and phase depend on the surface perturbations and have been used for sensing. It has been shown that temperature, pressure, mass deposition, conductivity change, elasticity change affect the propagation characteristics of the surface wave. Gas sensing has predominantly been achieved by mass-sensitive SAW sensors using gas absorption enhanced coatings. The mass change is observed as a frequency shift in an oscillator loop. However, the sensitivity is limited using this method. Conductivity change, on the other hand, can be more promising as a sensing parameter. Since the sensing process is induced by incoming signal, so the SAW sensor can have zero power consumption when standby. And the incoming signal can be introduced wirelessly, thus further reduce the power needed for the system.

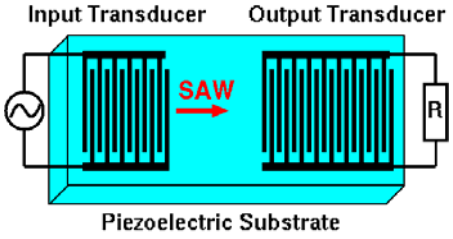

Figure 2. 6 Structure of SAW sensor.

The changes in phase, $\Delta\phi$ and attenuation, $\Delta\alpha$ of the surface acoustic wave can be given by

$$\frac{\Delta\phi}{\phi} = \kappa\left[\underbrace{c_m f_0 \Delta\rho_s}_{mass} + \underbrace{\frac{K^2}{2}\Delta\left(\frac{\sigma_s^2}{\sigma_s^2 + v_0^2 C_s^2}\right)}_{conductivity}\right] \qquad \textbf{Eq. 2. 3}$$

$$\frac{\Delta\alpha}{k} = \kappa\frac{K^2}{2}\Delta\left(\frac{v_0 C_s \sigma_s}{\sigma_s^2 + v_0^2 C_s^2}\right) \qquad \textbf{Eq. 2. 4}$$

Where c_m is the mass sensitivity coefficient, ρ_s is the mass per unit area, f_0 is the frequency of operation, K^2 is the electromechanical coupling coefficient, σ_s is the sheet conductivity of the film, C_s is the capacitance per length of the SAW substrate, κ is the fraction of the propagation path covered by the CNT film, and k is the wave number.

As for substrate materials, the properties of many common used piezoelectric materials are listed in table 2.1.

Table 2. 1 Common used Piezoelectric Material Properties.

Substrate	Cut	Propagate Direction	Wave Speed(m/s)	Coupling Coeff K^2 (%)	Temperature Coefficient (ppm/℃)	Transmission Loss(dB/cm)
Quartz	Y	X	3159	0.23	-22	0.82
	ST	X	3158	0.16	0	0.95
$LiNbO_3$	Y	Z	3485	4.5	-85	0.31
	131°Y	X	4000	5.5	-74	0.26
	128° Y	X	4000	5.5	-72	
$LiTaO_3$	Y	Z	3230	0.74	-37	0.35
	X	112° Y	3295	0.64	-18	

Electromechanical coupling coefficient is a numerical measure of the conversion efficiency between electrical and acoustic energy in piezoelectric materials. Qualitatively the electromechanical coupling coefficient, K^2, can be determined as the portion of energy converted per input energy. So higher coupling coefficient means more efficient electric mechanic energy conversion.

From the table, it can be seen that ST cut quartz has zero temperature coefficient and relatively low coupling coefficient and relatively high transmission loss. So the SAW signal on ST quartz will be relatively weak. However, due to its zero temperature coefficient, ST quartz can be used in harsh environment with temperature variation but equipped with power supply. As for wireless application, $LiNbO_3$ can be used because of its high coupling coefficient and low transmission power loss. As for temperature related variation, it can be compensated by having temperature sensor on board.

2.4 Carbon Nanotubes (CNTs)

It has been observed from literature survey that CNT especially single wall CNT (swCNT) can be promising for CO_2 gas sensing due to its large surface-to-volume ratio. The absorption of CO_2 gas on the surface of swCNT changes many physical properties of swCNT, including impedance and mass. Researches on mass sensing of swCNT nanocomposites had long been conducted for its ease of implementation. However, mass sensing suffers from low precision caused by absorption of water vapors and other gas contents. On the contrary, impedance sensing shows more potential.

2.4.1 Types of CNTs [21]

CNTs can be mainly divided into two groups by its structure: single wall CNT (swCNT) and multi wall CNT (mwCNT).

2.4.1.1 swCNTs

Most swCNTs have a diameter of close to 1 nanometer, with a tube length that can be many millions of times longer. The structure of a SWNT can be conceptualized by wrapping a one-atom-thick layer of graphite called graphene into a seamless cylinder. The way the graphene sheet is wrapped is represented by a pair of indices (n,m) . The integers n and m denote the number of unit vectors along two directions in the honeycomb crystal lattice of graphene. If m = 0, the nanotubes are called zigzag nanotubes, and if n = m, the nanotubes are called armchair nanotubes. Otherwise, they are called chiral. The diameter of an ideal nanotube can be calculated from its (n,m) indices as follows

$$d = \frac{a}{\pi}\sqrt{(n^2 + nm + m^2)} \qquad \textbf{Eq. 2. 5}$$

where a = 0.246 nm.

SWCNTs are an important variety of carbon nanotube because most of their properties change significantly with the (n,m) values, and this dependence is non-monotonic. In particular, their band gap can vary from zero to about 2 eV and their electrical conductivity can show metallic or semiconducting behavior. SWCNTs are likely candidates for miniaturizing electronics. The most basic building block of these systems is the electric wire, and SWCNTs with diameters of an order of a nanometer can be excellent conductors. Fig. 2.7 shows the typical structure of swCNTs.

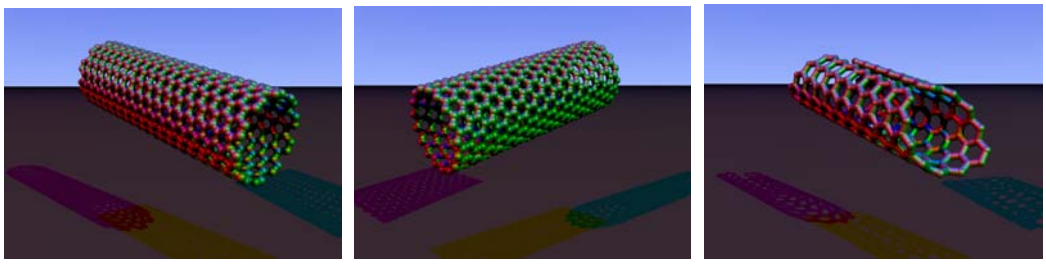

(a) (b) (c)

Figure 2. 7 Typical swCNT structure. (a) Armchair (n, n). (b) Zigzag (n, 0). (c) Chiral (n, m).

2.4.1.2 mwCNTs

MWNT consist of multiple rolled layers (concentric tubes) of graphite. There are two models that can be used to describe the structures of multi-walled nanotubes. In the Russian Doll model, sheets of graphite are arranged in concentric cylinders, e.g., a (0,8) swCNT within a larger (0,17)

swCNT. In the Parchment model, a single sheet of graphite is rolled in around itself, resembling a scroll of parchment or a rolled newspaper. The interlayer distance in mwCNTs is close to the distance between graphene layers in graphite, approximately 3.4 Å. The Russian Doll structure is observed more commonly. Its individual shells can be described as swCNTs, which can be metallic or semiconducting. Because of statistical probability and restrictions on the relative diameters of the individual tubes, one of the shells, and thus the whole mwCNT, is usually a zero-gap metal. A three layer mwCNT with armchair structure is shown in Fig. 2.8.

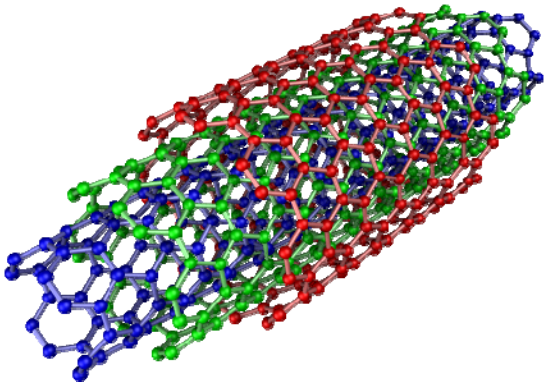

Figure 2. 8 Typical three layer mwCNT with armchair structure.

2.4.2 Fabrication of CNTs [21]

Techniques have been developed to produce nanotubes in sizeable quantities, including arc discharge, laser ablation, high-pressure carbon monoxide (HiPco), and chemical vapor deposition (CVD). Most of these processes take place in vacuum or with process gases. CVD growth of CNTs can occur in vacuum or at atmospheric pressure. Large quantities of nanotubes can be synthesized by these methods; advances in catalysis and continuous growth processes are making CNTs more commercially viable.

2.5 Gas Sensing Nanocomposites

Upon exposure to certain gases, the change in the properties of CNTs or CNTs-based composites can be detected by various methods. As a result, CNTs-based gas sensing systems and the theoretical analyses of gas adsorption and collision effects on the nanotubes have been the subjects of intense research [22].

2.4.1 Nanocomposites [23-29]

Nanocomposite is a special class of materials having unique physical properties and wide application potential in diverse areas [24]. Novel properties of nanocomposites can be obtained

by successfully imparting the characteristics of parent constituents to a single material. These materials differ from both the pure polymers and the inorganic nanomaterials in some physical and chemical properties. Polymer nanocomposites (PNC) have drawn great research interest for their unique physical, mechanical, and optical properties. Both inorganic and organic nanofillers are used for this purpose on a variety of polymers by different group of workers. Among the former category, mainly the clay polymer nanocomposites have drawn major attention because of their lower cost and very high reinforcing property [25]. The dispersion of metal or semiconductor nanoparticles within the polymer matrix also exhibits a large enhancement of the physical and mechanical properties [26-27]. Among the organic nanofillers, the carbon nanotube is the most important [28] because it possesses low mass density and large aspect ratio that yields a unique combination of mechanical, thermal, and electroactive properties [29].

2.4.2 CNT nanocomposite sensor

One promising sensing material based on polymers is conducting particles-insulating matrix composition [22]. The polymer acts as the insulating matrix while dispersed conducting particles provide the conducting path for sensing [30]. Due to adsorption of interested analyst, there are volumetric changes of the matrix polymer. This can lead to a distinct change in percolation-type conductivity around a critical composition of the material, which is known as "percolation threshold". Generally, the percolation threshold is dependent on the shape of the conducting particle. Composite consisted of particles with higher aspect ratio shows lower threshold and higher sensitivity [31]. CNTs, with almost one-dimensional thread-like structure and good conductivity, are ideal as the dispersed particles in this conducting particles-insulating matrix composition for gas sensing systems. Therefore, CNTs/polymer composites have been intensively studied for gas sensors [32–34].

Many CNT nanocomposites have been fabricated as gas sensing material. Polypyrrole (PpY)/CNT mixture shows almost 90% resistance change when exposed in 0.3% No_2 [35]. Ethyl cellulose (EC)/CNT nanocomposite shows 9% resistance change for 0.5% benzene [30]. Polymethylmethacrylate (PMMA)/CNT mixture shows resistance change over dichloromethane, chloroform and acetone [36].

In general, CNTs do not have sensing response to all gases and vapours but only the ones with high adsorption energy or that can interact with them [22]. Therefore, coating or doping of an enhance element on CNTs may broaden the application range. Chlorosulfonated polyethylene with tetrahydrofuran (THF) as a coating solution for CNT can be used for Cl_2 sensing, and Hydroxypropyl cellulose with chloroform as coating can be used to detect HCl [37]. The sensing response demonstrates a huge potential of using modified CNTs gas sensing materials for a broad range of gases and chemical vapors.

3.0 FABRICATION AND CHARACTERIZATION OF SAW FLOW SENSOR

3.1 Background

Since the development of SAW gas sensor involves both SAW sensor development and gas sensitive layer development, design, fabricate and test a SAW sensor naturally becomes the first step in SAW sensor development. Here, ST quartz is used to construct a flow sensor based on pressure sensing. The fabrication and testing protocol is thus built after the flow sensor construction.

Fluid flow sensor has broad applications in various industrial and research operation monitoring and control. It is especially important to have accurate flow measurement in some aero-space technology applications and some of the cutting edge research projects.

There has been numerous flow sensors, some of them already commercialized. Traditional mechanical flow sensors, such as venturi flow meters [38-40] and pitot tube flow meters [41-43], do not require power supply, and have simple structures. However, the readouts of these traditional flow sensors are not compatible with electronic system, making them unsuitable for modern applications.

Modern electronic flow sensors can be divided into several categories based on operation principles. One of the most important types of flow sensor is thermal flow sensor [44-48], including hot-wires anemometers, calorimetric flow sensors. They usually have a heater and at least one temperature sensing element to measure, e.g. the heat transfer from the heater to the thermometer. These flow sensors can have broad measurement range, from micro fluid measurement to macroscopic petroleum transport pipes. It's also convenient to integrate these sensors into CMOS circuit same chip control. The other important type of flow sensor is ultrasonic flow sensor [49-51]. The sensing structure is clamped to the outside wall of the pipe, where ultrasonic wave travels through the flow and is reflected back through the flow and intercepted by the receiver. The response of the ultrasonic wave, including resonant frequency, magnitude and phase change depends on the flow rate through the pipe. However, the power consumption of these sensors makes them hard to be used in portable devices or remote areas where power supply is a challenge.

For pressure driven laminar flow, as shown in Fig. 3.1, the pipe wall is subject to pressure along the flow direction. The pressure on the wall decreases linearly towards the exit. When a sensor is mounted on the pipe wall, the sensor will also be subject to linearly decreased pressure. For sensor with small surface area compared to pipe dimension, the pressure can be assumed to be uniform.

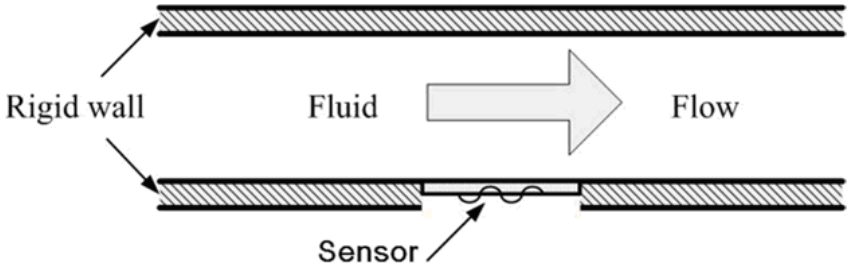

Figure 3. 1 Pressure Driven Laminar Flow Schematic View.

Previous research [52-54] showed that, for laminar flow, the pressure difference between specific point on pipe wall and flow exit depended linearly on flow rate. Since flow rate depends linearly on pressure, the flow meter essentially functions as a pressure sensor.

To facilitate the integration of wireless module, surface acoustic wave (SAW) is chosen as the sensing method. SAW sensor has been widely used for its low power consumption and easy operation and compatibility with wireless.

There has been some research on SAW pressure sensor design and fabrication [55-58]. However, the fabricated sensor is based on LiNbO3 and has two-layer chamber structure. Since LiNbO3 is temperature dependant, the pressure sensor is unstable without proper temperature compensation. The complicated two-layer structure also makes it unsuitable for flow sensor application.

ST-X cut quartz is selected for flow sensor due to its abundance and temperature stability. Plate structure is used for fabrication simplicity.

3.2 Theoretical Analysis

3.2.1 Pressure on Chamber Induced by Flow

Consider as a two-plate Couette flow problem shown in Fig. 3.2 (a). There is only one velocity component v along the x direction, and the boundary condition is v(-H/2)=v(H/2)=0. The pressure field is denoted by *p*.

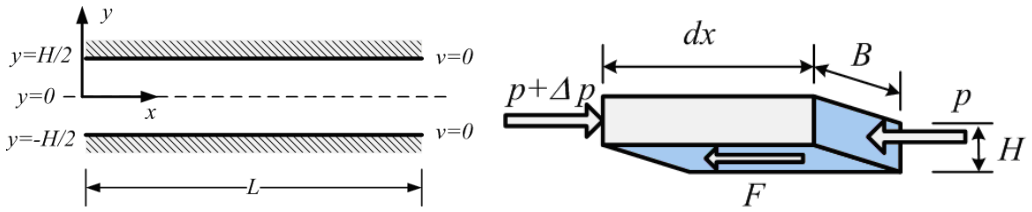

(a) (b)

Figure 3. 2 (a) Two plate Couette problem. (b) Short Segment of flow chamber under pressure and dragging force.

For a linear viscous fluid with viscosity μ, the flow profile is

$$v = V\left(1 - \frac{4y^2}{H^2}\right), \qquad \textbf{Eq. 3. 1}$$

where V is the maximum flow velocity, which will be determined below,

Assumptions:

- The cross-section area of the rectangular flow chamber is $A = BH$, where B is the width of the chamber and H is the height of the chamber, and its perimeter is c= 2(B+H).
- Along axis pressure gradient is $\frac{dp}{dx}$,
- Dragging force on the chamber inner surface follows a linear relationship, i.e. $\tau = \alpha V$, where τ is the shear stress on the resonator top surface, and α is the drag coefficient.

Now consider a short segment of the chamber (length *dx*) as Fig. 3.2 (b), then the force balance is, *F=f dx c= - dp A*

Assuming a 2-D flow as in Eq. 3.1, the width of the chamber should be much larger than the height, B>>H, so the friction force on the side walls can be ignored. Therefore,

$$V = -\frac{BH}{2\alpha(B+H)}\frac{dp}{dx} \approx -\frac{H}{2\alpha}\frac{dp}{dx}$$

At the chamber walls, for a linear viscous fluid with a viscosity μ, the friction should be equal to shear stress, which is,

$$\tau = \mu\frac{\partial v}{\partial y}\bigg|_{y=\pm\frac{H}{2}} = \frac{4\mu V}{H}$$

Therefore,

$$\alpha = \frac{4\mu}{H}$$

and

$$V = -\frac{H^2}{8\mu}\frac{dp}{dx} \qquad \textbf{Eq. 3. 2}$$

The flow profile is now,

$$v = -\frac{1}{2\mu}\frac{dp}{dx}\left(\frac{H^2}{4} - y^2\right) \qquad \textbf{Eq. 3. 3}$$

If p_0+p_1 is the pressure at x=0, and p_1 is the pressure at $x = L$, then $\frac{dp}{dx} = -\frac{p_0}{L}$. Then, from Eq. 3.2, the flow profile is

$$v = V\left(1 - \frac{4y^2}{H^2}\right), \quad V = \frac{p_0 H^2}{8\mu L} \qquad \textbf{Eq. 3. 4}$$

The flow rate: $$Q = \frac{2VHB}{3} = \frac{p_0 H^3 B}{12\mu L} \qquad \textbf{Eq. 3. 5}$$

pressure: $$\sigma_{xx} = \sigma_{yy} = -p(x) = -p_0(L - x)/L - p_1 \qquad \textbf{Eq. 3. 6}$$

shear stress: $$\tau_{xy} = -\tau_0 y, \quad \tau_0 = \frac{p_0}{L} \qquad \textbf{Eq. 3. 7}$$

From the above equation, the flow rate is proportional to the pressure difference along the flow path of length L, width B and height H.

3.2.2 Initial Deformation of the Resonator

With p and τ known from Eqs. 3.6 and 3.7, the initial deformation of the resonator induced by flow can be determined. Consider the free-body diagram of the resonator, a unit length of the structure in the X_3 direction. The bending moment distribution is shown in Fig. 3.3 (a).

When the length of resonator is much smaller than the length of flow chamber, i.e. $l << L$, the pressure p on the resonator can be assumed to be uniform as in Fig. 3.3 (b).

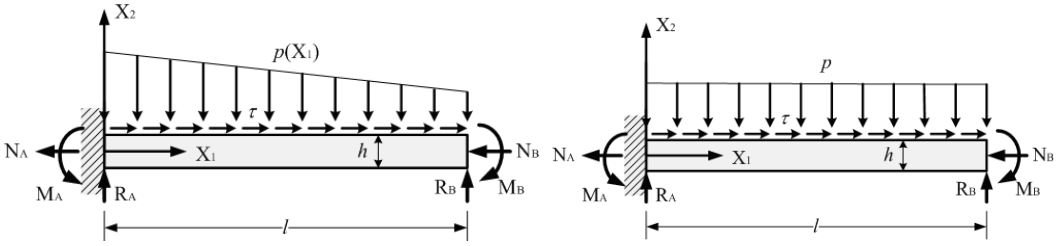

(a) (b)

Figure 3. 3 (a) Bending moment distribution in the unit length of the free body diagram of the resonator in X_3 direction. (b) Approximated uniform bending moment distribution.

Assumptions:

- The length of the resonator plate is much larger than its thickness.
- Plane strain beam

For planar deformation of thin plates, let $w_1^{(0)}$ and $w_2^{(0)}$ be the plate middle plane extensional and flexural displacements. $w_1^{(0)}$ and $w_2^{(0)}$ are governed by the following two systems of equations, respectively:

$$\begin{aligned} &\bar{c}_{11} A w_{1,1}^{(0)} = N_A - \tau X_1 \\ &\bar{c}_{11} I w_{2,11}^{(0)} = M \end{aligned} \qquad \textbf{Eq. 3. 8}$$

$$M(X_1) = -M_B + (l - X_1) R_B - p\frac{(l - X_1)^2}{2}$$

And their boundary conditions

$$\begin{aligned} &w_1^{(0)}(0) = 0, \;\; w_1^{(0)}(l) = 0, \\ &w_2^{(0)}(0) = 0, w_2^{(0)}(l) = 0, \; w_{2,1}^{(0)}(0) = 0, \; w_{2,1}^{(0)}(l) = 0 \end{aligned} \qquad \textbf{Eq. 3. 9}$$

$$(N_A = \frac{1}{2}\tau l, \; R_B = \frac{1}{2} pl, \; M_B = \frac{1}{12} pl^2)$$

where $\bar{c}_{11} = c_{11} - c_{12}^{\,2} / c_{22}$, c_{pq} are elastic stiffness constants. $A=h(1)$ is the cross sectional area.

$I = h^3/12$ is the moment of inertia of A. Solving Eq. 3.8, it can be calculated that:

$$\begin{aligned} &w_1^{(0)}(X_1) = \frac{\tau(l - X_1)X_1}{2\bar{c}_{11}A} = \frac{\tau(l - X_1)X_1}{2\bar{c}_{11}h}, \\ &w_{2,1}^{(0)}(X_1) = -\frac{pX_1(l - X_1)(l - 2X_1)}{12\bar{c}_{11}I} = -\frac{pX_1(l - X_1)(l - 2X_1)}{\bar{c}_{11}h^3}, \\ &w_2^{(0)}(X_1) = -\frac{pX_1^{\,2}(l - X_1)^2}{24\bar{c}_{11}I} = -\frac{pX_1^{\,2}(l - X_1)^2}{2\bar{c}_{11}h^3} \end{aligned} \qquad \textbf{Eq. 3. 10}$$

Then the biasing displacement field ***w*** can be calculated from the plate extensional and flexural displacements through

$$w_1(X_1) \cong w_1^{(0)}(X_1) - X_2 w_{2,1}^{(0)}(X_1),$$
$$w_2(X_1) \cong w_2^{(0)}(X_1), \qquad \textbf{Eq. 3. 11}$$
$$w_3(X_1) \cong 0.$$

3.2.3 The unperturbed SAW mode

The thickness of the crystal plate is chosen to be much larger than the wavelength of the SAWs. So the SAWs at the bottom surface of the plate decay sufficiently in the plate thickness direction and do not interfere with the interface between the plate and the fluid. Therefore, the SAWs propagating along top surface of an elastic half space with $\overline{X}_2 > 0$, as shown in Fig. 3.4, can be effectively evaluated.

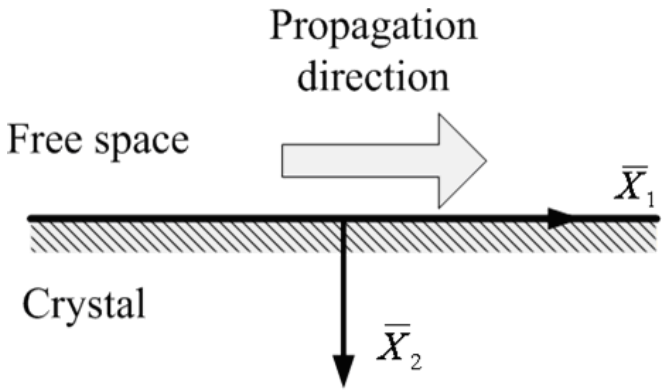

Figure 3. 4 SAWs propagating along top surface of an elastic half space

Consider Rayleigh surface waves with angular frequency ω, wave number k in the $\overline{X}_1$ direction, phase speed $C_R = \omega/k$, and displacement **u**. Consider quartz which is of holoaxial, trigonal symmetry and allow plane-strain motions. Rayleigh waves over a half space of quartz crystals with a traction-free boundary surface are given by

$$\rho \frac{\partial^2 u_i}{\partial t^2} = c_{ijkl} \frac{\partial^2 u_k}{\partial x_l \partial x_j} \qquad (i, j, k, l = 1, 2, 3)$$

$$u_i = u_{0i} \exp j\left[\omega t - k\left(l_1 x_1 + l_2 x_2 + l_3 x_3\right)\right]$$

$$\left(c_{ijkl} l_l l_k - \rho v^2 \delta_{ik}\right) u_{0k} = 0$$

$$\left|c_{ijkl}l_l l_k - \rho v^2 \delta_{ik}\right| = 0$$

$$\begin{vmatrix} \Gamma_{11} - \rho v^2 & \Gamma_{12} & \Gamma_{13} \\ \Gamma_{12} & \Gamma_{22} - \rho v^2 & \Gamma_{23} \\ \Gamma_{13} & \Gamma_{23} & \Gamma_{33} - \rho v^2 \end{vmatrix} = 0$$

$$\begin{cases} u_1 = \exp\left(-2\pi\beta\overline{X}_2/\lambda_R\right)\cos\left(2\pi g\dfrac{\overline{X}_2}{\lambda_R} + \alpha\right)\cos\left[\omega\left(t - \dfrac{\overline{X}_1}{C_R}\right) - \alpha\right] \\ u_2 = -r\exp\left(-2\pi\beta\overline{X}_2/\lambda_R\right)\cos\left(2\pi g\dfrac{\overline{X}_2}{\lambda_R} + \alpha\right)\sin\left[\omega\left(t - \dfrac{\overline{X}_1}{C_R}\right) - \alpha\right] \end{cases} \quad \textbf{Eq. 3. 12}$$

where β, λ_R, g, α, C_R and r depend on material properties.

3.2.4 Frequency shift on pre-stressed substrate

Consider a homogeneous material body occupying a region V. The body is free from any deformations and fields.

The mass density is ρ_0.

The second and third order elastic constants of the substrate are $c_{K\alpha L\gamma}$ and $c_{K\alpha L\gamma AB}$, respectively.

Suppose that the governing equations and boundary conditions allow a linear acoustic mode with frequency ω and displacement **u**.

When an initial displacement field **w** with initial stress $\mathbf{T}^0$ and initial strain $S^0_{KL} = \left(u_{K,L} + u_{L,K}\right)/2$ is applied, the frequency of the mode is perturbed a little and is denoted by $\omega+\Delta\omega$.

The frequency shift due to the initial fields is represented by the following integral from a first-order perturbation analysis [59-60]

$$\frac{\Delta\omega}{\omega} \cong \frac{1}{2\omega^2}\frac{\int_V \hat{c}_{K\alpha L\gamma}u_{\alpha,K}u_{\gamma,L}dV}{\int_V \rho_0 u_\alpha u_\alpha dV} \quad \textbf{Eq. 3. 13}$$

Where $\hat{c}_{K\alpha L\gamma}$ is the modification of the second-order elastic constants by the initial fields and is given by

$$\hat{c}_{K\alpha L\gamma} = T^0_{KL}\delta_{\alpha\gamma} + c_{K\alpha LN}w_{\gamma,N} + c_{KML\gamma}w_{\alpha,M} + c_{K\alpha L\gamma AB}S^0_{AB} \qquad \textbf{Eq. 3. 14}$$

Note:

- The initial field **w** is induced by the fluid pressure and the drag.
- The unperturbed mode **u** is when the initial fields are absent.

With the initial fields in Eq. 3.11 and the unperturbed modes in Eq. 3.12, the perturbation integral in Eq. 3.13 can be calculated. The displacement gradients needed in Eq. 3.14 can be calculated by Eq. 3.11. $w_{2,2}$ can be obtained from the stress relaxation condition T_2=0 for thin plates. To use in Eq. 3.13, it's necessary to expand Eq. 3.12 into $\cos\omega t$ and $\sin\omega t$ terms and use the coefficient of either $\cos\omega t$ or $\sin\omega t$.

3.3 Surface Acoustic Wave Sensor Design

3.3.1 Piezoelectric Substrate Material

The piezoelectric substrate is selected using a ST-X cut quartz membrane for its higher excitation strength of SAW and its negligible temperature dependence from -20℃ to 100℃. And the K^2 is about 0.15%, which is small compared with some other strong piezoelectric materials.

ST-cut quartz has Euler Angles (0º, 132.75º, 0º), so its transform matrix is

$$\mathbf{A} = \begin{bmatrix} 1 & 0 & 0 \\ 0 & \cos 42.75° & \sin 42.75° \\ 0 & -\sin 42.75° & \cos 42.75° \end{bmatrix}$$

The material parameters of alpha quartz are:
Elastic stiffness coefficients:

$$\mathbf{c} = \begin{bmatrix} c_{11} & c_{12} & c_{13} & c_{14} & 0 & 0 \\ c_{12} & c_{11} & c_{13} & -c_{14} & 0 & 0 \\ c_{13} & c_{13} & c_{33} & 0 & 0 & 0 \\ c_{14} & -c_{14} & 0 & c_{44} & 0 & 0 \\ 0 & 0 & 0 & 0 & c_{44} & c_{14} \\ 0 & 0 & 0 & 0 & c_{14} & \frac{1}{2}(c_{11} - c_{12}) \end{bmatrix}$$

where $c_{11} = 86.74 \times 10^9 N/m^2$, $c_{12} = 6.99 \times 10^9 N/m^2$, $c_{13} = 11.91 \times 10^9 N/m^2$,

$c_{14} = -17.91 \times 10^9 N/m^2$, $c_{33} = 107.2 \times 10^9 N/m^2$, $c_{44} = 57.94 \times 10^9 N/m^2$,

$c_{66} = 39.88 \times 10^9 N/m^2$.

The dielectric matrix:

$$\varepsilon = \begin{bmatrix} 0.3921 & 0 & 0 \\ 0 & 0.3921 & 0 \\ 0 & 0 & 0.4103 \end{bmatrix}^{\times 10^{-10}}$$

The piezoelectric coefficients:

$$e = \begin{bmatrix} 0.171 & -0.171 & 0 & -0.0436 & 0 & 0 \\ 0 & 0 & 0 & 0 & 0.0436 & -0.171 \\ 0 & 0 & 0 & 0 & 0 & 0 \end{bmatrix}^{C/m^2}$$

So, the elastic stiffness coefficients matrix of ST-cut quartz is

$$\mathbf{c}' = \begin{bmatrix} 86.74 & -8.60 & 27.50 & 1.05 & 0 & 0 \\ -8.60 & 130.74 & -4.81 & -1.84 & 0 & 0 \\ 27.50 & -4.81 & 96.63 & 13.44 & 0 & 0 \\ 1.05 & -1.84 & 13.44 & 41.22 & 0 & 0 \\ 0 & 0 & 0 & 0 & 67.47 & 7.60 \\ 0 & 0 & 0 & 0 & 7.60 & 30.35 \end{bmatrix}^{\times 10^9 N/m^2}$$

Similarly, the dielectric matrix and the piezoelectric coefficient matrix are obtained as

$$\varepsilon' = \begin{bmatrix} 0.3921 & 0 & 0 \\ 0 & 0.4005 & 0.0091 \\ 0 & 0.0091 & 0.4019 \end{bmatrix}^{\times 10^{-10}}$$

$$e' = \begin{bmatrix} 0.1710 & -0.1327 & -0.0383 & 0.0821 & 0 & 0 \\ 0 & 0 & 0 & 0 & 0.1071 & -0.0720 \\ 0 & 0 & 0 & 0 & -0.0990 & 0.0665 \end{bmatrix}^{C/m^2}$$

The mass density of quartz is 2.649 g/cm^3 at 20℃. The phase velocity of a SAW on ST-cut quartz is 3158 m/s.

3.3.2 Design of the SAW sensor

The synchronous frequency is 52.563 MHz, which limits the highest frequency of operation of

SAW devices to a few GHz

According to Eq. (11), the strain S_{11} of the resonator can be determined as

$$S_{11} = w_{1,1} = \frac{\tau(l-2X_1)}{2\bar{c}_{11}h} - X_2\left(-\frac{p\left(l^2-6lX_1+6X_1^2\right)}{\bar{c}_{11}h^3}\right)$$

When the resonator locates at the bottom center of flow chamber, then $p = \frac{p_0}{2} + p_1$, $\tau = \frac{p_0 H}{2L}$, the strain on the bottom of the resonator is

$$S_{11}\big|_{X_2=-\frac{h}{2}} = w_{1,1} = \frac{p_0 H(l-2X_1)}{4\bar{c}_{11}hL} - \frac{\left(\frac{p_0}{2}+p_1\right)\left(l^2-6lX_1+6X_1^2\right)}{2\bar{c}_{11}h^2} \qquad \textbf{Eq. 3. 15}$$

For a rectangular flow chamber of 165.10 mm × 69.85 mm × 0.51 mm (L × B × H) and composed of 2 parallel acrylic plates, it can be calculated that $p_1 = 0$, $\tau/p = 0.3089\%$, the effect of shear stress can be neglected, and the strain S_{11} in Eq. 3.15 can be calculated by

$$S_{11}\big|_{X_2=-\frac{h}{2}} = S'_{11}\big|_{X_2=-\frac{h}{2}} + S''_{11}\big|_{X_2=-\frac{h}{2}} \approx S''_{11}\big|_{X_2=-\frac{h}{2}} = -\frac{\left(\frac{p_0}{2}+p_1\right)\left(l^2-6lX_1+6X_1^2\right)}{2\bar{c}_{11}h^2} \qquad \textbf{Eq. 3. 16}$$

The dimension of the resonator plate is 20 mm × 20 mm × 0.3 mm. When the pressure on the resonator induced by flow is 10kPa and 40kPa separately, the relative errors between S_{11} and S''_{11} on the bottom of plate can be calculated and plotted in Fig. 3.5. From Fig. 3.5 the relative error is less than 0.1%.

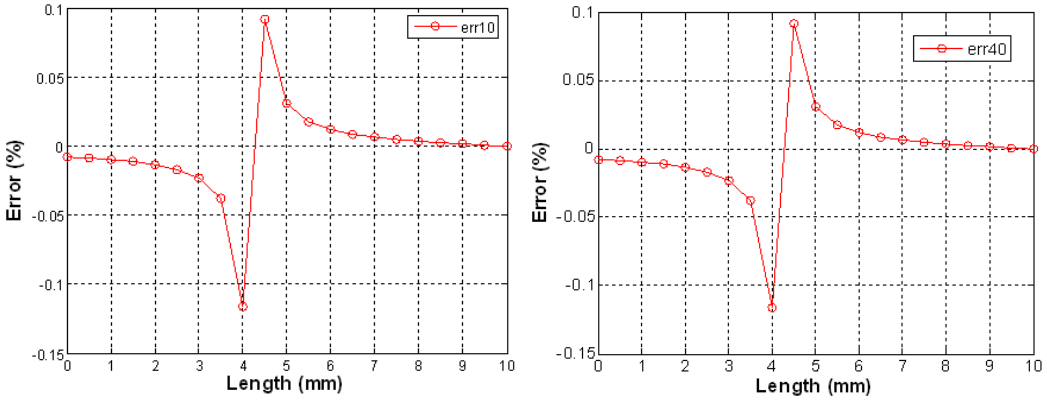

(a) (b)

Figure 3. 5 Theoretical relative error of neglecting the shear stress (a) Error at 10kPa. (b) Error at 40kPa.

It is known that the input/output IDTs are arranged on the expanding region of the piezoelectric substrate bottom. It is also known that the pressure sensitivity of ST-X cut quartz is higher when the propagation path of a SAW is close to 10 mm or 3 mm [61]. For a fixed rectangular plate (20 mm × 20 mm × 0.3 mm) made of ST-X cut quartz under a uniform pressure, its deformation and normal strain along x direction can be numerically calculated by ANSYS and shown in Fig. 3.6.

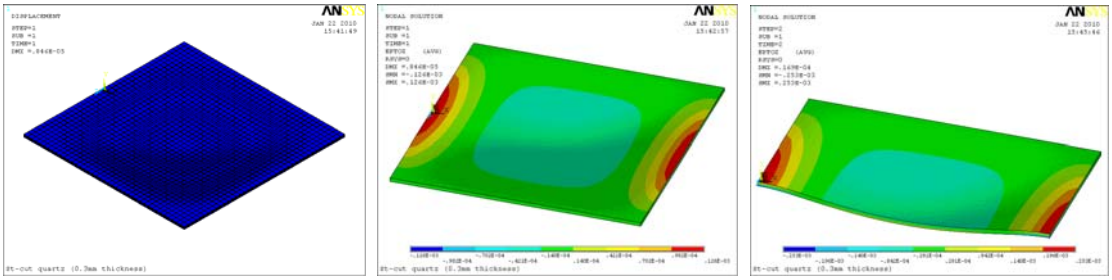

(a) (b) (c)

Figure 3. 6 FEM results about ST-X cut substrate under pressure. (a) Deformation under 10kPa pressure. (b) Strain S_{11} under 10kPa pressure. (c) Strain S_{11} of half plate under 20kPa pressure.

The S_{11} results on the central line of bottom of ANSYS simulation and plain strain beam calculation results by Eq. 3.16 are shown in Fig. 3.7. For 20mm × 20mm × 0.3mm sensor, two simulation cases of 10kPa and 40kPa are shown in Fig. 3.7(a). For comparison, besides calculation results of 10kPa and 40kPa pressure on the sensor, the situation where the same pressure is applied to a 30mm × 30mm × 0.3mm sensor is also calculated and shown in Fig. 3.7(b).

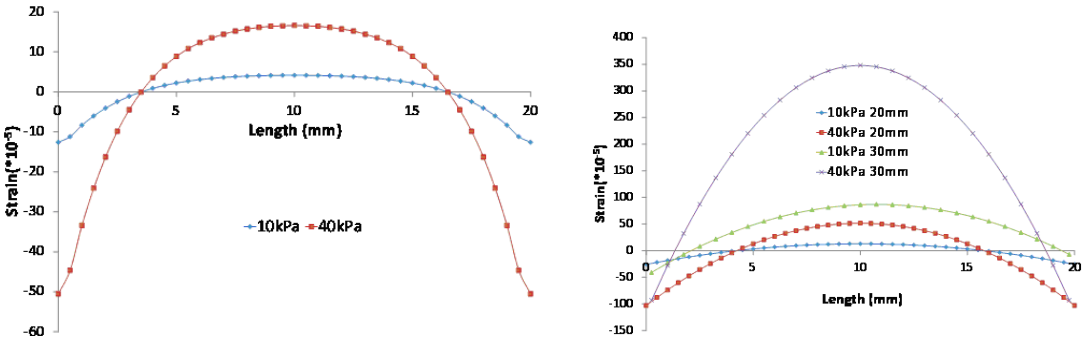

(a) (b)

Figure 3. 7 The strain S_{11} on the central line of plate bottom from simulation and calculation. (a) FEM result for 20mm × 20mm × 0.3mm sensor. (b) Calculation results for 20mm × 20mm × 0.3mm and 30mm × 30mm × 0.3mm sensors.

The resulted phase changes of the SAWs under different situations are also calculated and shown in Fig. 3.8 (a). As can be seen, the response phase change is greater for larger plate and higher pressure.

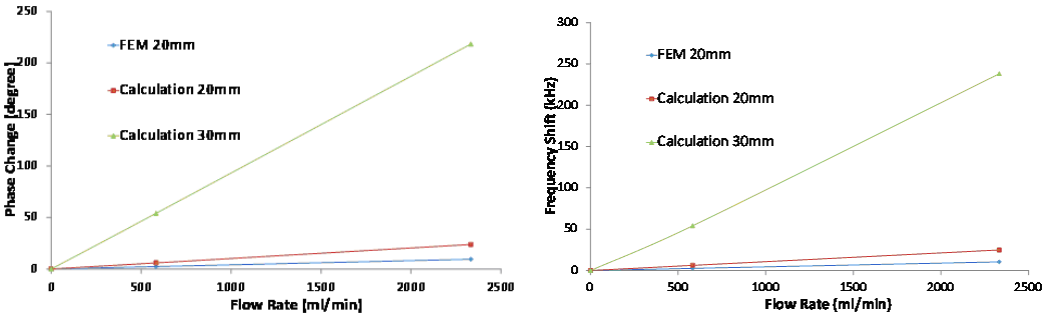

(a) (b)

Figure 3. 8 (a) Simulated and calculated phase change versus flow rate of the chamber. (b) Simulated and calculated frequency shift versus flow rates of the chamber

For frequency shift, it is known that the frequency will decrease with the increase of strain, i.e., the increase of flow rate [62]. The related expecting frequency shifts are shown in Fig. 3.8 (b).

3.3.3 Design and fabrication of the testing system

Fig. 3.9 shows the schematic view of the chamber, which is composed of 2 parallel acrylic plates, in which a rectangular flow channel with dimension 165.10 mm × 69.85 mm × 0.51 mm ($L \times B \times H$), inlet and outlet reservoir, one sensor mounting port, and one inlet port and outlet port are formed.

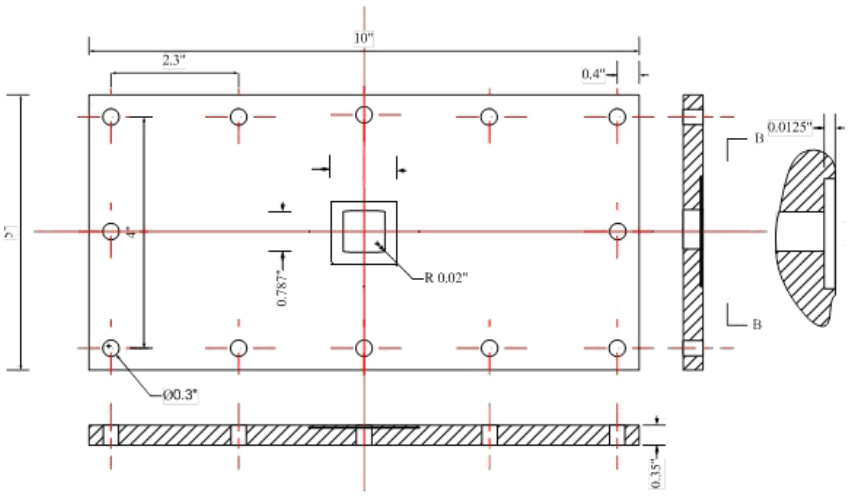

(a) Top plate of chamber.

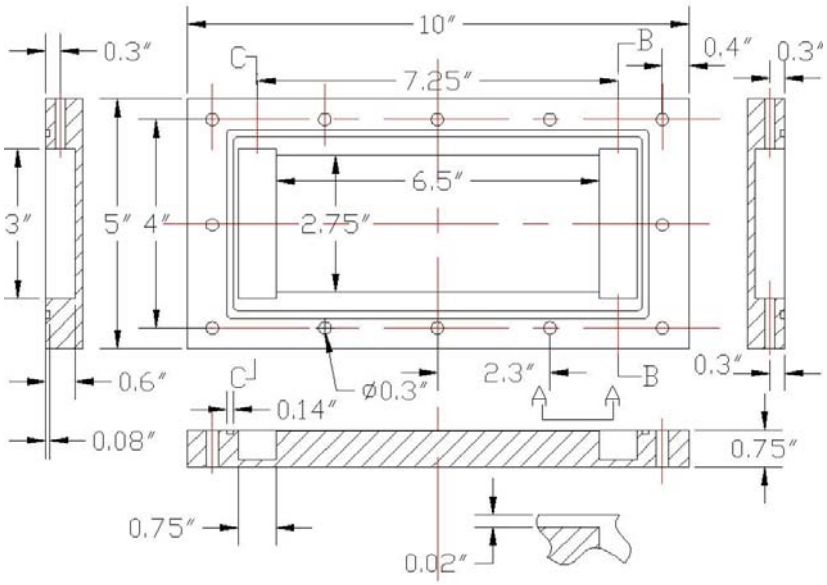

(b) Bottom plate of chamber

Figure 3. 9 The dimension of chamber

Since SAW signal will damp significantly in water and other liquids, it is natural that IDTs are located on the back of the substrate, thus SAW can propagate on the back of substrate. From Fig. 3.7, it can be seen that 5.7mm from the center of the sensor, the pressure induced strain is almost zero. Thus the IDTs begin from that point so they will have minimal deformation under pressure and the SAW propagation path is entirely located on tension area. The designed sensor has 70 pair of input and output IDTs and 3mm apart. The whole sensor is constructed on a 3cm × 3cm × 0.3mm quartz crystal substrate. And the two IDTs are located symmetrically on the center of the substrate.

A 50nm thick Cr layer was deposited on the Quartz wafer. Then a 150nm thick Au layer was sputtered on top of Cr layer. After that a 3μm thick AZ4210 was coated on Au surface by spin-coating at 3000rpm for 30 seconds. After patterning, the Au and Cr on IDT area were kept and others were removed by Au etchant and Cr etchant. The remaining photoresist is then removed by acetone. Finally the wafer is cleaned using IPA and DI water and then dehydrated for 30min at 120℃. Silver paste is used to connect the IDT electrodes to the measurement instrument. Fig. 3.10 shows the designed and fabricated sensors separately.

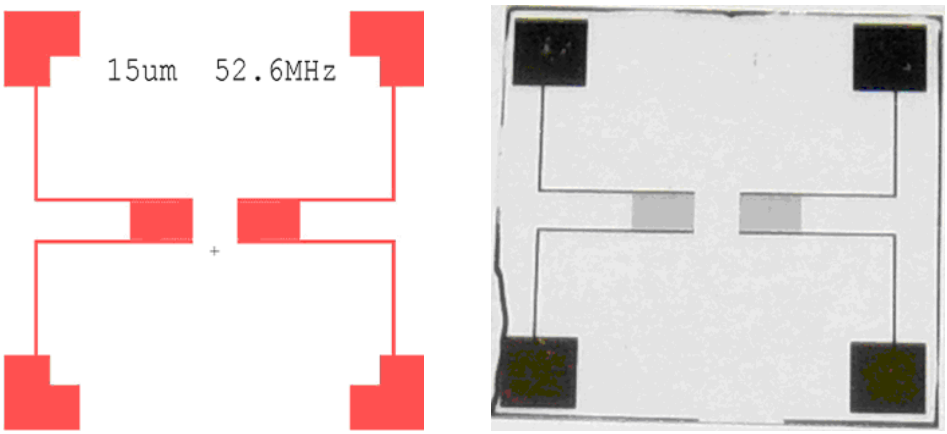

(a) (b)

Figure 3. 10 (a) Designed SAW sensor with 15um IDT finger and space. (b) Fabricated SAW sensor on 3cm × 3cm quartz crystal substrate.

The sensor mounting port on the top plate is 3cm × 3cm and around 350μm deep. On the center of the mounting port, a 2cm × 2cm square shape through hole is used to apply pressure on the center 2cm × 2cm area of the SAW sensor. Four through holes are constructed on the four corners of the mounting port to connect the electrode pad from the sensor to the measurement instruments. AZ4210 photoresist is used as adhesive to fix the fabricated sensor on the mounting port. Thus the sensor can be changed after experiments by cleaning the photoresist. The integrated experiment system is shown in Fig. 3.11.

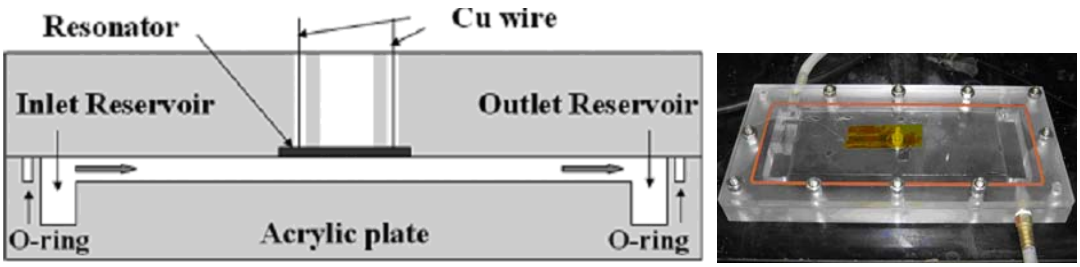

(a) (b)

Figure 3. 11 (a) Crosessetional view of the designed experiment setup. (b) Integrated experiment setup.

3.4 Experiment Results and Conclusion

The sensor is tested under different flow rates from 0ml/min up to 3500ml/min, which corresponds to normal pressure of 0Pa up to 60kPa. Using the group delay measurement function from network analyzer, the delay time and the corresponding resonant frequency of the sensor can be recorded simultaneously. When the flow rate increases from stagnant, the delay time changes accordingly. This increase of delay time is then converted into phase change after dividing by the

period of the SAW. From this aspect, the phase change is linearly dependent on delay time change.

From Fig. 3.12, it can be seen that the phase change of the sensor is linearly depending on the fluid flow rate at 1Deg/11.8ml/min, while the resonant frequency does not show obvious change along flow rate change, probably because the choice of IDT locations minimize the deformation of IDTs.

Comparing the experiment data with the theoretical value from Fig. 3.7, it can be seen that the actual phase change of the sensor is comparable to the case of 3cm × 3cm. The possible reason of this phenomenon is because the SAW sensor is mounted using AZ4210 photoresist. The photoresist is coated on the mounting port using brush. During the drying process, the evaporated solvent causes numerous holes on the adhesive layer, thus making the adhesive porous and vulnerable to external pressure. When subject to pressure from the flow, the adhesive layer close to the 2cm × 2cm opening cracks, thus the SAW sensor loses the supporting layer on the back. So the real area under pressure of the flow is close to 3cm × 3cm because of the loss of the support layer. The performance might be adjusted if permanent uniform bonding is adopted.

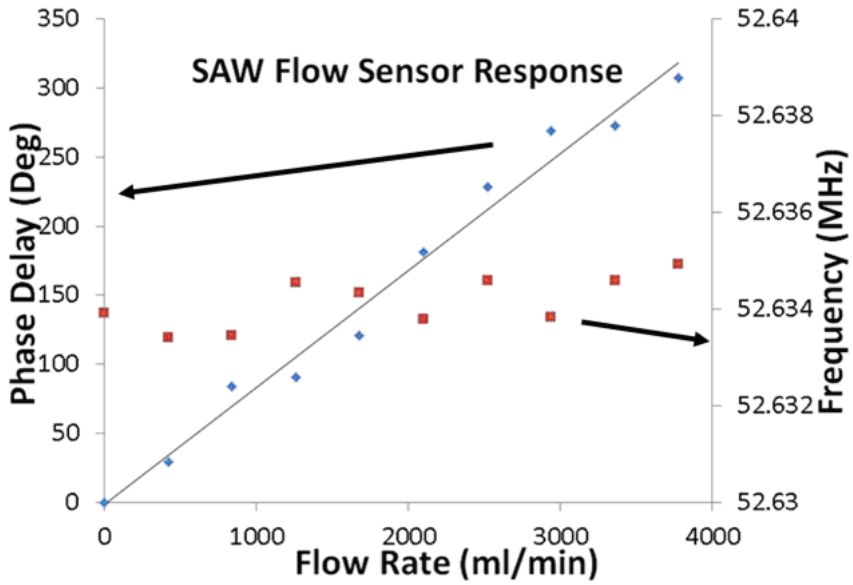

Figure 3. 12 SAW flow sensor reponse.

The experimental result shows irregular frequency change with the increase of the flow rate, which is different from the expected frequency decrease. The reason for the difference lies in two sides. First the resonant frequency is derived from the group delay measurement, where the signal

is integrated over the range of scanning frequency, so the frequency value is the result of indirect measurement, thus there might be certain system error. The other factor that might affect the resonant frequency is the fabrication process. For the fabricated SAW sensor, the finger width and space are both 15μm. A 0.08μm fabrication error will cause the resonant frequency shift of 300kHz. Using current fabrication process, the fabrication error is expected to be less than 1μm. So it's reasonable that the resonant frequency is not unique for each pair of IDT finger, thus the resonant frequency change cannot be recognized during the experiment.

To improve the sensitivity of flow sensor, thinner substrate can be used at lower measurement range. The device can also be operated at higher order resonant frequency to further improve the signal resolution. However, based on experiment observation, the insertion loss at high frequency might exceed the limit of the measurement instrument, making it less feasible for real application.

The flow sensor can also be incorporated with wireless function, while careful design and operating frequency decision are needed. The sensor dependence on temperature change is assumed negligible due to the property of ST cut quartz, while the other part of the testing system might be affected by temperate change. So it's necessary in the future to investigate in the overall temperature dependence of the testing system.

In all, analytical result implies linear relationship between flow rate and pressure difference along flow path. SAW sensor analysis and FEM simulation result shows that the phase delay of SAW signal depends linearly on the pressure on the sensor at low flow rate. Based on the analysis and simulation, the expected response of the SAW sensor is calculated. A SAW sensor based on quartz crystal substrate with 52.63MHz resonant frequency is designed and fabricated, along with the corresponding testing system. Test results show certain agreement with analysis in terms of phase delay, while the response of resonant frequency change falls under reasonable range around the expected curve. Overall, the SAW flow sensor can be potentially used in practical applications with certain calibration and can be integrated with wireless function in the future.

In a word, the development of SAW sensor proves that IDT delay time structure is suitable for sensor configuration and metal etching is better compared with lift off in IDT lithography.

4.0 CNT NANOCOMPOSITE FABRICATION AND CHARACTERIZATION

4.1 Introduction

Surface Acoustic Wave (SAW) technology [63] has long been used in gas sensing system [64]. With inter digital transducer (IDT), SAW is generated and travels along the surface, and is received by IDT on the other side of the sensor. The SAW frequency and phase/magnitude can be altered by changing the surface mass/impedance on SAW transmission path. Since most SAW base materials, such as quartz, are not sensitive to the gas concentration, a thin film that can respond to the environment is normally used.

Sensing thin films are normally formed by curing different polymers, due to the easy integration of polymer and SAW device fabrication [65]. Among the various polymers, polyimides (PIs) has excellent thermal stability and very good mechanical properties [66]. To make the thin film suitable for gas sensing, most PIs can be converted into porous material by several ways including adding porous filler, adding low temperature curing agent and some other methods [67]. The capability of withstanding high temperature makes PIs suitable for making various gas sensing membranes under harsh environments, especially when high temperature application is needed.

Since PIs are insulator, conductive fillers are necessary for impedance type thin film gas sensing membrane. Carbon nanotubes (CNTs) are the most successful conductive filler available until now. Since the introduction of CNTs, these new materials have attracted most attentions for their superb electrical, mechanical and thermal properties compared to conventional materials [68]. Lots of research has been done in utilizing CNTs as various sensors [69]. Because of its large surface-to-volume ratio, CNT will have faster response time and better response signal than other sensing materials.

It’s natural that CNTs can be incorporated into PIs to give the composite sensing property of CNTs without losing the mechanical and thermal properties of PIs.

To characterize the performance of SAW gas sensing system, the response of the composite in IDT configuration needs to be studied to set the reference for gas sensing.

There have been some researches done on PI-CNT composite thin films [70]. However, their researches are either based on mold formed CNT [71], which is different from thin films in terms of electrical properties, or the thin film had been pre-treated before mixing and curing [72], or their characterizations are based on specific measurement setup of dc conductivity measurement and dielectric measurement11. Since the measured percolation threshold and impedance performance depend on the thin film preparation process and the direction of the measurement, measurements incorporated with SAW IDTs, such as impedance spectroscopy, still need be studied.

4.2 Fabrication of CNT nanocomposite and Percolation Threshold Study

It has known that the impedance measurement results are different for the CNT-Polyimide nanocomposite with different mixing ratios. To determine the proper mixing ratio and manufacturing parameters for the thin film employed in CO_2 sensing system, analysis needs to be done regarding the different characteristic behavior of these thin films.

When polyimide and CNT are mixed, several different CNTs might connect each other and form a path across the thin film, thus turning the composite from insulating to conducting electrons. The theory that describes the relationship between the filler (CNTs in this particular case) concentration and the conductivity is called percolation theory. It has been shown there exists a critical filler concentration value that, when the concentration is below the critical value, the probability of forming a conducting path approaches to 0 infinitely, and while the concentration is above the critical value, the probability of conducting approaches to 1 infinitely. This critical value is called percolation threshold. The universality principle states that, the value of the percolation threshold is connected to the local structure of the film, while the behaviors of open clusters below, at, and above percolation threshold are invariant with respect to the local structure.

So it’s essential to find out the percolation threshold for the CNT-polyimide nanocomposite thin film since the property of the thin film below the percolation threshold will behave more like insulator while the behavior of the thin film above the percolation threshold is more close to ideal conductor. In current research project the response of the thin film to different CO_2 concentration is expected to reach maximum around the percolation threshold while maintaining the measurement feasibility.

4.2.1 Fabrication of CNT Nanocomposite

To measure the impedance of the thin film, dozens of pairs of electrodes are made under the thin film to ensure uniform and accurate impedance measurement. The electrodes are designed the same as interdigital transducers (IDTs), in accordance with the future integration with SAW devices.

A 50nm thick Cr layer was deposited on the Quartz wafer. Then a 150nm thick Au layer was sputtered on top of Cr layer. After that a 3um thick AZ4210 was coated on Au surface by spin-coating. After patterning, the Au and Cr on IDT area were kept and others were removed by Au etchant and Cr etchant. The remaining photoresist is then removed by acetone. Finally the wafer is cleaned using IPA and DI water and then dehydrated for 30min at 120℃.

The fabricated IDT has 60 pairs of fingers with 5mm length, 36 um width, 44um spacing, 4.8mm aperture.

The swCNTs are commercially available through Aldrich® company (2g, St. Louis, Mo, USA). The base fluid polyimide are from HD® Microsystem company (1 Gal, Parlin, NJ, USA). The base fluid is added into the beaker, then swCNTs are added the weight according to the desired mixing ratio. Then a magnetic stir bar is used for mixing. The whole beaker is covered by plastic wrap and stir for 5min or until the mixture shows uniform texture. After that, the mixture is poured on the top surface of the IDT chip. By using spin-coater, the mixture eventually forms a thin film of about 1um thick. The thin film covered IDT chip is finally baked on hotplate at 120℃ for 5min and 350℃ in the oven for 30min. Silver paste and silver wire serve as the connection path between the measurement instrument and the electrode pads of IDT.

4.2.2 CNT Nanocomposite Percolation Threshold

Since the thickness of the fabricated thin film is controlled to be around 1um, the thin film can be treated as a two dimensional structure. There are several different types of basic lattice models for 2D structure. As shown in Fig. 4.1, there are several different types of regular and Archimedean lattices. There are also many other types of irregular lattices, which is not shown in the picture [73].

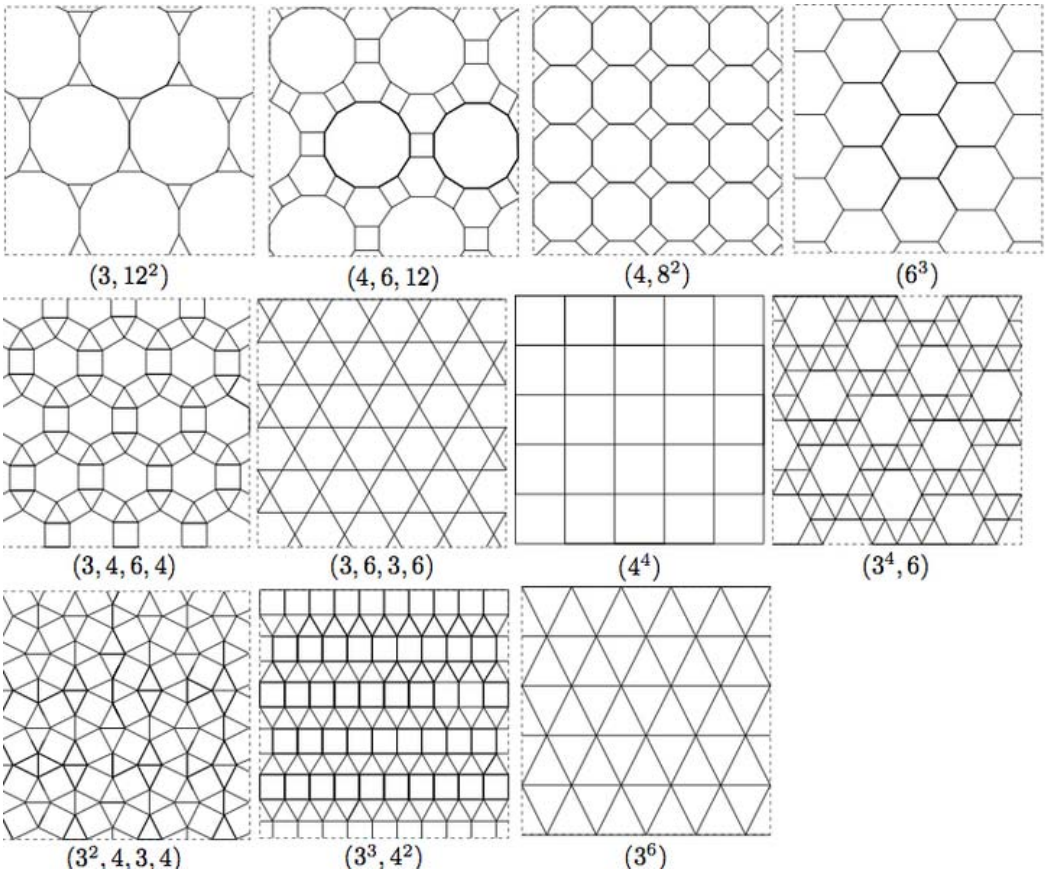

Figure 4. 1. Some of the regular and Archimedean lattices.

The notation underneath each lattice on the above figure means the number of every basic shape that each vertex is surrounded by.

Due to universality principle, it's beyond the interest of current project to investigate the detail lattice structure of CNT-polyimide nanocomposite thin film. The work is thus focused on percolation threshold, i.e. the transition region between insulator and conductor.

Fig. 4.2 shows the some of the impedance spectroscopy measurement results for different CNT weight ratios.

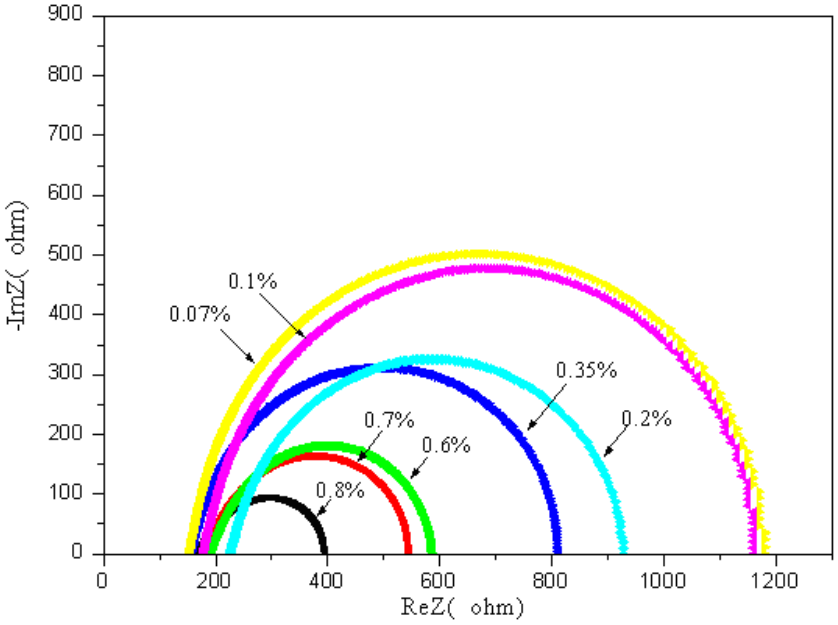

Figure 4. 2 Impedance spectroscopy of some CNT-Polyimide nanocomposite thin films with different weight ratios.

The weight ratio on the above figure ranges from 0.07% to 0.8%. Experiment data for samples with weight ratio below 0.07% exceeds the scope of the measurement instrument, thus 0.07% is chosen as starting concentration of the nanocomposite thin film. When the concentration increases beyond 0.8%, the resistivity of the thin film tends to decrease much slower than in lower concentration region, so only 0.8% is shown. In the meanwhile, the conductivity of the thin film changes drastically beyond 0.8%, so the data points after 0.8% will be included in the conductivity figure.

Since the thickness of the thin film and the dimensions of the IDT electrodes are known, the volume resistivity and volume conductivity can be calculated based on the following formula:

$$\rho = R\frac{A}{\ell} \qquad \textbf{Eq. 4. 1}$$

and

$$\sigma = \frac{1}{\rho} \qquad \textbf{Eq. 4. 2}$$

Fig. 4.3 and Fig. 4.4 show the volume resistivity and volume conductivity respectively.

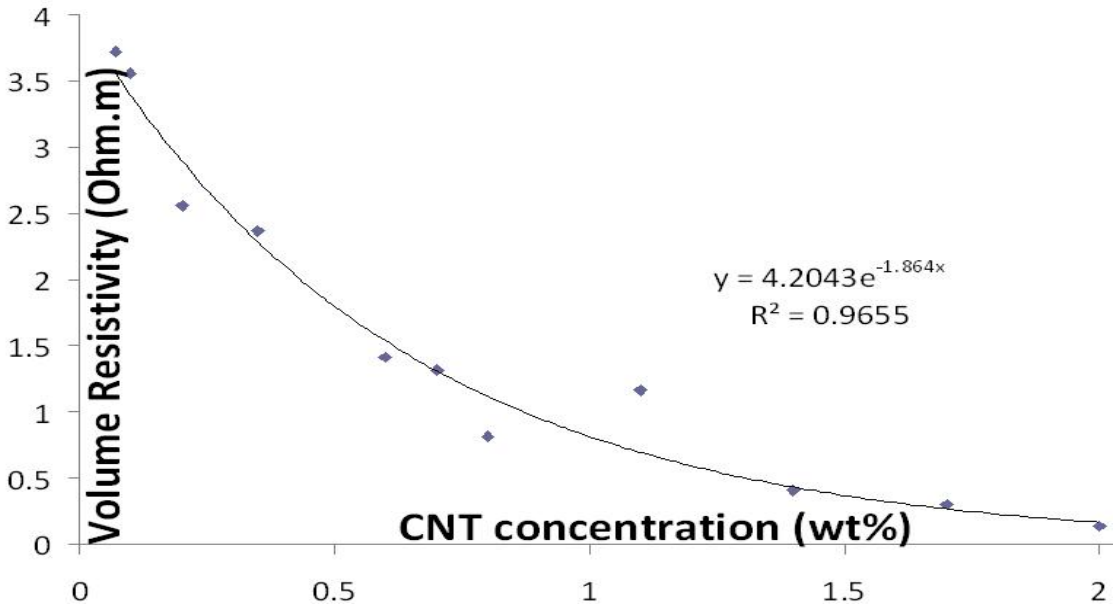

Figure 4. 3 Volume resistivity of nanocomposite thin film with respect to weight ratio.

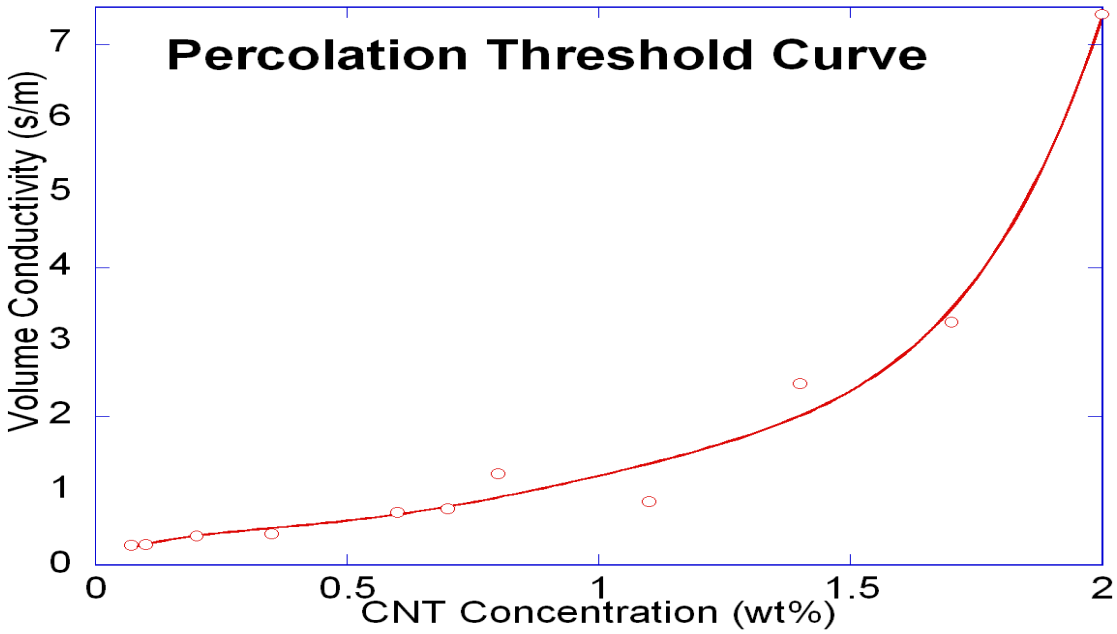

Figure 4. 4 Volume conductivity of nanocomposite thin film with respect to weight ratio.

As can be seen from above figure, the conductivity changes drastically between weight ratio of 0.7% and 0.8%. Similar to other similar figures like Fig. 4.5 from the literature, the conductivity and concentration relationship curve can be approximated by polynomial, and the second order derivative of the polynomial shows that the percolation threshold for CNT-PI nanocomposite is about between 1.1wt% and 1.4wt%.

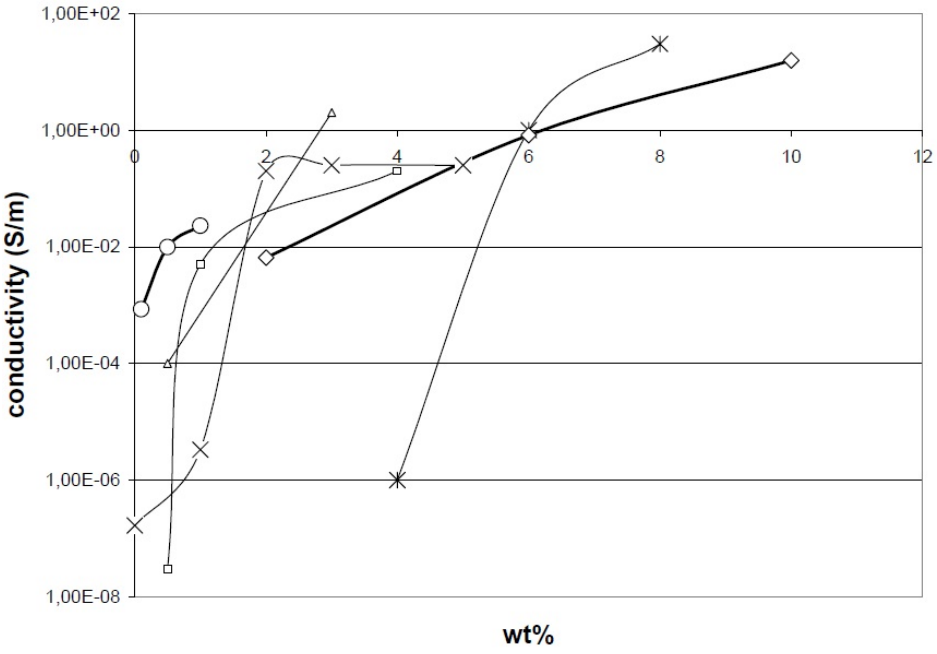

Figure 4. 5 Volume conductivity of CNT-polymer nanocomposite with respect to weight ratio from literature.

4.3 CNT Nanocomposite Response to Temperature Change

Different samples with mixing ratio from 0% (pure polyimide) up to 1.2% are prepared. Each sample is test under different temperature range from room temperature (25℃) up to more than 200℃.

Fig. 4.6 (a) shows the real part of pure polyimide thin film impedance measured by impedance analyzer. Fig. 4.6 (b) shows the imaginary part of pure polyimide thin film impedance measured by impedance analyzer. Fig. 4.6 (c) shows the Nyquist plot of the pure polyimide thin film. Fig. 4.7 (a) shows the real part of 0.02% mixing ratio thin film impedance measured by impedance analyzer. Fig. 4.7 (b) shows the imaginary part of 0.02% mixing ratio thin film impedance measured by impedance analyzer. Fig. 4.7 (c) shows the Nyquist plot of the 0.02% mixing ratio thin film. Fig. 4.8 to Fig. 4.18 shows the Nyquist plot for different mixing ratio thin film, increase from 0.05% up to 1.2%.

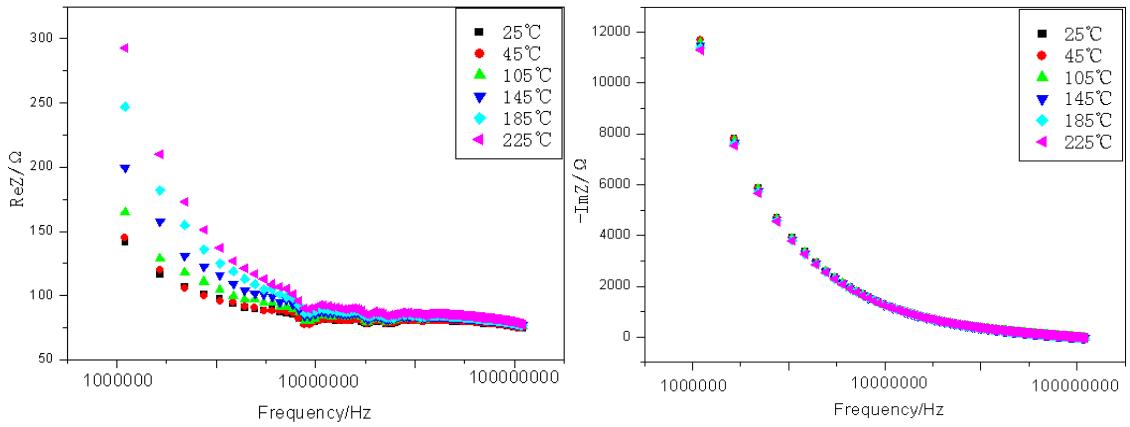

(a) (b)

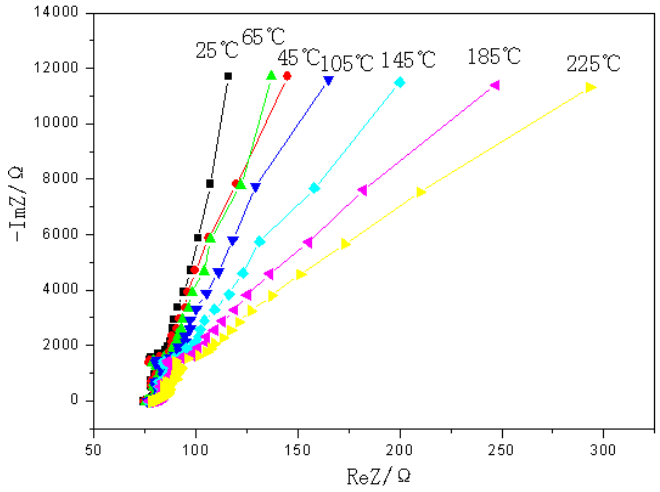

(c)

Figure 4. 6 Impedance of swCNT-polyimide composites(0%swcnt) at different temperature

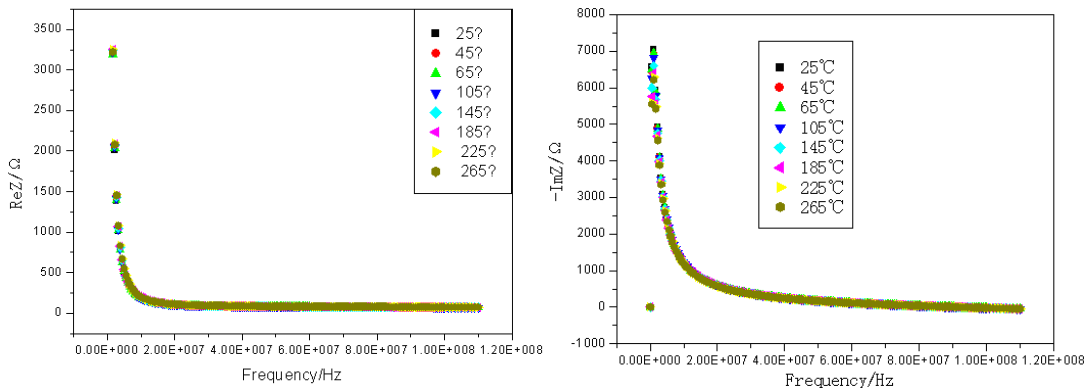

(a) (b)

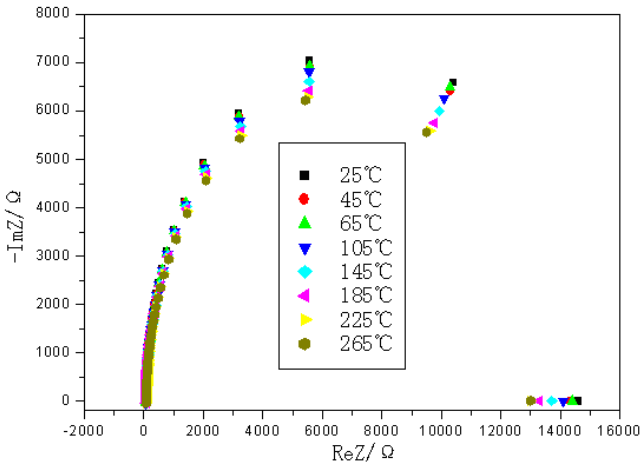

(c)

Figure 4. 7 Impedance of swcnt-polyimide composites(0.02%swcnt) at different temperature

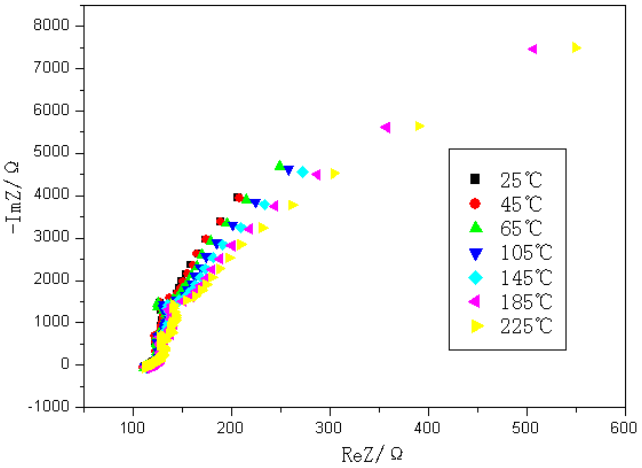

Figure 4. 8 Impedance of swcnt-polyimide composites(0.05%swcnt) at different temperature

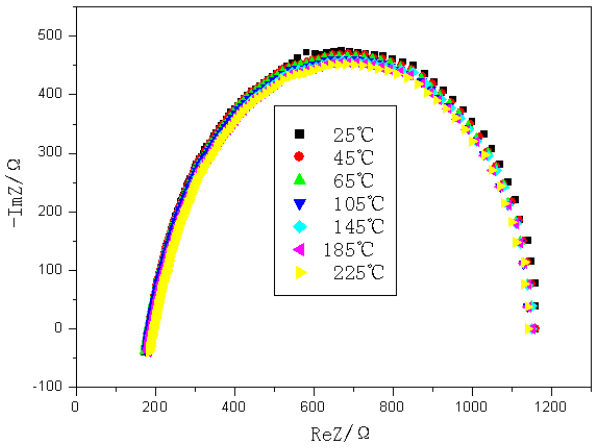

Figure 4. 9 Impedance of swcnt-polyimide composites(0.07%swcnt) at different temperature

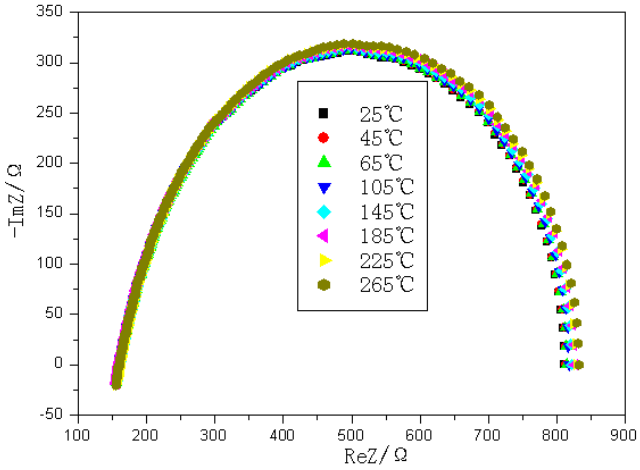

Figure 4. 10 Impedance of swcnt-polyimide composites(0.1%swcnt) at different temperature

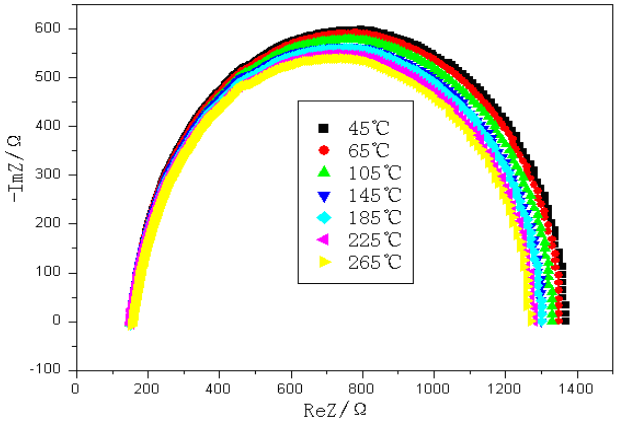

Figure 4. 11 Impedance of swcnt-polyimide composites(0.2%swcnt) at different temperature

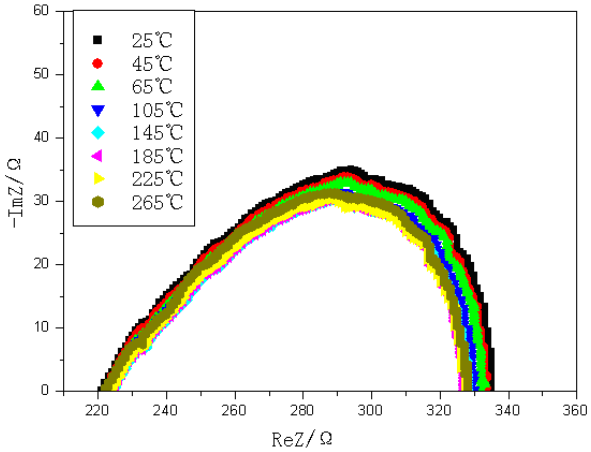

Figure 4. 12 Impedance of swcnt-polyimide composites(0.35%swcnt) at different temperature

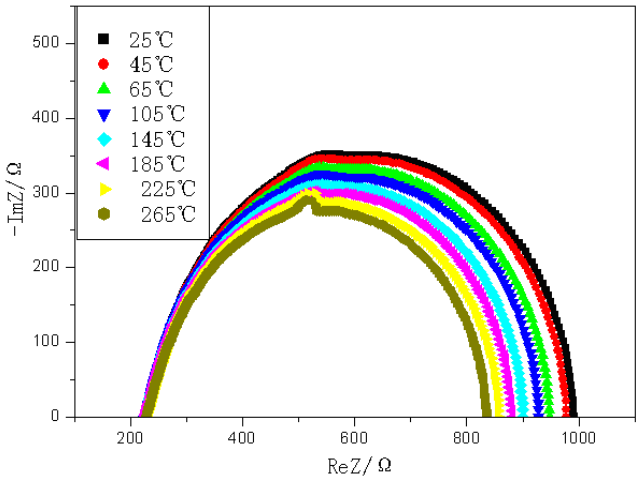

Figure 4. 13 Impedance of swcnt-polyimide composites(0.6%swcnt) at different temperature

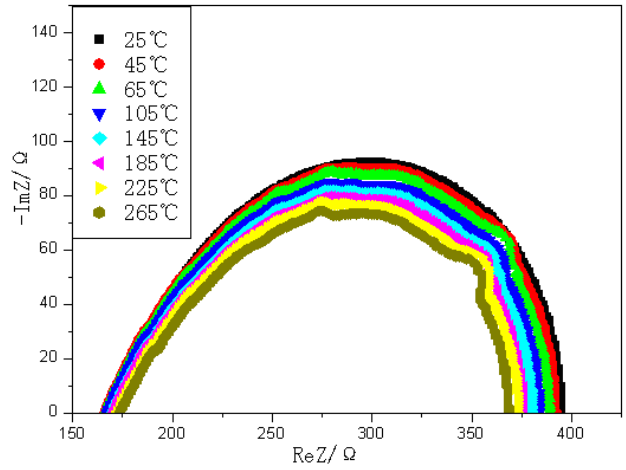

Figure 4. 14 Impedance of swcnt-polyimide composites(0.7%swcnt) at different temperature

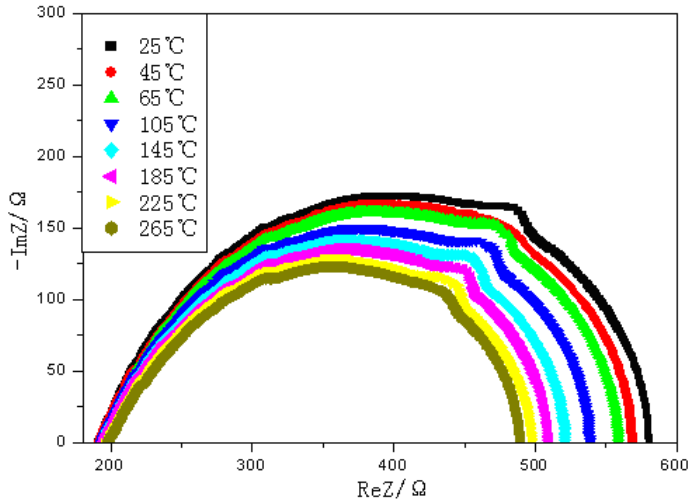

Figure 4. 15 Impedance of swcnt-polyimide composites(0.8%swcnt) at different temperature

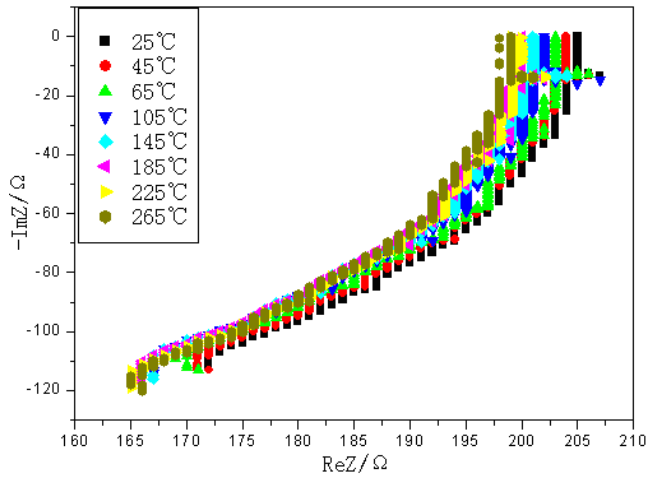

Figure 4. 16 Impedance of swcnt-polyimide composites(1%swcnt) at different temperature

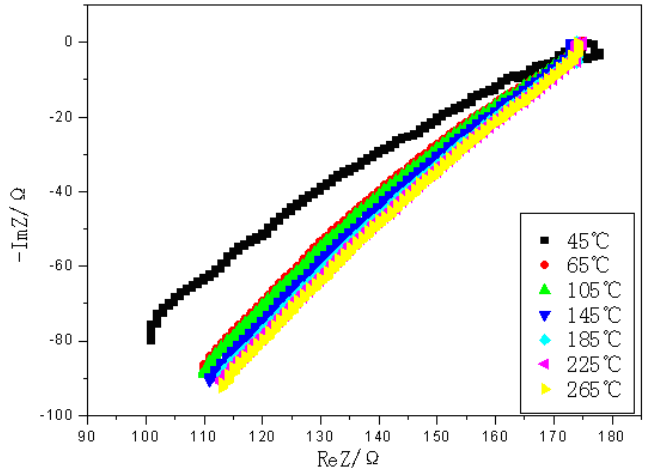

Figure 4. 17 Impedance of swcnt-polyimide composites(1.1%swcnt) at different temperature

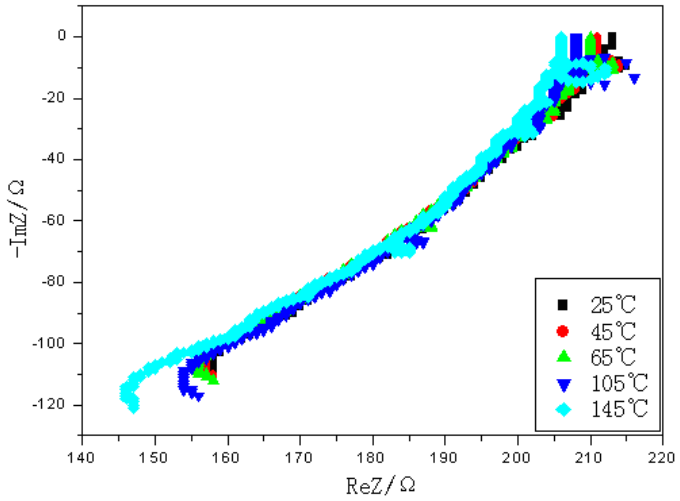

Figure 4. 18 Impedance of swCNT-polyimide composites(1.2%swCNT) at different temperature

It's shown from the figures that with the increase of temperature, the impedance of the sample at low frequency decrease gradually. At higher mixing ratio, this change is more obvious. It's also shown that with the increase of mixing ratio, the impedance at low frequency decrease drastically.

It can be noticed that at 0.05% mixing ratio, the low frequency impedance is not as expected to be lower than that of 0.02% mixing ratio. This is mostly due to the fact that with such low mixing ratio, the swCNT is hard to be distributed evenly. This can be proved by the trend of decreasing low frequency impedance at mixing ratio higher than 0.07%. Test samples with CNT concentration higher than 0.8% do now show complete half circles due to CNT agglomeration, so only temperature coefficient of samples with concentration equal to or lower than 0.8% is included. A better fabrication process is adopted in the following chapter to resolve the agglomeration issue.

As shown in Fig. 4.19, the impedance of nanocomposite thin film can be expressed as an equivalent circuit, when a resister is connected with a capacitor in parallel and then connected with a resister in series.

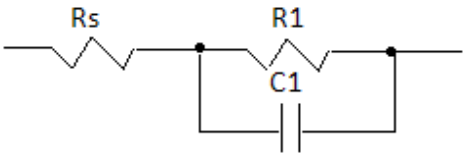

Figure 4. 19 Equivalent circuit of the swCNT nanocomposite thin film

The complex resistance Z of the thin film can be described by the following formula:

$$\mathrm{Z} = \mathrm{R} + iX = Rs + (1/R_1 + i\omega C_1)^{-1} \text{ or } \mathrm{Z} = \left(R_s + \frac{R_1}{1+\omega^2 C_1{}^2 R_1^2} \right) - j\frac{\omega C R_1^2}{1+\omega^2 C_1{}^2 R_1{}^2} \qquad \textbf{Eq. 4. 3}$$

Obviously, when $\omega \to 0$, $\mathrm{Z} = R = R_s + R_1$; when $\omega \to \infty$; $\mathrm{Z} = R_s$,and at the top point of the semicircle, $\omega_o = \frac{1}{C_1 R_1}$. Therefore, the equivalent circuit parameters can be obtained from the measurement of impedance semi-circle. Based on Eq. 4.3, the R_s and R_1 can be calculated separately for each concentration. From Fig. 4.20, it can be seen that before the percolation threshold of 0.7%, most nanocomposites show decreasing resistance for increasing temperature at a rate between 140ppm/℃ and 400ppm/℃. With the increase of CNT concentration, the temperature coefficient increase monotonically to above 1000ppm/℃. Fig. 4.21 shows the temperature coefficient change with increasing CNT concentration.

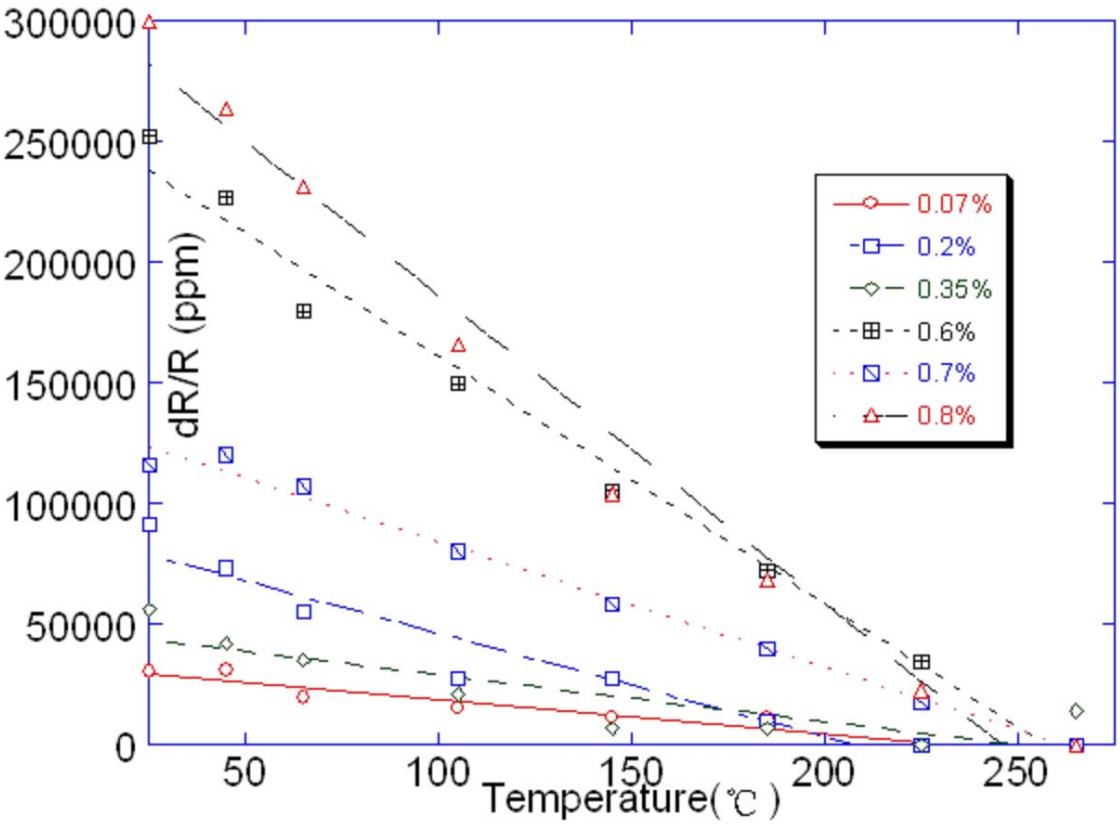

Figure 4. 20 Resistance change with temperature for nanocomposites with different CNT concentration.

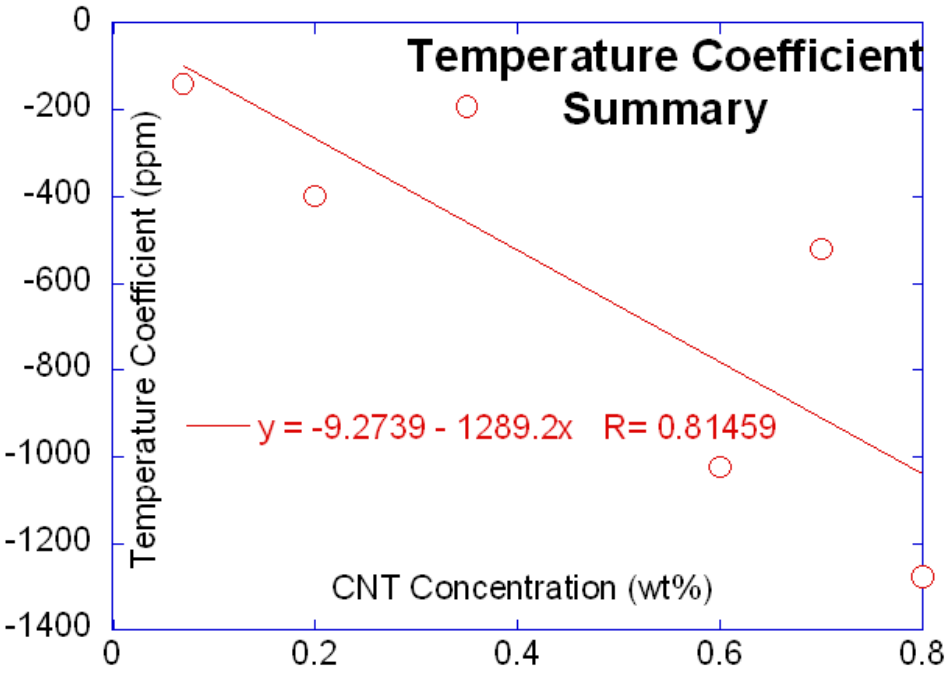

Figure 4. 21 Temperature Coefficient for nanocomposites with different CNT concentration.

4.4 CNT Nanocomposite Response to Strain

The thermal expansion coefficient of quartz is 0.59ppm/℃ [74-75] , For $LiNbO_3$, the z directional thermal expansion coefficient is about 3.4ppm/℃, and 13 ppm/℃ in x/y direction [76]. For polyimide, this coefficient is 55 ppm/℃. So the nanocomposite on piezoelectric substrate will have certain strain from the thermal stress induced by thermal expansion coefficient mismatch. It is thus necessary to investigate into the effect of strain on the nanocomposite resistance.

4.4.1 Test Preparation

To rule out the effect of other parameters, mechanical stress is applied to reach desired strain. The stress application apparatus is AP8214 from Pasco as shown in Fig. 4.22. The apparatus is equipped with a force sensor for stress calculation and a rotary sensor for displacement measurement. The apparatus also includes a data sampling module and communication module, which is used to transfer real time data to computer.

Figure 4. 22 Stress Strain testing apparatus.

Two types of test samples are prepared. One is CNT-PI nanocomposite on top of 100um thick PI film, and connected to measurement equipment by silver paste and copper wire. The other has IDT between nanocomposite and PI film. Fig. 4.23 shows both types of test samples.

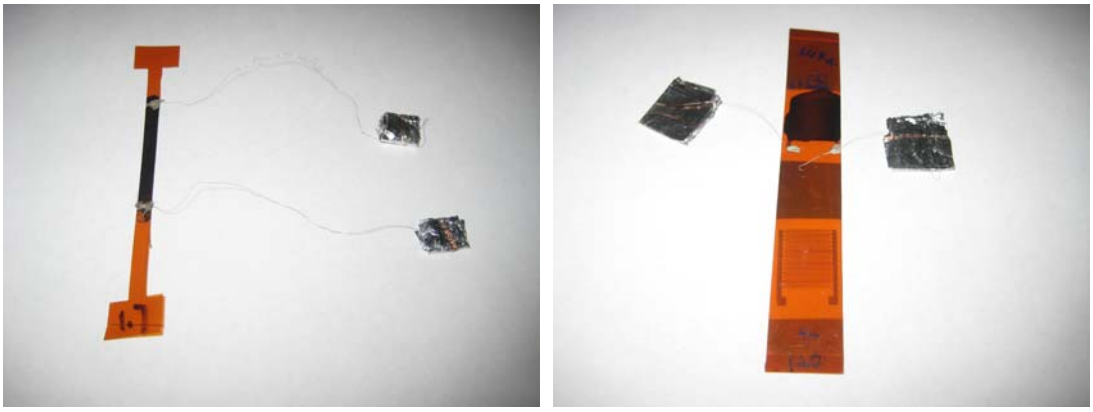

(a) (b)

Figure 4. 23 Test sample. (a) without IDT. (b) with IDT, top one with nanocomposite, bottom one no nanocomposite.

4.4.2 Impedance Measurements

The test samples without IDT are prepared with 5 different CNT concentrations, from 0.8% to 2%. Fig. 4.24 to Fig. 4.28 shows their impedance at strain = 0 to strain = 0.01 respectively. The one with IDT are made with 4 different CNT concentration, from 1.1% to 2%. Fig. 4.29 to Fig. 4.32 shows their impedance between strain = 0 and strain = 0.01respectively.

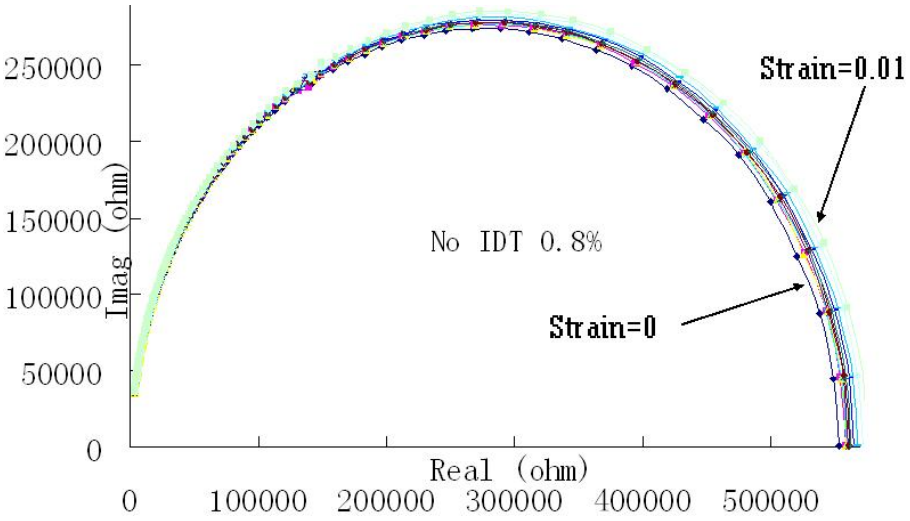

Figure 4. 24 Impedance of test sample without IDT, and with CNT concentration of 0.8%.

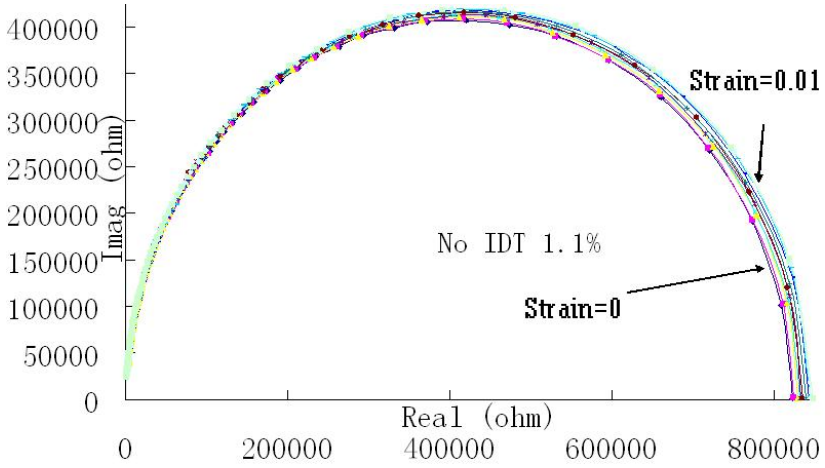

Figure 4. 25 Impedance of test sample without IDT, and with CNT concentration of 1.1%.

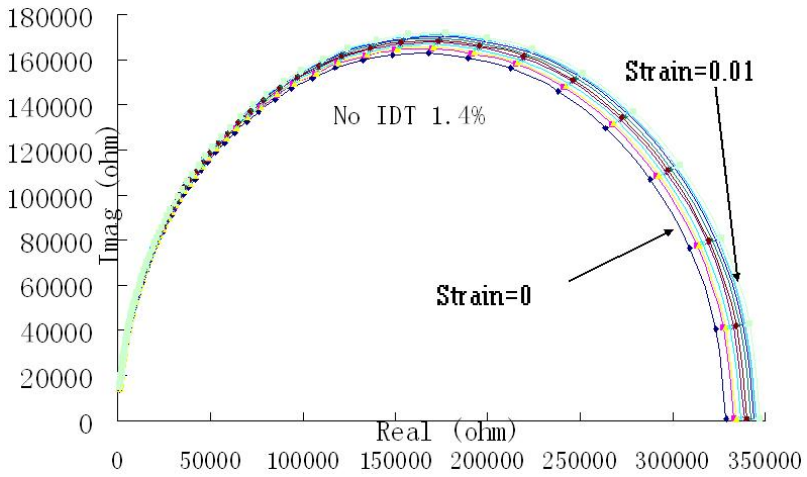

Figure 4. 26 Impedance of test sample without IDT, and with CNT concentration of 1.4%.

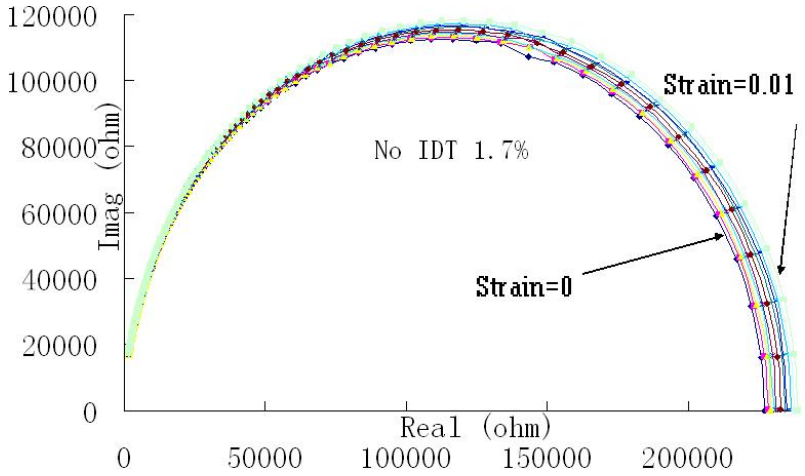

Figure 4. 27 Impedance of test sample without IDT, and with CNT concentration of 1.7%.

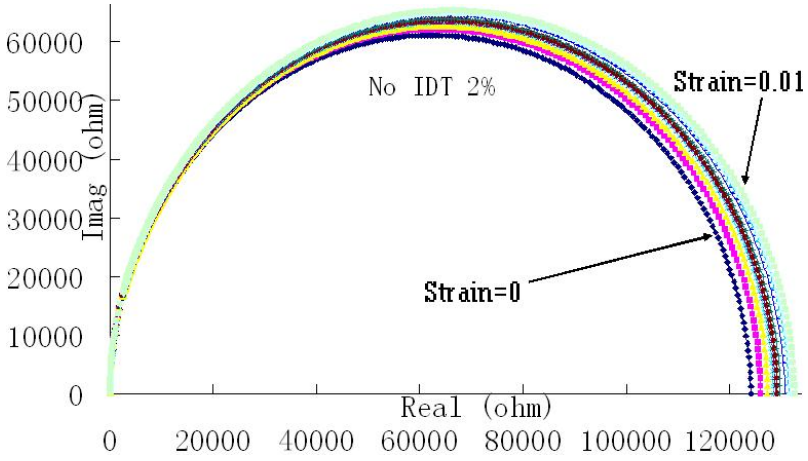

Figure 4. 28 Impedance of test sample without IDT, and with CNT concentration of 2%.

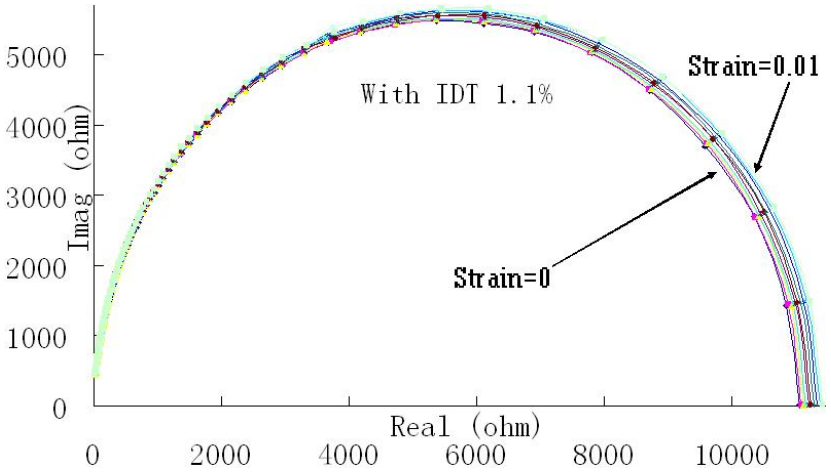

Figure 4. 29 Impedance of test sample with IDT, and with CNT concentration of 1.1%.

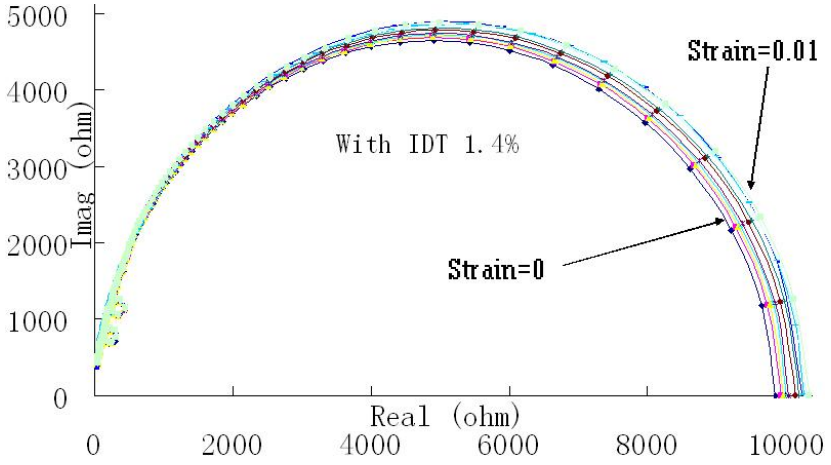

Figure 4. 30 Impedance of test sample with IDT, and with CNT concentration of 1.4%.

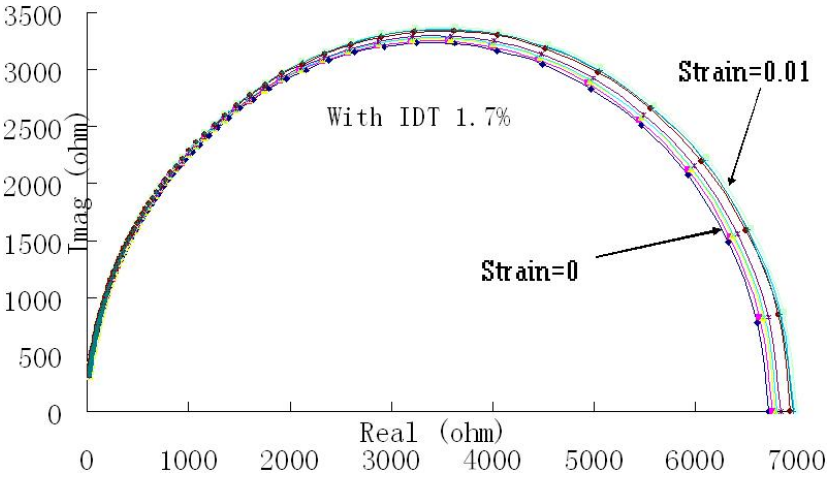

Figure 4. 31 Impedance of test sample with IDT, and with CNT concentration of 1.7%.

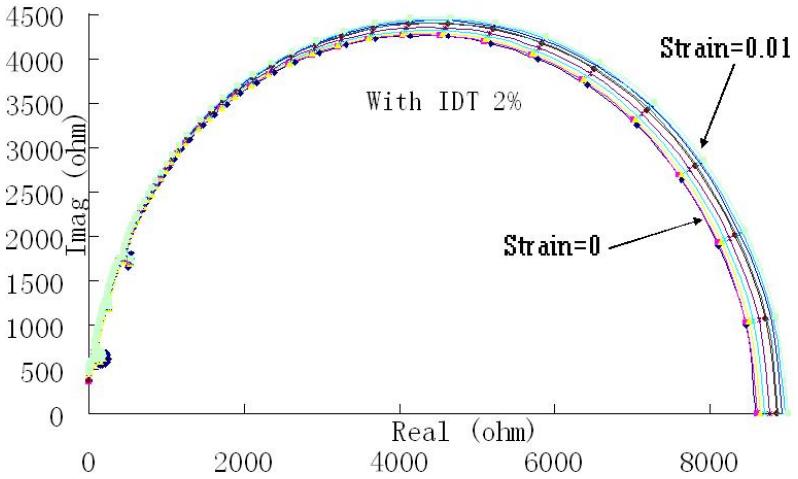

Figure 4. 32 Impedance of test sample with IDT, and with CNT concentration of 2%.

It can been seem that for test sample without IDT, the impedance is a perfect half circle, while for some of the test samples with IDT, such as the test sample with CNT concentration of 1.4% and 2%, the impedance has certain circles on high frequency, which suggests the existence of parasite capacitance.

4.4.3 DC Gauge Factor Test Results

For test results, it can be seen in Fig. 4.33 that, for test samples without IDT, the gauge factor-the ratio of nanocomposite resistance increase to strain-for nanocomposite acquired through DC measurement varies between 3.2 to 5.6 and increases monotonically with the increase of CNT concentration. Fig. 4.34 shows similar results for test samples with IDT under DC measurement. Here, R in the figures means the DC measurement results of the sample, as explained in Equ. 4.3.

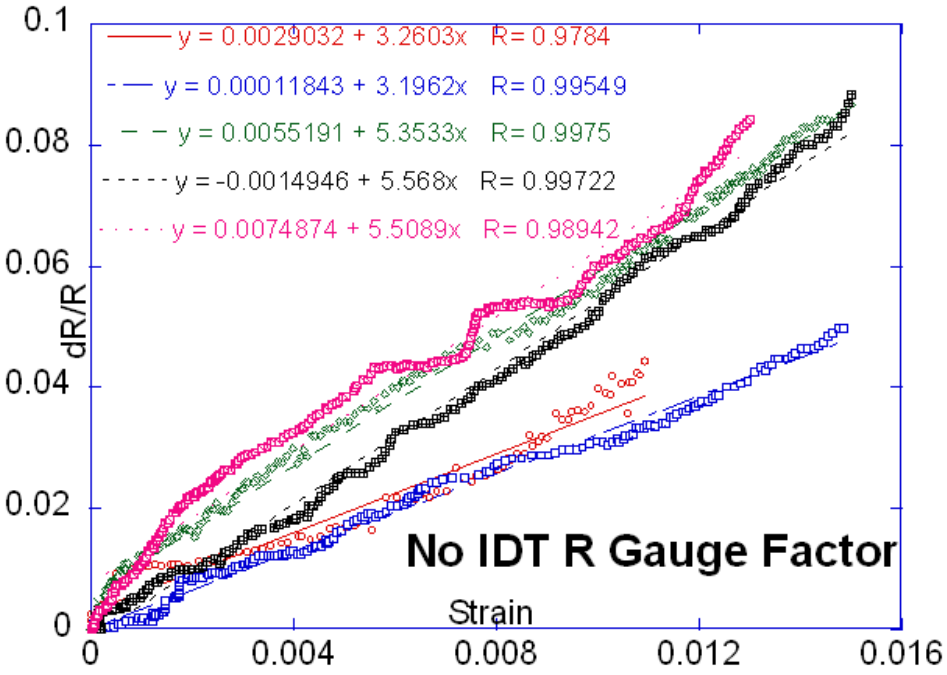

Figure 4. 33 Gauge factor experiment results for test samples without IDT, the trend line equations are for concentrations of 0.8%, 1.1%, 1.4%, 1.7% and 2% from top to bottom.

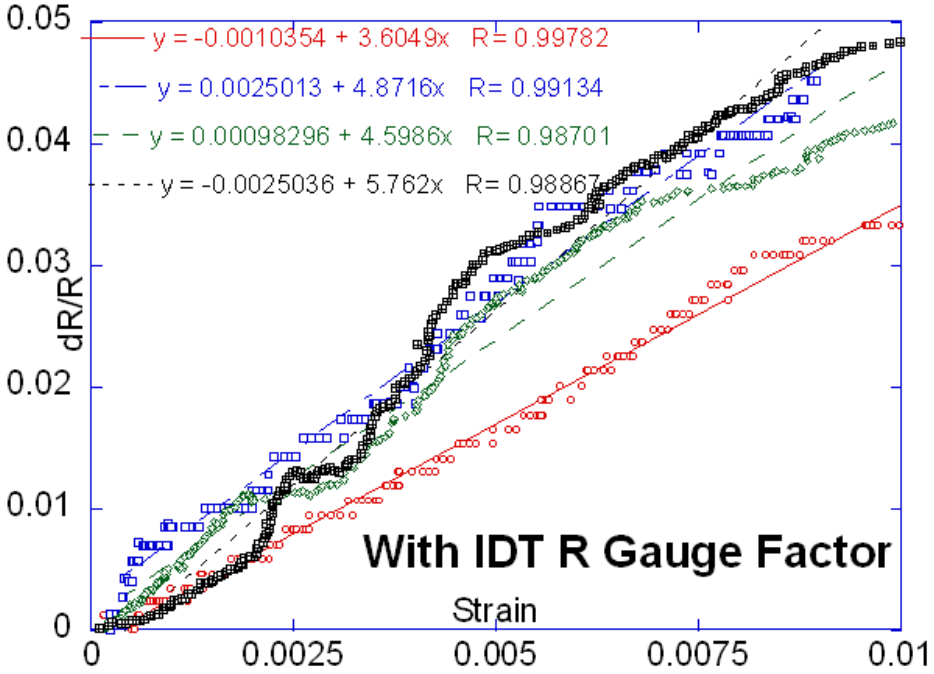

Figure 4. 34 Gauge factor experiment results for test samples with IDT, the trend line equations are for concentrations of 1.1%, 1.4%, 1.7% and 2% from top to bottom.

Based on the comparison of test results from both types of test samples, as shown in Fig. 4.35,

there is no major difference between test samples with and without IDT, and both show certain increase on gauge factor over CNT concentration on the nanocomposite.

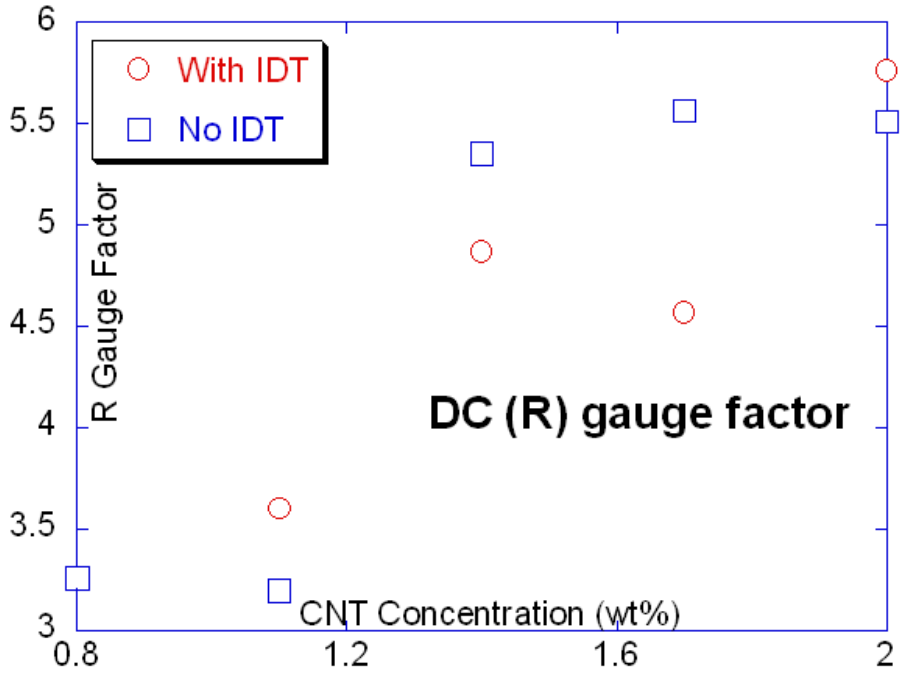

Figure 4. 35 Gauge factor comparison between two types of test samples.

4.4.4 Impedance Parameters Gauge Factor Test Results

The parameters extracted from impedance measurement results are also shown in Fig. 4.36 to Fig. 4.39.

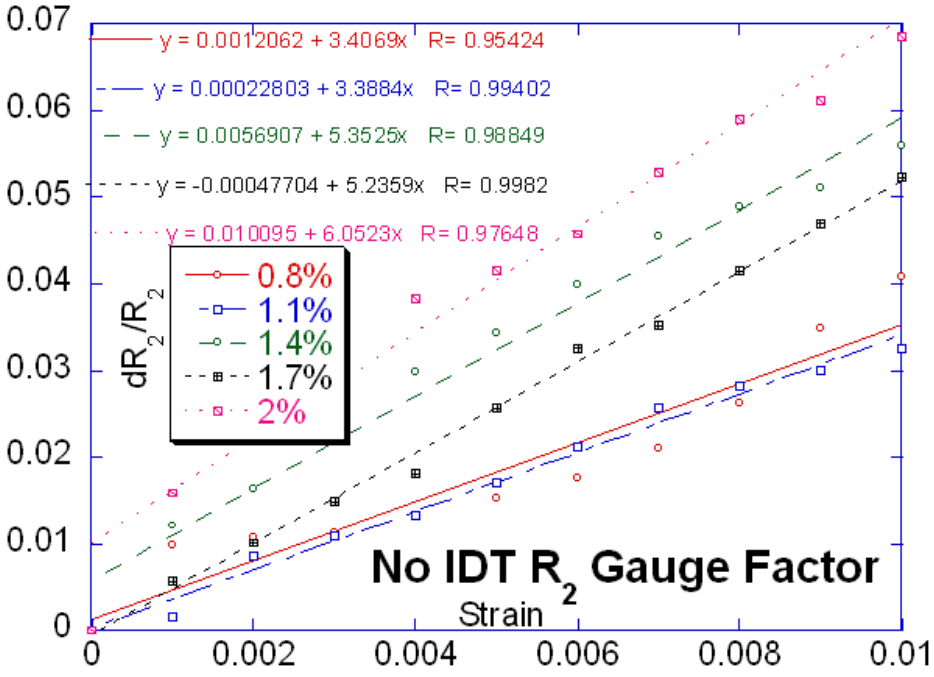

Figure 4. 36 Resistance Gauge factor from impedance measurements for samples without IDTs.

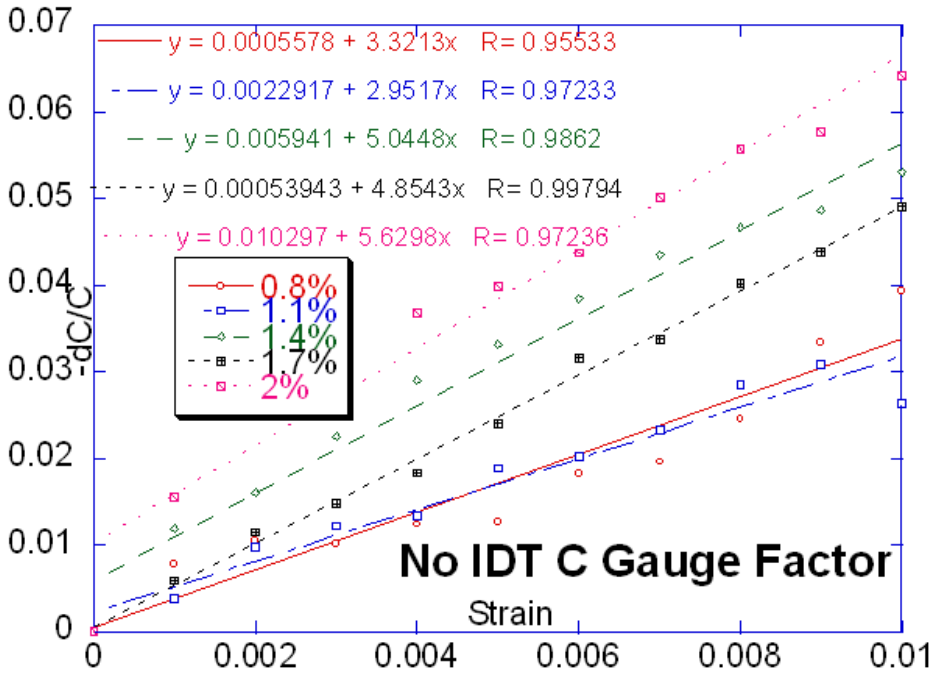

Figure 4. 37 Capacitance Gauge factor from impedance measurements for samples without IDTs.

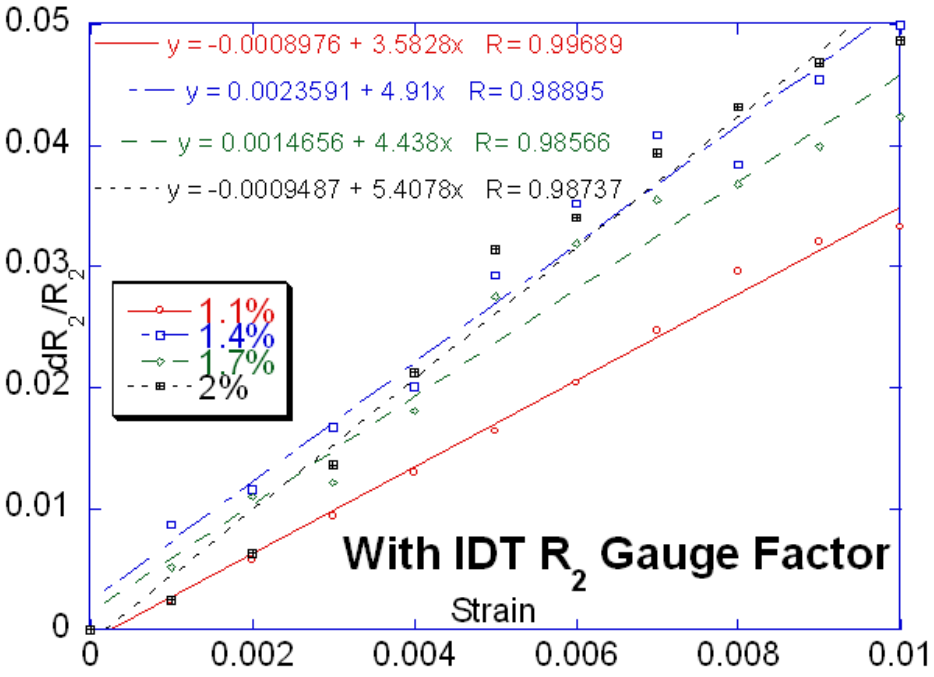

Figure 4. 38 Resistance Gauge factor from impedance measurements for samples with IDTs.

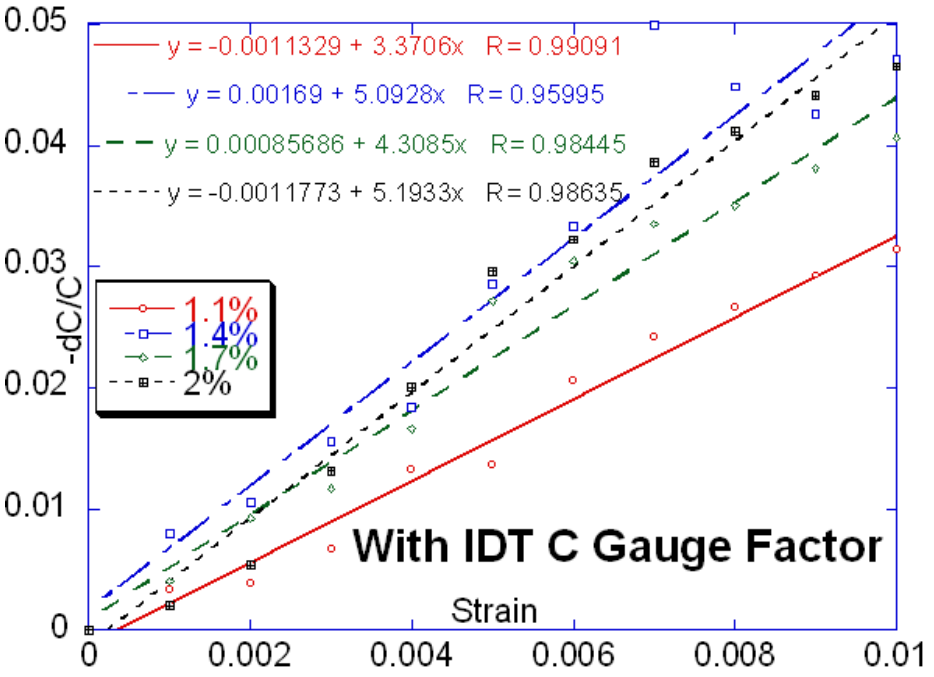

Figure 4. 39 Capacitance Gauge factor from impedance measurements for samples with IDTs.

4.4.5 Gauge Factor Summary

It can be seen that gauge factor from capacitance is generally slightly lower than the gauge factor from the resistance calculation, while the gauge factor from resistance are comparable for DC and impedance measurement, as shown in Fig. 4.40.

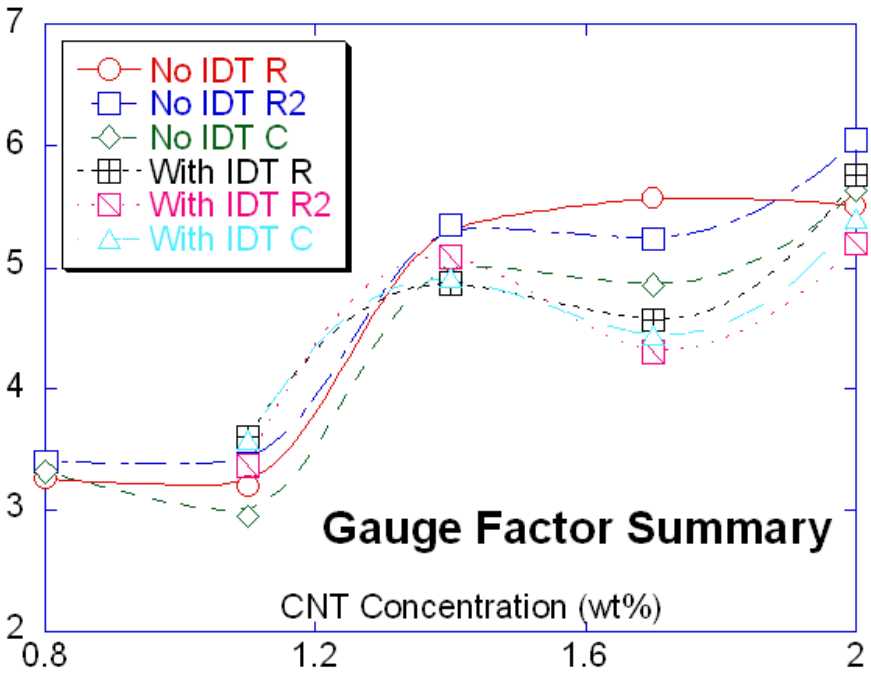

Figure 4. 40 Gauge Factor summary.

4.4.6 Experiment Discussion

The gauge factors from DC resistance measurement and impedance analysis are comparable, which is reasonable since the contact resistance is minimized by careful fabrication process design.

As hypothetically shown in Fig. 4.41, when subject to extensional force, the CNTs might slip and the electron conducting path becomes longer, thus the resistance will increase. The other possible cause is tunneling effect [77]. When the distance between two non-contacting CNTs is small enough, there might be tunneling effect that changes the overall resistivity of the nanocomposite. The tunneling resistance between two neighboring CNTs can be approximated as: [78]

$$R_{tunnel} = \frac{V}{AJ} = \frac{h^2 d}{Ae^2\sqrt{2m\lambda}} \exp\left(\frac{4\pi d}{h}\sqrt{2m\lambda}\right)$$

where J is the tunneling current density, V the electrical potential difference, e the quantum of electricity, m the mass of electron, h the Planck's constant, d the distance between CNTs, λ the height of barrier, and A the cross-sectional area of tunnel. Therefore, when subject to strain, the contacting CNTs might be separated by a small distance, thus introducing the tunneling resistance and increasing the overall resistance. Both factors contribute to the strain sensor resistance performance.

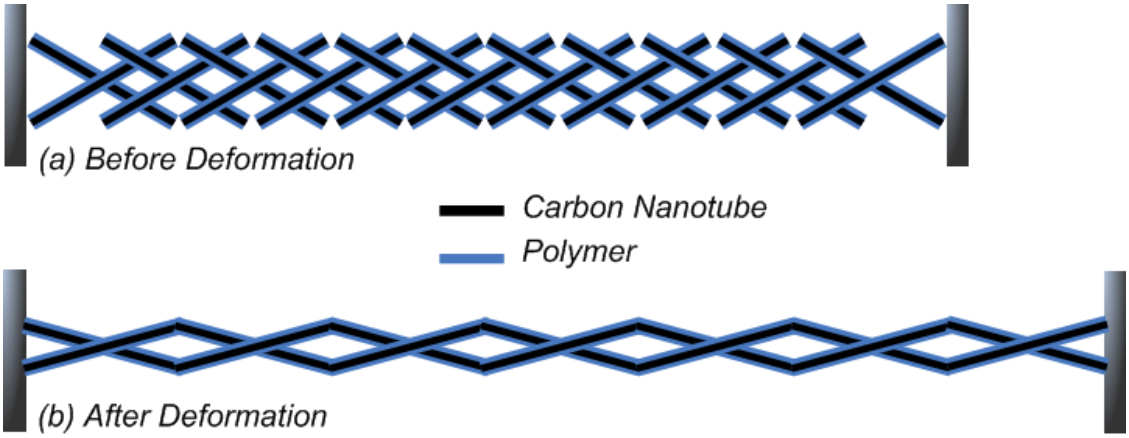

Figure 4. 41 Strain Sensor Working Mechanism.

Based on parallel plate capacitance equation $C = \varepsilon_r \varepsilon_0 A / d$, where ε_r is the dielectric constant, ε_0 is the electric constant, A is cross-sectional area of the strain sensor, and d is the distance between the electrodes, the capacitance will decrease under extensional force because of the decreasing A and increasing d. The gauge factor calculation for the capacitance agrees with the above analysis, as shown in Fig. 4.37 and Fig. 4.39. The gauge factor based on capacitance is slightly lower than that based on resistance, suggesting that resistance measurement is more sensitive.

The experiment results also show that the gauge factor has little improvement beyond CNT concentration 1.4wt%, and considering the percolation threshold range of 1.1wt% to 1.4wt%, it can be concluded that the optimum strain sensor is about 1.4wt% CNT-PI nanocomposite.

And looking back at all the gauge factor measurement results, certain non-linearity can be observed, especially at the beginning of the experiment, i.e. at very small strain. This could be caused by the loading process. The sample was clamped by turning the nuts before experiment, and the process would cause certain twist in the sample, thus the resistance change in the beginning might be the result of a combination of stretch and twist, and the impact might last into bigger strain as well.

4.5 Conclusion

It can be estimated that for CNT-PI nanocomposite on quartz substrate, the thermal expansion

coefficient difference is about 55ppm/℃. So for outdoor temperature variation of 40℃ throughout the year, the thermal caused strain is about 0.2%. Based on the gauge factor experiment results, it can then be estimated that the resistance change purely due to the thermal strain is about 1%. Thus it can be estimated that the temperature coefficient of nanocomposite resistivity is about -1000ppm/℃-5*55ppm/℃=-1375ppm/℃.

The overall effect of temperature change, and its resulting thermal stress, can be summarized as 1000ppm/℃, which accounts for 4% resistance change given that the temperature changes for about 40℃ throughout the year, and the number can be even greater if the temperature changes more. The temperature impact on sensor overall performance can be further calculated and will be introduced in next chapter.

5.0 NANOCOMPOSITE CO_2 RESPONSE AND SAW CO_2 SENSOR PERFORMANCE

5.1 Introduction

The basic principle of CO_2 sensing using CNT-Polymer nanocomposite is the diffusion of the gas into the polymer, causing certain ion exchange, thus causing the resistivity change of the CNT network. It is essential to build a test platform for accurate gas concentration control and fast response of testing, to test the nanocomposite resistance change over different gas concentration as reference, and to estimate the SAW response to sheet resistivity change before final integration of nanocomposite and SAW sensor.

5.2 Gas Testing Platform Construction and Improvement

As shown in Fig. 5.1, the gas testing system comprises of gas sources (Compressed Air gas tank and compressed CO_2 gas tank), flow controllers, one quartz gas testing flow chamber with oven, one sink connected with exhaust gas pipe, one current source measurement unit for thin film conductivity measurement (can be replaced by network analyzer in later characterization process), one computer connected to the current source unit for automatic data collection.

There are three different gases that can be connected to the system at the same time. Each gas pipe is connected to a flow controller before the gas flow into the chamber. The flow controllers are 1179A type Mass-Flo controller from MKS. They have flow rate upper limits of 500sccm, 100sccm and 50sccm, respectively. The controller has an accuracy of 1% of the full scale and a resolution of 0.1% full scale in a 4 digits display. The quartz chamber is part of the F79300 type thermolyne tube furnace from Thermo Scientific. The furnace can generate uniform temperature in the center chamber area between 100℃ up to 1200℃. The quartz chamber has a length of 38” and inner diameter of 2”, which yields a chamber volume of about 2L. Electrical measurement of the testing sample resting in the chamber center is achieved by the build-in electrical connection cord covered by high temperature insulation ceramics.

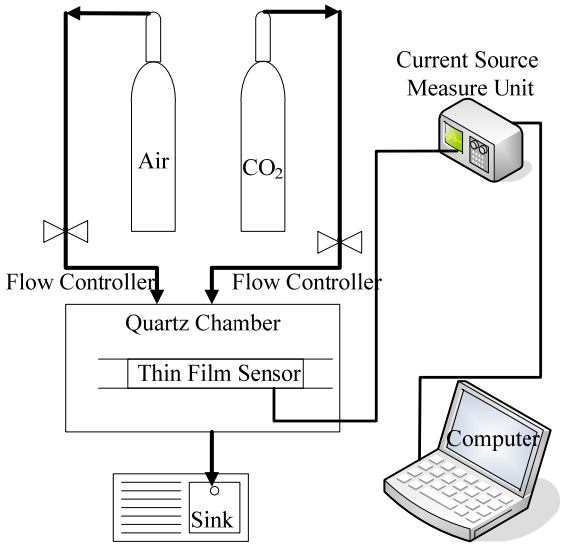

Figure 5. 1 Gas testing system schematic view.

As shown in Fig. 5.2, the measurement of the thin film conductivity is done by type 238 current source measurement unit from Keithley. The current source can output constant current up to 50mA and measure the voltage drop on the test sample or vice versa.

Figure 5. 2 Keithley 238 current source measurement unit.

Automatic data collection is realized by incorporating NI data acquisition card and Labview program. Data sampling rate can be set as high as 1kHz. The data collection interface is shown as Fig. 5.3.

Once the thin film conductivity characterization is completed, the current source measurement unit will be replaced by network analyzer to characterize the performance of the whole sensing system. And the labview program will be accordingly modified for the change.

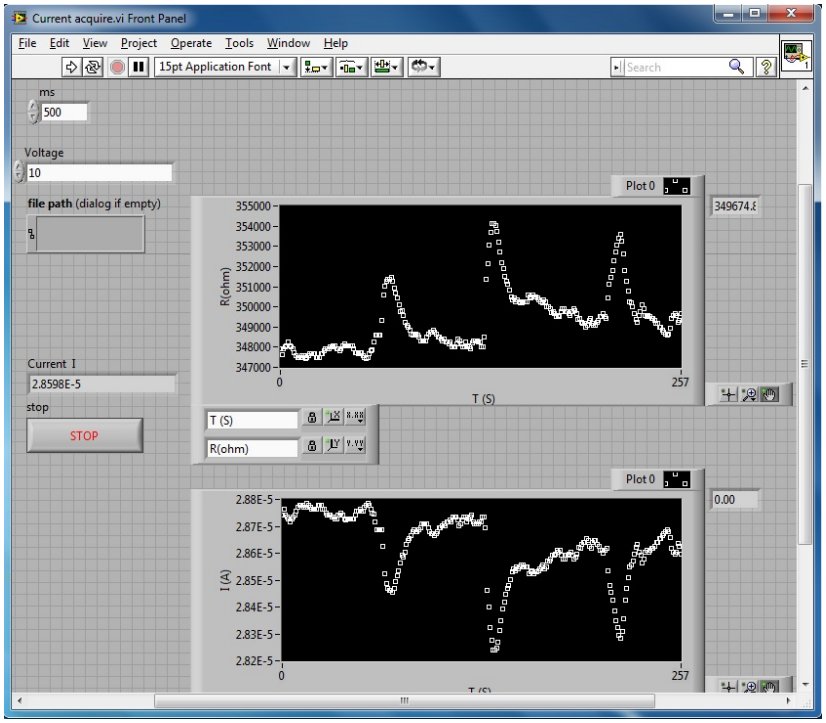

Figure 5. 3 Labview interface for automatic data collection.

The whole system is shown in Fig. 5.4.

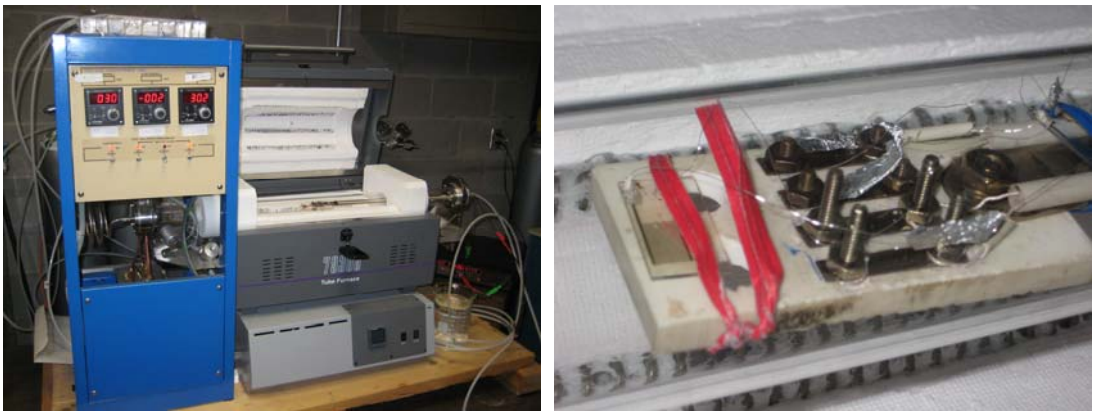

(a) (b)

Figure 5. 4 Gas testing system with automatic data collection. (a) System overview. (b) Test sample.

As shown in Fig. 5.4 (a), the system contains flow control module, quartz gas test tube in oven, resistance measurement module, from left to right. Gas cylinders are connected to flow control module from back. As seen from Fig. 5.4 (b), the test samples are fixed in the fixture inside the test tube, the pads of the test samples are connected to the connectors on the fixture. The connectors are electrically connected out of the cap in the gas exit side of the measurement

module.

The test tube has an inner diameter of 4.8cm, length of 96cm, with the total volume of around 1.7L (1700cc). Experiments contains three major steps: flush – the test tube is flushed with compressed air at 150sccm, 50% CO_2 – the test tube is flushed by 30sccm CO_2 mixing with 30sccm compressed air, and 100% CO_2 – the test tube is flushed by 30sccm CO_2.

Prelim test results show response time for 50% CO_2 is generally around 10 minutes, with the exception of 30 minutes for 1.1wt% thin film. The recover time for 50% CO_2 ranges from 2 minutes to 20 minutes. The response time for pure CO_2 is generally 40 minutes and corresponding recover time is around 20 minutes.

Since the chamber is 38 inches long with 2 inches inner diameter, the total volume the chamber can hold is around 2L. Since the test sample is placed on the center of the chamber, then it can be estimated that for 50% CO_2 it takes around 10 minutes to reach the sample. For pure CO_2 it takes around 20 minutes, and for compressed air flush it takes around 7 minutes.

Based on the above data, it can be estimated that the response time of the thin film for 50% CO_2 is less than 1 minute. The recover time after 50% CO_2 testing ranges from less than 1 minute to more than 10 minutes. The response time for pure CO_2 is around 20 minutes and recover time around 13 minutes.

Since the injection time for various gas filling and flushing process is estimated simply based on flow rate, without considering the effect of diffusion, the calculated response time and recover time is not as accurate as it should be. One solution for faster response and recovery is to reduce the volume of test chamber. In the meantime, the original chamber can still be used to evaluate the resistivity response under different gas concentration, since the original chamber provides better space for complete mixing.

Fig. 5.5 shows the new supplemental chamber for better response time evaluation. The new chamber has an inner diameter of 2” and length of 5”. The total volume it can hold is around 250cc. So 50% CO_2 takes around 1 minute to fully reach the sample. And it takes 2.5 minutes for pure CO_2 case. The flush time will be less than 1minute.

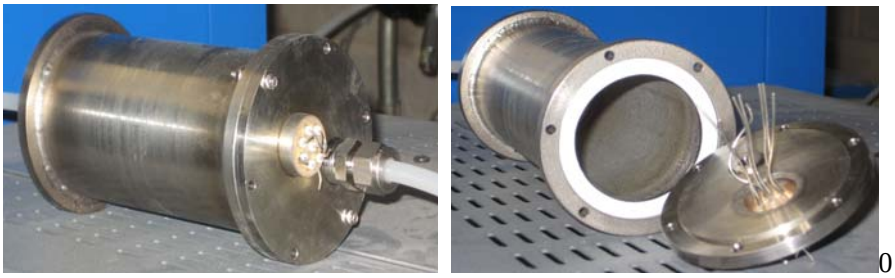 0

Figure 5. 5 Supplemental testing chamber for faster response.

The other way to reduce the response time is to clean out test gas before purging the chamber using vacuum pump. This also proved to be effective.

5.3 SAW CO2 Sensor Assessment [79-80]

Various gas sensors utilizing CNT have been investigated. Some of them are blocks that are made by physically compressing the CNT powder into a mold with desired shape and dimensions. Others are made by mixing CNT powder and polymers or ceramics either by spin-coating or by thermal/electrical evaporation process.

CNTs are p-type conducting material. CNT thin film contains holes as free carrier. When exposed to various gases, such as CO_2, the holes in CNT thin film are neutralized by the electrons from the incoming gas. Then the free carrier is reduced, thus reducing the conductance of the thin film. So the resistance of the thin film is expected to increase upon exposure in CO_2 environment.

A SAW propagating in X direction (which is the case for ST cut Quartz) has a surface electrical potential ϕ which can be expressed as [79-80]:

$$\phi(x,t) = \phi_0 e^{j(\omega t - kx)} \qquad \textbf{Eq. 5. 1}$$

where ω is the angular frequency of the SAW and k is the wave number (For our case, with a period of 60um, the wave number is 52.35E+3).

When there is a conducting film on the propagating path, the propagation characteristics are slightly changed to [79-80]:

$$\phi_0(x) = \phi_0(0) e^{-\gamma x} \qquad \textbf{Eq. 5. 2}$$

where $\gamma = \alpha + j\beta$ is a complex propagation factor arising from the wave/carrier interaction, γ represents the change of the propagation factor compared with unperturbed wave condition. It's assumed that the wave-carrier interaction is weak so that $|\gamma| << k$.

The surface potential ϕ induces charge per unit area ρ_s in the thin film. The current density J_x in the film can be related to surface potential by the continuity equation [79-80]:

$$\frac{\partial J_x}{\partial x} = -\frac{\partial}{\partial t}\left(\frac{\rho_s}{d}\right) \qquad \textbf{Eq. 5. 3}$$

where d is the thickness of the film.

From equation 5.1, the approximation can be made that $\frac{\partial}{\partial x} = -jk$ and $\frac{\partial}{\partial t} = j\omega$, so Equation 5.3 becomes [79-80]

$$\rho_s = \frac{kd}{\omega} J_x \qquad \text{Eq. 5. 4}$$

This induced charge also generate a surface potential ψ which together with ϕ determines the net surface potential. The current density J_x may be related to the total surface potential $(\psi + \phi)$ and the film conductivity σ by [79-80]:

$$J_x = \sigma E_x = -\frac{\partial}{\partial x}(\psi + \phi) = jk\sigma(\psi + \phi) \qquad \text{Eq. 5. 5}$$

where E_x is the electric field.

In equation 5.5, the diffusion current has been neglected.

The surface potential generated by the induced charge is given by [79-80]

$$\psi = \frac{\rho_s}{C_s k} = \frac{\rho_s}{k(\varepsilon_0 + \varepsilon_1)} \qquad \text{Eq. 5. 6}$$

where $C_s k$ is the capacitance per unit area between charges induced at the air-substrate interface by a wave with wave number k, and $C_s = \varepsilon_0 + \varepsilon_1$ where ε_0 is the permittivity of the region above the substrate and ε_1 is that of the substrate. In the case of an anisotropic SAW substrate, $\varepsilon_1 = \sqrt{\varepsilon_{yy}\varepsilon_{zz} - \varepsilon_{yz}^2}$.

Combining equation 5.4 to 5.6, we have [79-80]

$$\rho_s = \frac{jk\sigma d(\varepsilon_0 + \varepsilon_1)\phi}{v_0(\varepsilon_0 + \varepsilon_1) - j\sigma d} \qquad \text{Eq. 5. 7}$$

where $v_0 = \omega / k$ is the unperturbed SAW velocity (3158m/s for ST cut quartz and 4000 for $LiNbO_3$).

The movement of carriers by the SAW potential involves power flow from the wave to the carriers, which is expressed by [79-80]:

$$P_y = -\frac{\partial \rho_s}{\partial t}\frac{\phi_0}{2} = -\frac{j\omega\rho_s\phi_0}{2} \qquad \text{Eq. 5. 8}$$

where P_y is the average power flow per unit area in the direction normal to the surface along which the wave is propagating. Note that the charge moving in phase with ϕ represents stored energy, while the quadrature component arising from carrier lag represents dissipated energy. From equation 5.7 and 5.8, the complex power flow into carrier is [79-80]:

$$P_y = \frac{\omega k \sigma d (\varepsilon_0 + \varepsilon_1) \phi_0^{\,2}}{2\left[v_0(\varepsilon_0 + \varepsilon_1) - j\sigma d\right]}$$ **Eq. 5. 9**

The power that goes into moving carriers in the surface film is extracted from the surface wave. This results in a change in surface wave velocity and attenuation of the wave. An impedance Z_0 can be defined which relates the surface electrical potential ϕ to the total power carried by the wave P_x [79-80]:

$$Z_0 = \phi_0^{\,2} / P_x$$ **Eq. 5. 10**

Associated with the propagating surface wave is an energy density U, representing the total (mechanical and electrical) energy stored per unit surface area. This energy density can be related to the total average power P_x carried by the acoustic beam (of width ω) through the following equation and in turn to the surface potential ϕ through equation 5.10 [79-80]:

$$U = \frac{P_x}{\omega v_0} = \frac{\phi_0^{\,2}}{2 Z_0 \omega v_0}$$ **Eq. 5. 11**

The power supplied by the wave to the carriers is given by the rate of change of U [79-80]:

$$P_y = -v_0 \frac{\partial U}{\partial x} = -\frac{1}{\omega} \frac{\partial P_x}{\partial x}$$ **Eq. 5. 12**

From equation 5.2 and 5.11, the power supplied by the wave may be related to the change in wave propagation through the propagation factor γ [79-80]:

$$P_y = -\frac{\phi_0}{Z_0 \omega} \frac{\partial \phi_0}{\partial x} = \frac{\gamma \phi_0^{\,2}}{Z_0 \omega}$$ **Eq. 5. 13**

The wave impedance Z_0 may be related to the electromechanical coupling factor K^2 used to characterize piezoelectric substrates. K^2 is defined as the ratio of electrical to total wave energy density. Thus [79-80]:

$$K^2 = \frac{U_E}{U} = \frac{\frac{1}{2} k (\varepsilon_0 + \varepsilon_1) \phi_0^{\,2}}{P_x / \omega v_0} = Z_0 k (\varepsilon_0 + \varepsilon_1) \omega v_0$$ **Eq. 5. 14**

From which it's concluded that $Z_0 = K^2 / k(\varepsilon_0 + \varepsilon_1)\omega v_0$.

From equation 5.13 and 5.14, the power supplied by the wave to the charge carriers may be expressed as [79-80]:

$$P_y = \frac{\gamma \phi_0{}^2 k(\varepsilon_0 + \varepsilon_1) v_0}{K^2} \qquad \textbf{Eq. 5. 15}$$

Noting that the propagation factor $\gamma = \alpha + j\beta$, the complex power supplied by the wave from equation 5.15 can be equated to the complex power taken up by the carriers from equation 5.9.

Recalling that $v_0 = \omega / k$ and equating imagine parts we have the fractional velocity perturbation [79-80]:

$$\frac{\Delta v}{v_0} \cong -\frac{\beta}{k} = -\frac{K^2}{2} \frac{(\sigma d)^2}{(\sigma d)^2 + v_0{}^2 (\varepsilon_0 + \varepsilon_1)^2} \qquad \textbf{Eq. 5. 16}$$

While equating the real parts we have the attenuation per wave number [79-80]:

$$\frac{\alpha}{k} \cong \frac{K^2}{2} \frac{v_0(\varepsilon_0 + \varepsilon_1)\sigma d}{(\sigma d)^2 + v_0{}^2 (\varepsilon_0 + \varepsilon_1)^2} \qquad \textbf{Eq. 5. 17}$$

Equation 5.17 and 5.18 describe the velocity and acousto-electric attenuation change due to the change of the film conductivity on SAW propagation path. When considering the total surface wave velocity, we know from perturbation theory that [79-80]:

$$\frac{\Delta v}{v_0} = \frac{1}{v_0}\left(\frac{\partial v}{\partial m}\Delta m + \frac{\partial v}{\partial c}\Delta c + \frac{\partial v}{\partial \sigma}\Delta \sigma + \frac{\partial v}{\partial \varepsilon}\Delta \varepsilon + \frac{\partial v}{\partial T}\Delta T + \frac{\partial v}{\partial p}\Delta p\right) \qquad \textbf{Eq. 5. 18}$$

Here m is the variables mass, c is the stiffness, T is the temperature and p is the pressure. Together with unperturbed wave velocity v_0, conductivity σ and dielectric coefficient ε, these are the major components that can cause SAW velocity change, thus frequency shift.

Based on the equation and the background of current project, other than conductivity, we also need to consider the effect of dielectric coefficient and mass change on frequency shift. From Eq. 5.18, the frequency response of quartz and LiNbO3 sensors can be estimated as shown in Fig. 5.6.

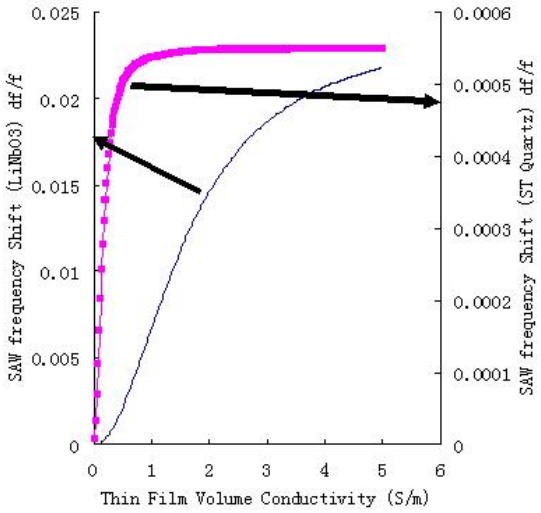

Figure 5. 6 SAW frequency shift corresponding to the thin film conductivity.

As can been seen from Fig. 5.6, the best combination of SAW substrate and sensing film is $LiNbO_3$ and nanocomposite with 1.6S/m sheet conductivity.

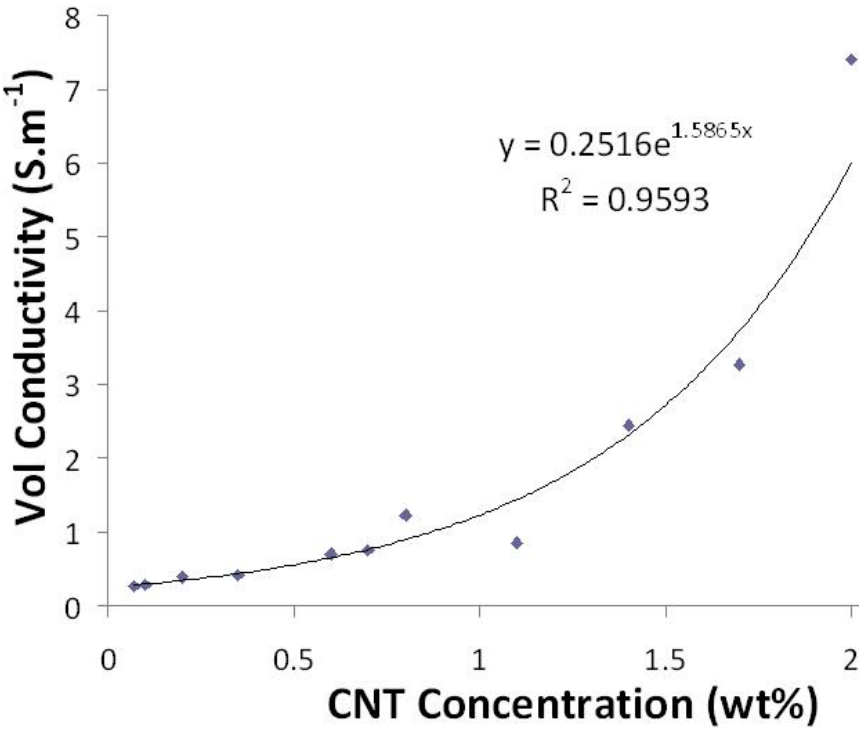

Figure 5. 7 Volume Conductivity of nanocomposite with different CNT concentration.

From Fig.5.7, it can be seen that nanocomposite thin film with volume conductivity of 1.6S/m can be fabricated with CNT concentration between 1.1wt% and 1.4wt%. More specifically, it can be calculated based on the trend line for volume conductivity that when CNT concentration is

1.166wt%, the volume conductivity of the nanocomposite thin film will be 1.6S/m.

5.4 CNT-PI Nanocomposite Response to CO_2

Due to the agglomeration phenomenon for higher CNT concentration, a new process for CNT-PI mixing is developed. Gas response is tested nanocomposite with new recipe.

5.4.1 Nanocomposite Fabrication

To further improve the dispersion of CNT in mixture solution, the fabrication process is improved in some of the steps. First, dimethylformamide (DMF) is used to disperse CNT. DMF is believed to be good candidate for CNT dispersion because of their chemical compatibility. CNT is mixed with DMF with 1:1000 weight ratio. The mixture is then agitated by ultrasonic convertor using Misonix ultrasound liquid processors. The CNTs are well dispersed in the DMF solution after 90 minutes ultrasound at 70W. In the meantime, polyimide (PI) are diluted into n-Methyl-2-pyrrolidone (NMP) with weight ratio of 1:2. Magnetic mixing bar is used to mix the solution before the solution is put into ultrasonic water bath. Solution with different CNT concentrations are made by joining the CNT solution and PI solution at different ration. For 0.8wt% solution, the ratio of CNT solution to PI solution is 1000:376. For 1.1wt% solution, the ratio is 1000:271.3. For 1.4wt% solution, the ratio is 1000:215.2. For 1.7wt% solution, the ratio is 1000:177.4. For 2wt% solution, the ratio is 1000:151. The solution is ready for use after the mixture of CNT solution and PI solution is brought into ultrasonic water bath for 60 minutes.

The solution with different CNT concentration is then dispensed on the sensor surface and heated at 120℃ on hotplate for 90s. The thin film is then fully cured at 350℃ for 30 minutes in the oven.

5.4.2 Nanocomposite Gas Response

After conductivity measurement, the nanocomposite thin films with different CNT concentration are placed in the testing chamber. The resistance of the thin film is measured under three different conditions: compressed air, 1:1 mixture of compressed air and CO_2, pure CO_2.

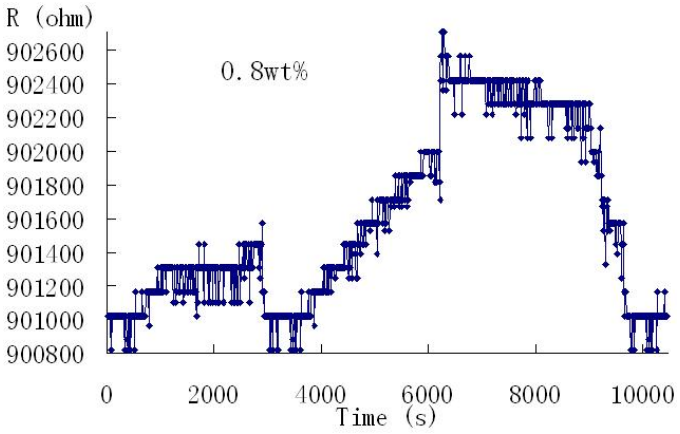

Figure 5. 8 Real time CO_2 response .for nanocomposite thin film with 0.8wt% CNT concentration.

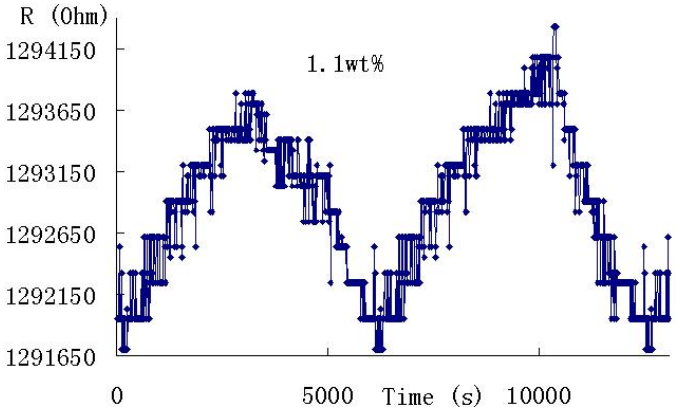

Figure 5. 9 Real time CO_2 response .for nanocomposite thin film with 1.1wt% CNT concentration.

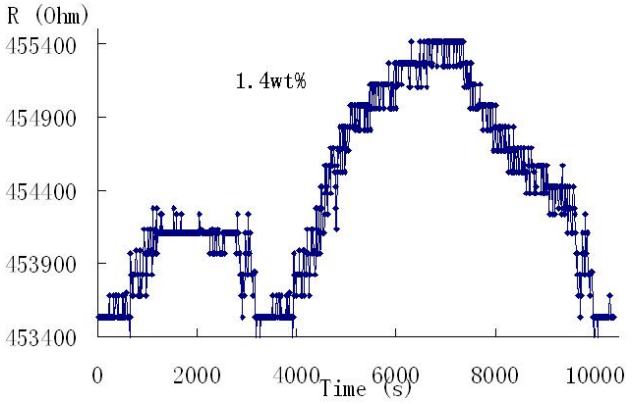

Figure 5. 10 Real time CO_2 response .for nanocomposite thin film with 1.4wt% CNT concentration.

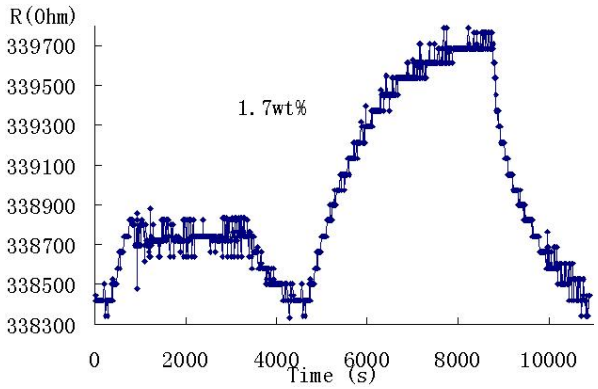

Figure 5. 11 Real time CO_2 response .for nanocomposite thin film with 1.7wt% CNT concentration.

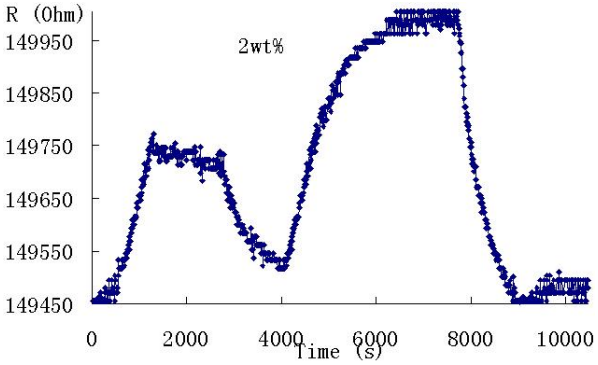

Figure 5. 12 Real time CO_2 response .for nanocomposite thin film with 2wt% CNT concentration.

Fig. 5.8 to Fig. 5.12 shows the compiled real time response of the thin film with different CNT concentration under the testing conditions. The relative change of resistivity for the nanocomposite thin films with different CNT concentration is shown in Fig. 5.13.

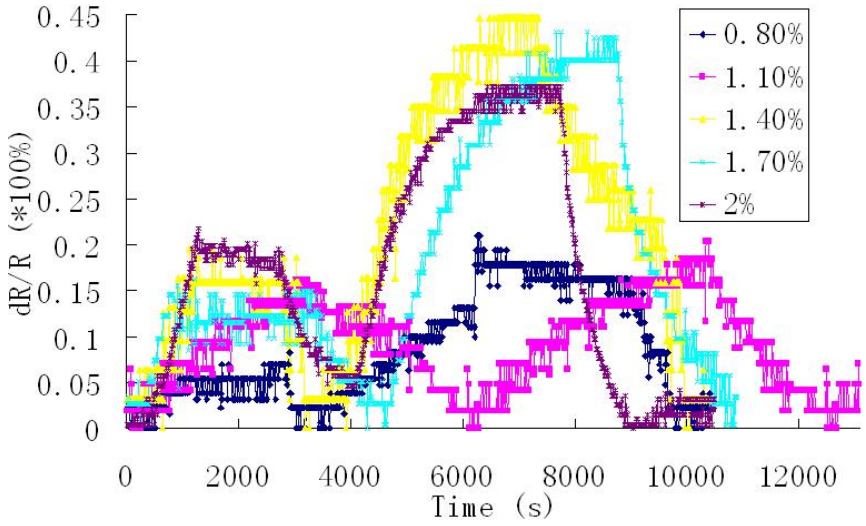

Figure 5. 13 Relative resistivity change of nanocomposite thin films.

At the beginning of the first step in each figure, compressed air with flow rate of 50sccm and CO_2 of 50sccm are introduced into the system through flow controller. After the resistance of the thin film reaches maximum value and stays for certain time, the flow controller is switched to compressed air of 140sccm to flush the chamber. Then CO_2 of 50sccm is connected to produce complete CO_2 environment. Again the chamber is flushed with compressed air after the resistance of the thin film reaches maximum value and becomes stable. Every time the chamber is flushed, vacuum pump is turned on for 2min to evacuate the gas in the chamber.

Following the same procedure, test specimen with CNT concentration of 1.1%, 1.4%, 1.7% and 2% are tested with pure air, 1% CO2 air mixture, 5%, 10%, 20%, 50% and pure CO_2. The test results show similar response for different CNT concentration, as illustration in Fig. 5.14.

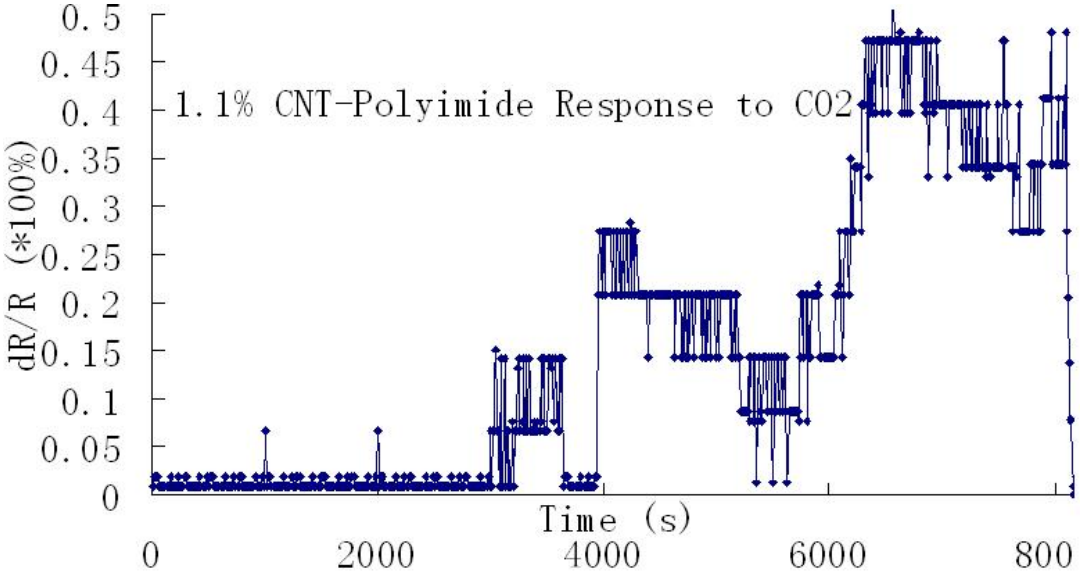

Figure 5. 14 Relative resistivity change of CNT-PI nanocomposite thin films with 1.1% CNT

Fig. 5.14 shows the case for 1.1% CNT nanocomposite. The resistance of the thin film barely changes at 1%, 5% and 10% CO_2 concentration. The response at 20% CO_2 concentration is 0.1%, and 0.2% for 50% CO_2 concentration, 0.4% for pure CO_2, which is comparable with previous results.

It can be estimated that the sensor will have 500 Hz frequency change under 20% CO_2 concentration, when the base frequency of the system is 52.63MHz. It poses great difficulty at extracting such frequency change from the background noise.

5.4.3 Nanocomposite Gas Response Improvement

As seen from above figures, the resistivity change for pure CO_2 is less than 0.4%. The test results suggest PI is not ideal candidate as CO_2 sensing polymer. From chemistry point of view, CO_2 is generally an unreactive molecule, which only combines with primary and secondary amines at room temperature and atmosphere pressure to form carbamate, which is essentially an acid-base equilibrium. The best candidate with primary and secondary amines is Polyethylenimine (PEI), which is a highly branched polymer with 25% primary, 50% secondary and 25% tertiary amino groups.

The CNTs are dispersed into DMF solution using similar process from previous report. The mixing ratio is controlled so that the CNT concentration of the fabricated solution is the same with the CNT-PI-DMF-NMP solution. Solutions with 1.1%, 1.4% and 1.7% CNT concentration are made respectively.

PEI is purchased from Aldrich with mean molecular weight of 25000. It's known that the mixture of PEI with starch will have better response to CO_2 compared to pure PEI, due to the hygroscopic nature of starch. Two different starch from corn and potato are tested respectively.

Starch are mixed with water using magnetic stir bar at elevated temperature around 100℃. The solution is then mixed with PEI.

The CNT-DMF solution from previous step is applied to the surface of the test sample and let dry. The sample is then immersed into the PEI-starch solution for 12 hours, and followed by rinse in water. After the water evaporates, the sample will have a CNT network with 10nm thick PEI-starch coating.

The samples are tested under air, 1%, 5%, 10%, 20%, 50% and pure CO_2 respectively. Test results are shown from Fig.5.15 to Fig. 5.17

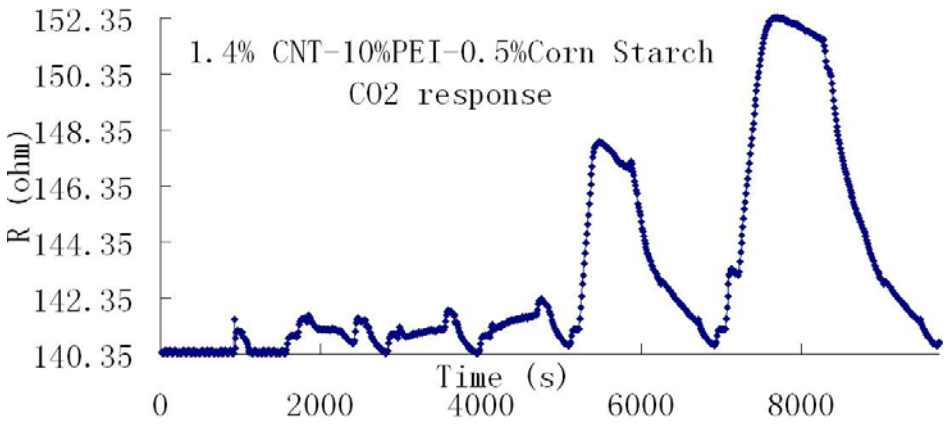

Figure 5. 15 Relative resistivity change of CNT-PEI nanocomposite thin films with 1.4% CNT and 0.5% corn starch

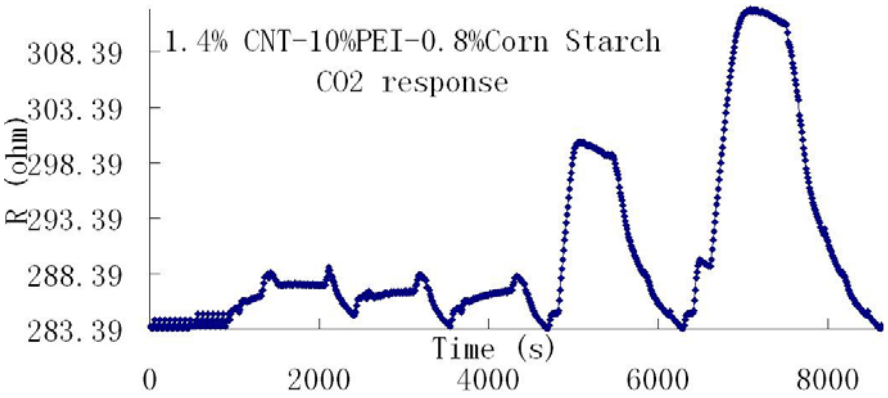

Figure 5. 16 Relative resistivity change of CNT-PEI nanocomposite thin films with 1.4% CNT and 0.8% corn starch

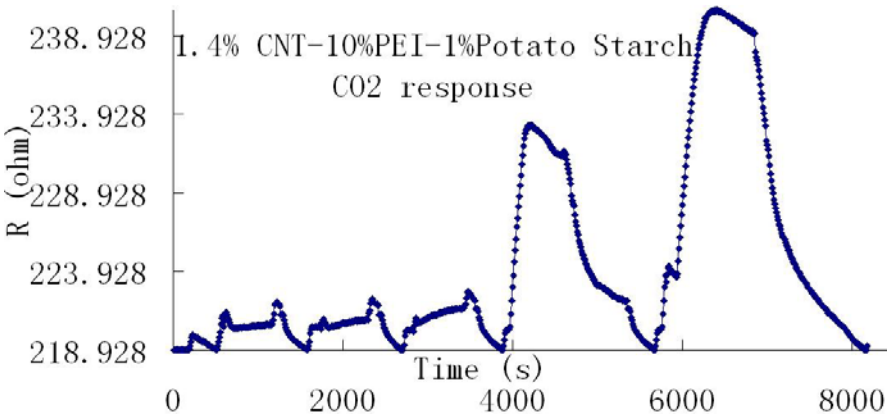

Figure 5. 17 Relative resistivity change of CNT-PEI nanocomposite thin films with 1.4% CNT with 1% potato starch

From Fig. 5.18, it can be seen that there is noticeable response at different concentration as low as 1% CO_2. The test results also suggest that corn starch and potato starch are comparable in CO_2 response enhancement.

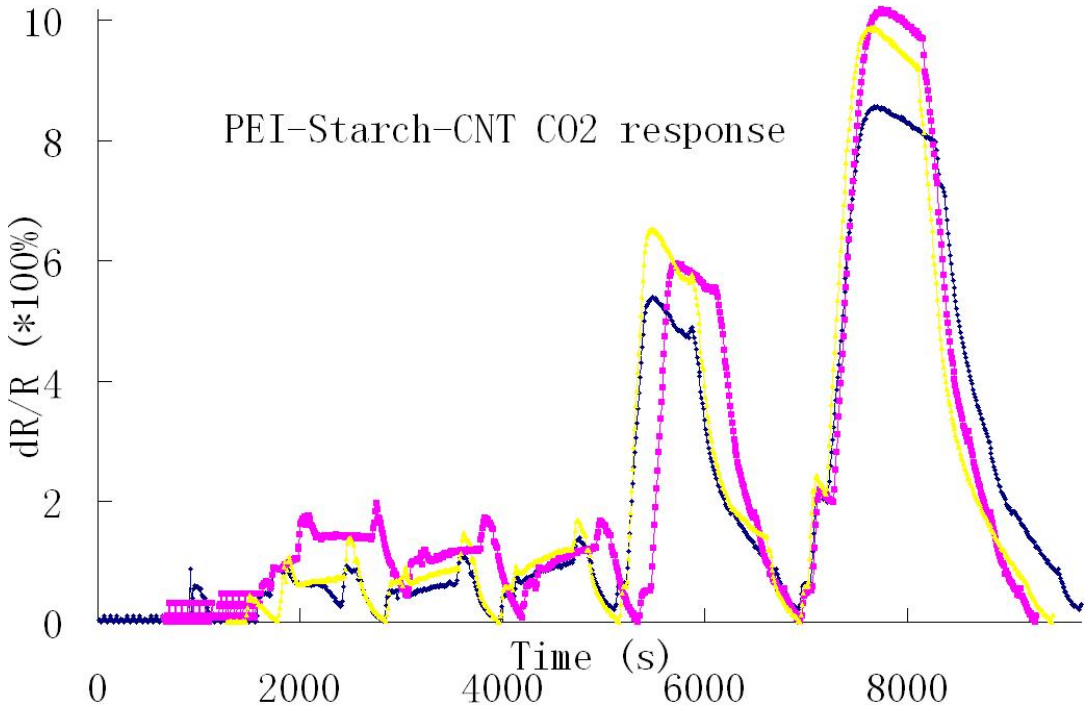

Figure 5. 18 Relative resistivity change of CNT-PEI nanocomposite thin films with 1.4% CNT

It can be summarized that CNT-PEI nanocomposite is over 20 times sensitive compared to CNT-PI nanocomposite. The thin film also has response to low concentration CO_2. The details are shown in Fig. 5.19.

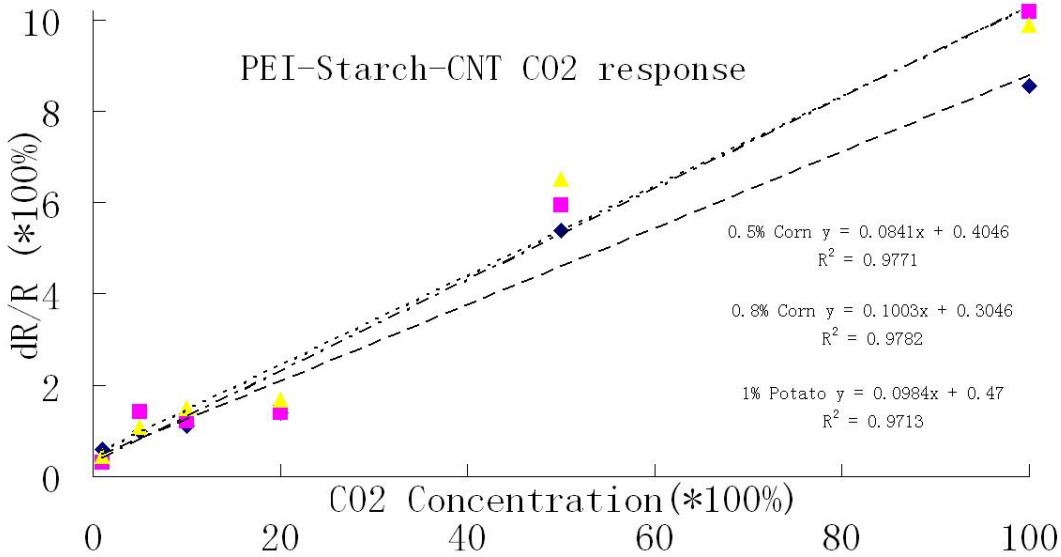

Figure 5. 19 Relative resistivity change of CNT-PEI nanocomposite thin films with 1.4% CNT

5.5 SAW Sensor CO_2 Response Assessment and Characterization

5.5.1 SAW Sensor Performance Assessment

Based on Fig. 5.6 and Fig. 5.19, the nanocomposite thin film response to CO_2 can be estimated as shown in Fig. 5.20. The frequency change ranges from about 50ppm at 1.0% CO_2 concentration, to over 1000ppm for pure CO_2.

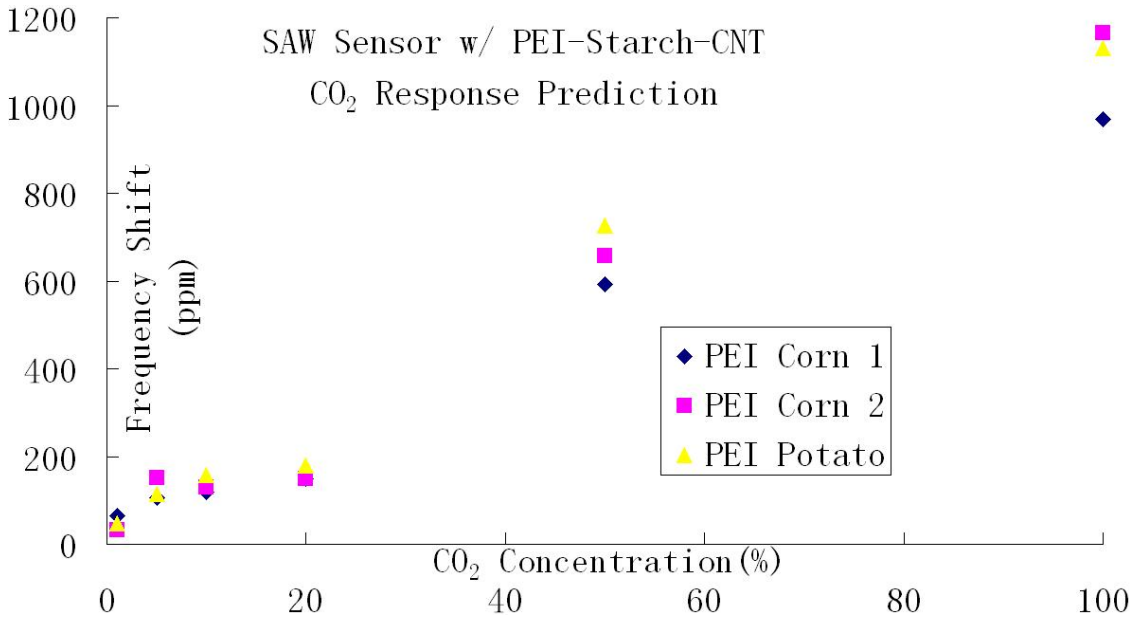

Figure 5. 20 SAW frequency shift prediction at different CO_2 concentration.

Fig. 5.21 shows the predicted frequency response in log scale.

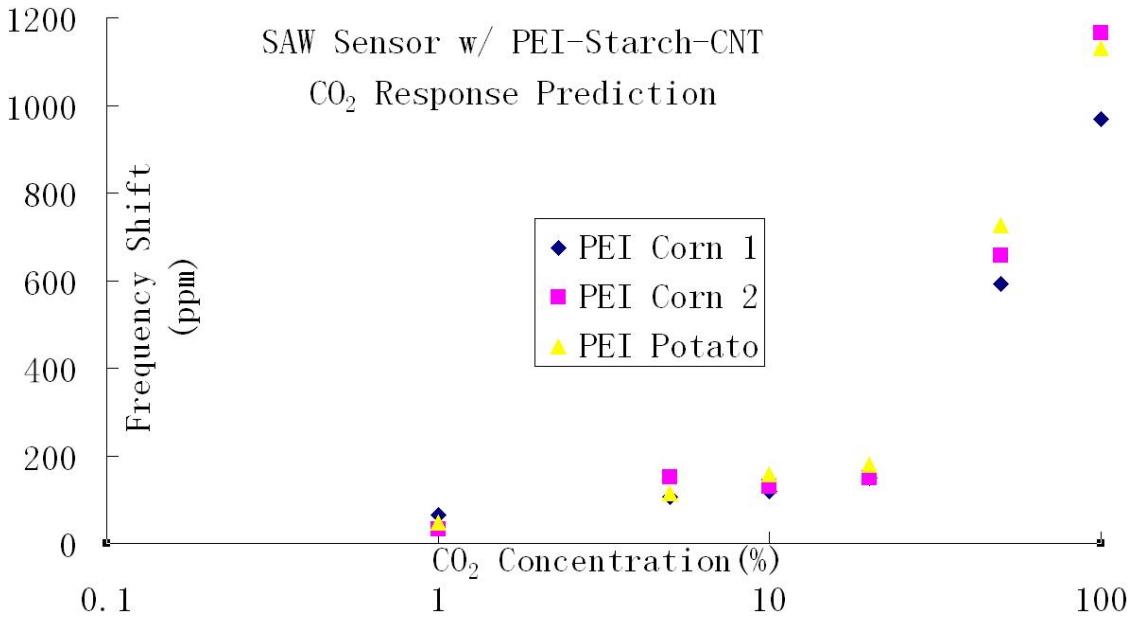

Figure 5. 21 SAW frequency shift prediction at different CO_2 concentration in log scale.

5.5.2 SAW Sensor Fabrication

Two methods are adopted in sensor fabrication: photo lithography and shadow mask technology. 128° YX cut $LiNbO_3$ are selected for its excellent coupling coefficient (5.5% compared to 0.16% of ST cut quartz) and low transmission loss (0.26dB/cm compared to 0.95dB/cm of ST cut quartz). Surface acoustic wave velocity on $LiNbO_3$ is 4000m/s.

First attempt of photo lithography is lift-off. During the process, photo resist is coated on the substrate surface using spin-coater and patterned under mask aligner. The pattern normally has opposite polarity so the IDT area is exposed and other area is covered by photo resist after developing. Thin layer of metal such as gold is then coated on top of the patterned surface. After cleaned in acetone, the metal on top of photo resist will peel off as photo resist dissolve gradually into acetone. Only the metal in IDT area remains. This attempt failed because $LiNbO_3$ substrate is transparent. During patterning process, most light go through the substrate and only a small portion of light is absorbed by the photo resist. This caused under-exposure and most of the photo resist is removed during developing process.

The second attempt of photo lithography is etching. After substrate cutting and cleaning, metal was coated on the substrate and followed by photo resist. Since the substrate is covered by metal film, most light during patterning process is absorbed by photo resist and thus the photo resist on the IDT area remained after developing. The substrate is then immersed in metal etchant and the metal not covered by photo resist is removed completely. The remaining photo resist on IDT is

then removed in RIE (reactive-ion-etching).

In this process, 1500A thick gold is coated on the $LiNbO_3$ substrate. Micro posit S1805 is used as photo resist. After spin-coating at 4000rpm for 45s, the photo resist is 0.6um thick. The remaining photo resist are removed in RIE, with 48sccm O_2, 2sccm CH_4. The power of plasma is kept at 200 watts and the pressure is 250 mTorr. The RIE process lasted for 120s.

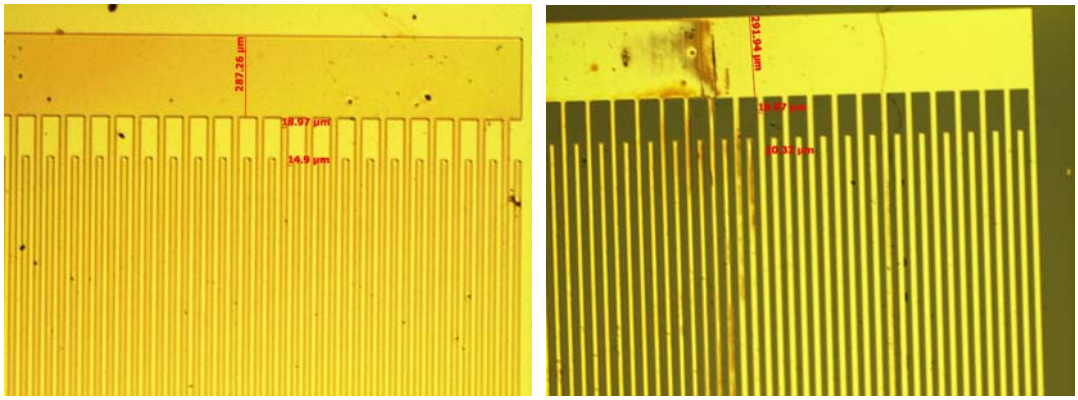

(a) (b)

Figure 5. 22 (a) $LiNbO_3$ substrate right after patterning. (b) LiNbO3 substrate after gold etching and RIE cleaning.

Fig. 5.22 shows the microscopic pictures of $LiNbO_3$ substrate after patterning and after RIE cleaning. It can be seen that the IDT has finger width of about 18um and spacing of about 15um. The estimated resonant frequency of the sensor is 60.6 MHz.

The other approach of IDT fabrication is shadow mask process. A shadow mask is a thin metal sheet with opening of IDT. The opening is normally achieved by laser cutting or chemical etching. During the IDT fabrication process, the $LiNbO_3$ substrate is covered by the shadow mask and exposed in metal coating system. Only the opening area is coated with metal. This method is relatively simple and cost effective, except that the feature size is relatively big compared to photo lithography.

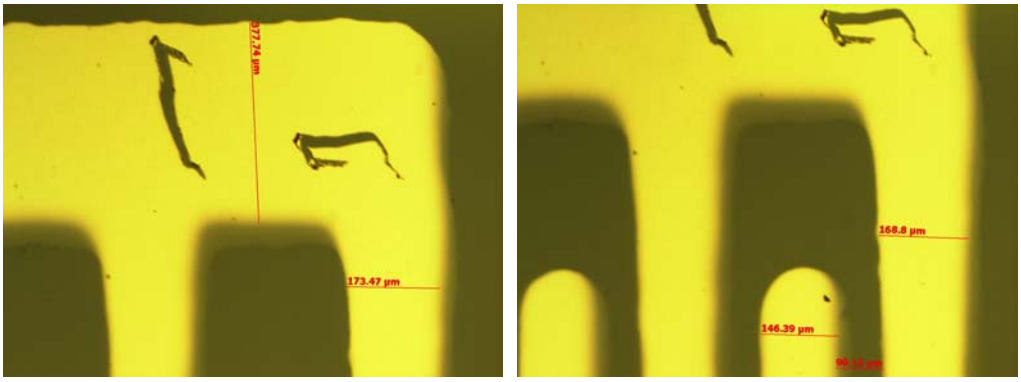

Figure 5. 23 IDT after shadow mask process.

Fig. 5.23 shows the microscopic pictures of $LiNbO_3$ substrate after shadow mask process. The IDT has finger width of about 160um and spacing of about 150um. The estimated resonant frequency of the sensor is 6.45MHz.

CNT-DMF solution is then coated on the space between the input and output IDTs and let dry, which is the same as the process mentioned in previous report. PEI-Starch solution is then coated on top of CNT and let dry. The reason of coating and letting PEI-Starch dry in air instead of immersing CNT in PEI-Starch solution for over night and let dry is because the IDT does not adhere strongly to the substrate and might peel off if immersed in PEI-Starch solution for over night.

The resulted PEI-starch coating on CNT is much thicker compared to previous report. The response amplitude and response time are expected to decrease substantially due to the thick coating on CNT. Fig. 5.24 shows the fabricated $LiNbO_3$ sensors.

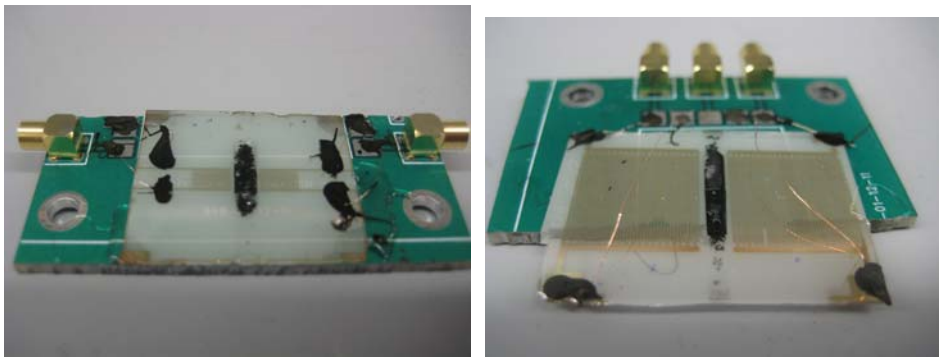

(a) (b)

Figure 5. 24 (a) $LiNbO_3$ sensor from photo lithography process. (b) $LiNbO_3$ sensor from shadow mask process.

5.5.3 SAW Sensor Performance Test Results

Similar to the measurement of thin film resistance under different gas concentration, the fabricated SAW sensor with sensitive thin film is tested in the same test chamber, with measurement equipment of network analyzer instead of resistance measurement instrument. The sensor is tested under Air (about 400ppm CO_2), and CO_2 concentrations of 0.1% (about twice of CO_2 concentration in the air), 0.5%, 1%, 5%, 10%, 20%, 35%, 50%, 75%, 90% and 100%. Normally the chamber is connected to vacuum pump for 2 minutes each time before introducing any gases into the chamber. The CO_2 concentrations of 1% and below are achieved by mixing compressed dry air and compressed dry 1% CO_2 in air. CO_2 concentrations above 1% are achieved by mixing compressed dry air and compressed dry pure CO_2.

Test results are shown in linear scale and log scale, respectively in Fig. 5.25 and Fig. 5.26.

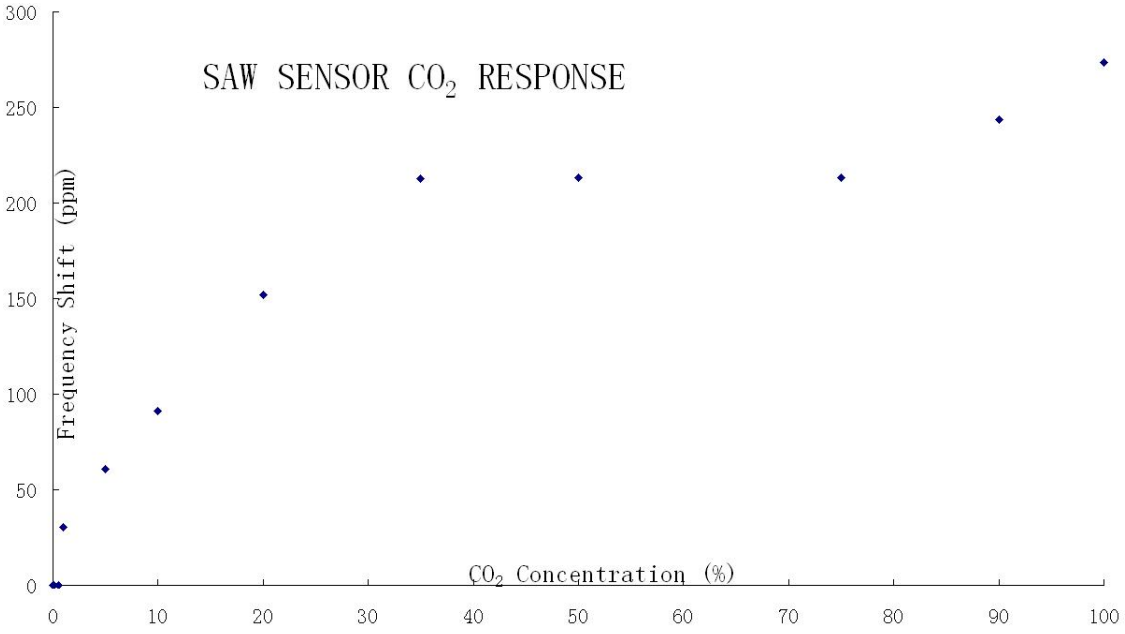

Figure 5. 25 Sensor Response in linear scale.

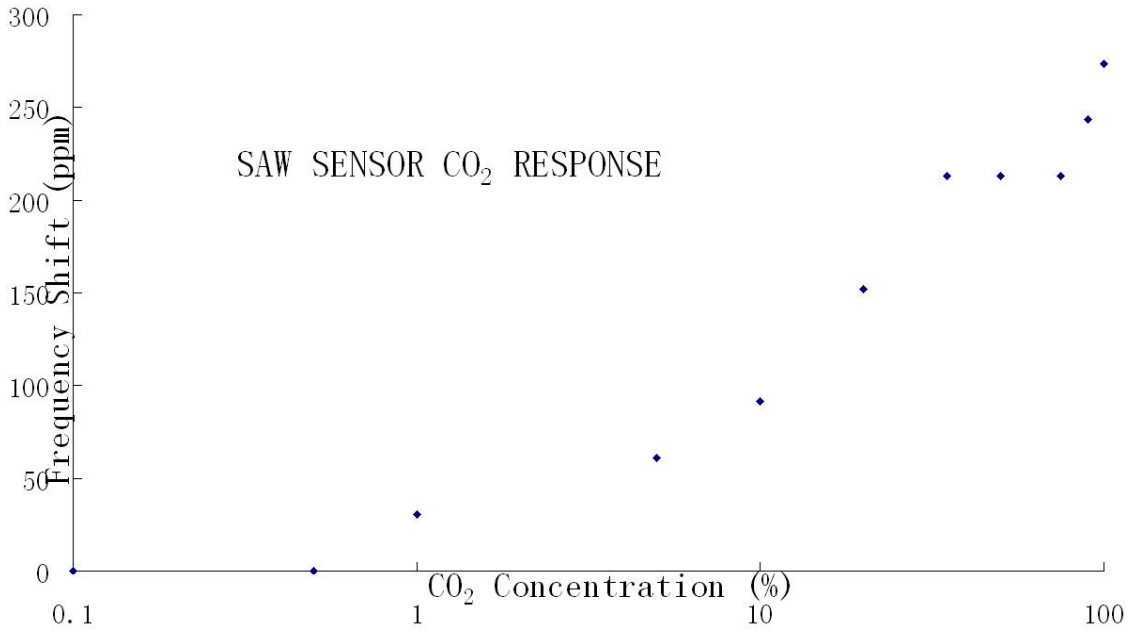

Figure 5. 26 Sensor Response in log scale.

Compare test results from Fig. 5.25 with prediction from Fig. 5.20, it can be seen that test results basically agree with prediction under 20% CO_2 concentration, while the predicted response based on resistance measurement is slightly higher than the real frequency measurement results, with over twice difference under pure CO_2. This might be caused by the slight difference in the fabrication process. In resistance measurement experiments, the test samples are immersed in starch-PEI solution for overnight and washed by DI water. While in frequency test experiments, the sensor is not immersed in the solution since the IDT might be contaminated during this process, and the starch-PEI solution is simply dropped onto the sensor and let dry or washed by DI water right away. The difference in preparation leaves the frequency test samples with less PEI-starch, thus the response to CO_2 saturates at lower concentration.

Even the sensor response to CO_2 concentration higher than 20% is not as high as predicted, the fabricated sensor still shows reasonable response, with 30ppm frequency change under 1% CO_2. Since the CO_2 concentration in the air is around 400ppm, and occasional wild fire and other natural activities might further increase this concentration, 1% is safe for not to trigger false alarm and good enough for leakage monitoring.

5.6 SAW Sensor Packaging

5.6.1 Humidity Impact on SAW Sensor Performance

Other than the huge temperature variation the sensor might be exposed to, humidity variation also

needs to be considered. The humidity, especially in the sequestration sites, might change from 35% in a sunny morning, to 100% in the stormy afternoon.

5.6.1.1 Humidity Test Setup

There are commercialized humidity testing system available with high accuracy humidity reading and multiple humidity level manipulation. Such system is perfect candidate for sensor humidity performance characterization. However the system is not readily available due to the cost. As an alternate, the sensor can be tested at several fixed humidity level. It's a common practice that in enclosed container with certain chemical solution, if the solution is over saturated at room temperature, the humidity level of the atmosphere above the solution will remain constant.

Such saturated solution provides an accurate relative humidity environment at fraction of the cost of humidity control system. As shown in Tab. 1, the relative humidity of each saturated solution depends on the temperature of the solution. Since the lab where the experiments are conducting has very stable temperature control system, the temperature fluctuation is less than 2℃. In another word, the relative humidity fluctuation is less than 1%, so the testing environment can be assumed to have constant relative humidity.

Table 5. 1 Relative Humidity of enclosed container with saturated solutions in different temperatures (from Omega).

Relative Humidity (RH%)	LiCl	$MgCl_2$	NaBr	$CaCl_2$	NaCl	KCl	K_2SO_4
20℃	11.31	33.07	59.14	32.3	75.47	85.11	97.59
25℃	11.30	32.78	57.6	31	75.29	84.34	97.30
30℃	11.28	32.44	56.0		75.09	83.62	97.00

As seen from Tab. 5.2, the solubility of each salt increases over the temperature, so the basic process of preparing the over saturated solution in room temperature is to bring the solution to elevated temperature (90℃ in our case) and dissolve all the salts. After the whole solution cools down to room temperature, the solution becomes over saturated and some of the salt crystallized out of the solution.

Table 5. 2 Solubility for different salt at different temperature.

Solubility (g/100g H_2O)	LiCl	$MgCl_2$	NaBr	$CaCl_2$	NaCl	KCl	K_2SO_4
20℃	83.5	54.6	90.8	74.5	35.89	34.2	11.1
30℃	86.2	55.8	98.4	100	36.09	37.2	13
90℃	121	69.5	121	154	38.47	53.9	22.9

It should be noted that due to the different solution heat (Enthalpy change of solution) of the salt, the dissolving process might generate a lot of heat or need certain heating environment. The

temperature change of the solution can be calculated and shown in Tab. 5.3. It can be seen that LiCl, $MgCl_2$ and $CaCl_2$ will have drastic temperature increase so their dissolving process needs to be slow and the salts need to be added to solution step by step every time after the solution temperature stabilize.

Table 5. 3 Solution heat and Temperature increase during saturated solution preparation process.

	LiCl	$MgCl_2$	NaBr	$CaCl_2$	NaCl	KCl	K_2SO_4
Solution Heat (KJ/mol)	37.4	155	0.6	81.3	-3.9	-17	-23.8
Salt Quantity (g)	460	300	330	350	150	180	72
Molecular Weight (g/mol)	42.4	95.3	102.9	111	58.5	74.6	174
Water Quantity (g)	500	500	300	300	400	400	400
Temperature Increase (℃)	193.9	233.1	1.5	204.1	-5.97	-24.5	-5.9

5.6.1.2 Humidity Test Results

The SAW sensor is then placed in the enclosed container above the saturated salt solution for testing. The measurements are conducted generally one hour after the sensor put in the container, when the signal has been stable for long time. After testing, the sensor is placed in an enclosed container with dry P_2O_5, a strong desiccant for at least 20 minutes under the signal gets stable.

Fig. 5.27 shows the sensor response under different relative humidity condition.

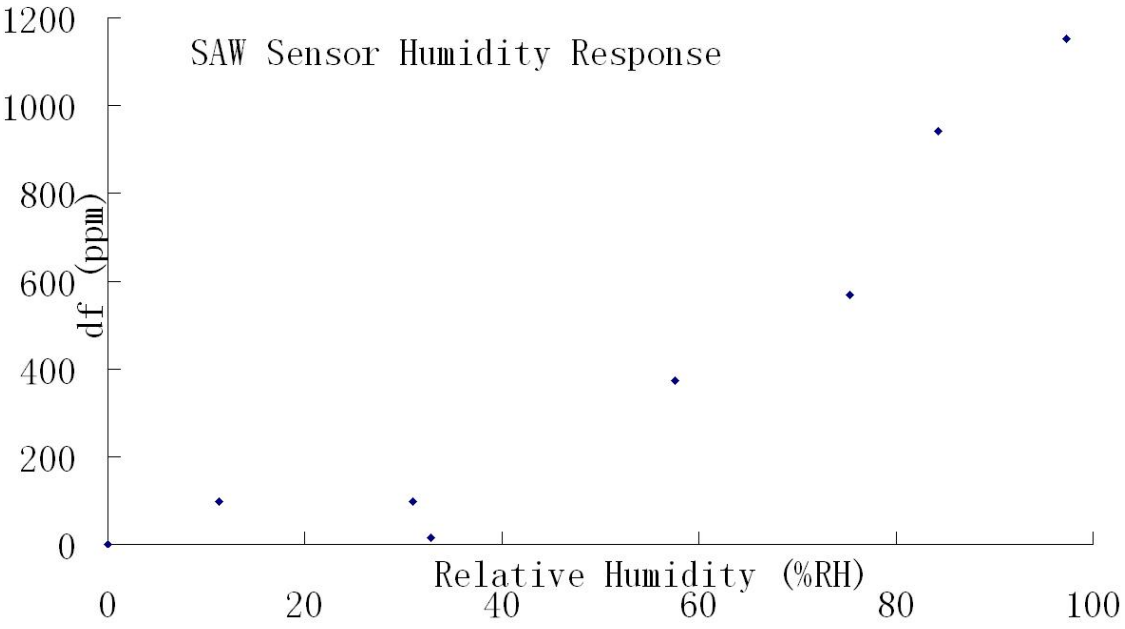

Figure 5. 27 Sensor Response to humidity.

It’s noted that under high humidity, the resonant frequency of the sensor even vanished and the response around the resonant frequency changes dramatically, as can be seen from the comparison of Fig. 5.28 to Fig. 5.35. At 84.3%RH (Fig.5.34), the measurement curve starts to deform, and the local peak at the resonant frequency completely vanishes at 97.3%RH (Fig. 5.35).

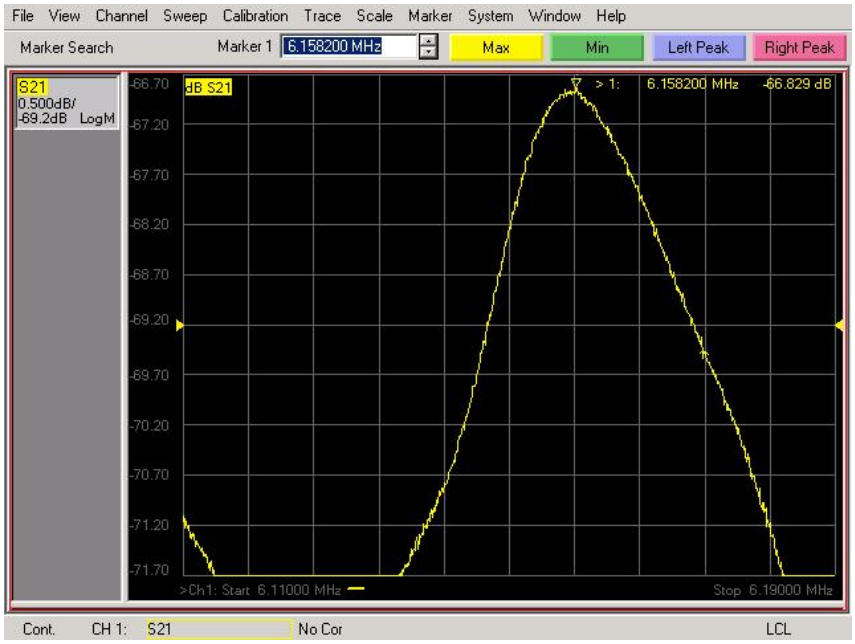

Figure 5. 28 Sensor Response at dry air with 0%RH.

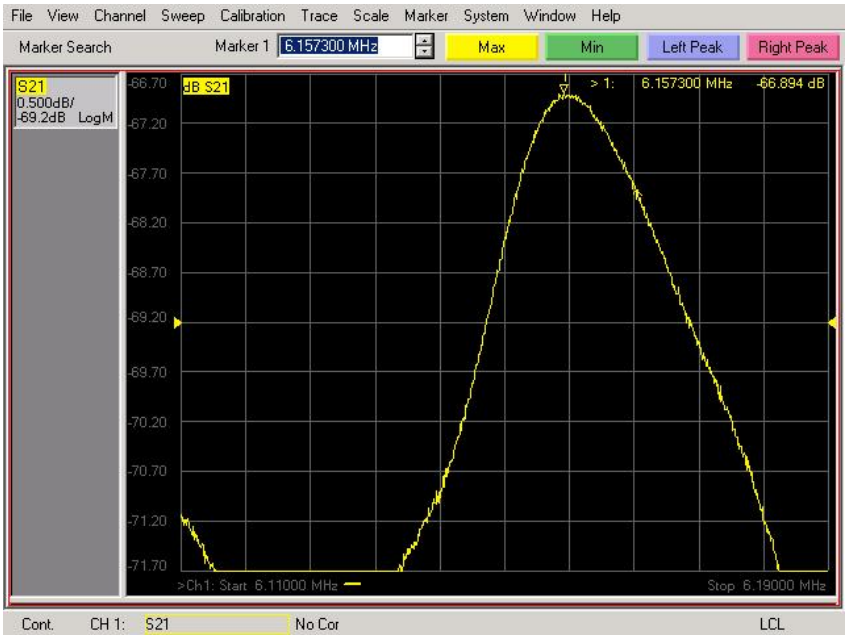

Figure 5. 29 Sensor Response 11.3%RH.

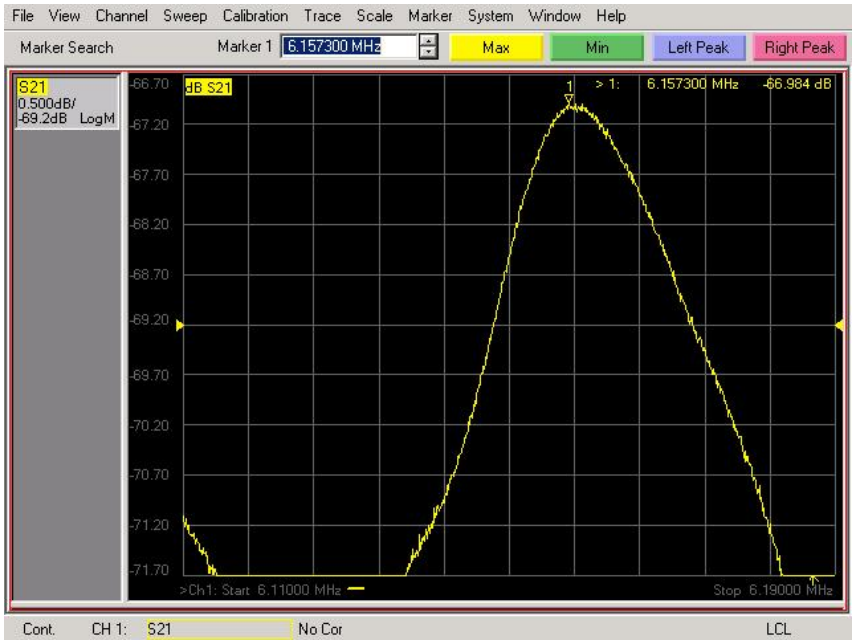

Figure 5. 30 Sensor Response 31%RH.

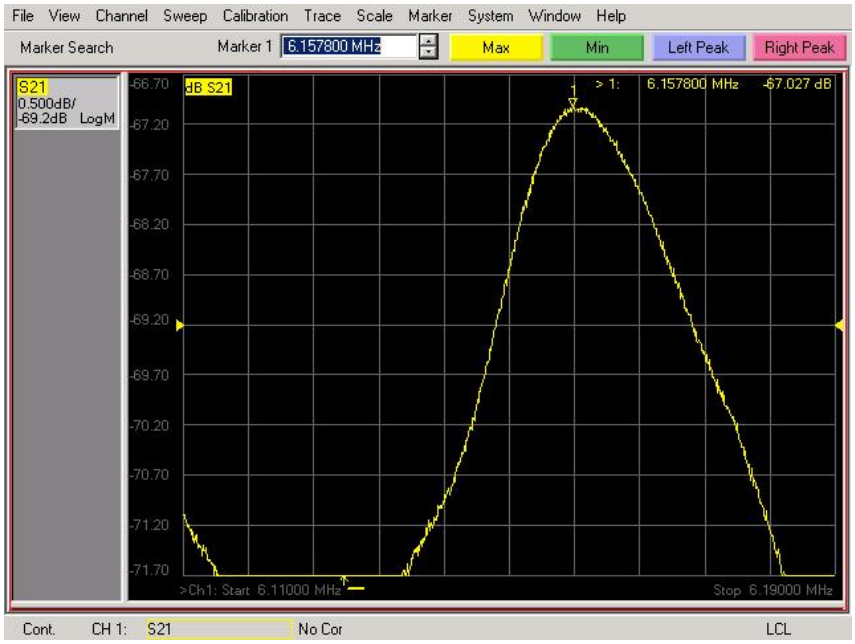

Figure 5. 31 Sensor Response 32.8%RH.

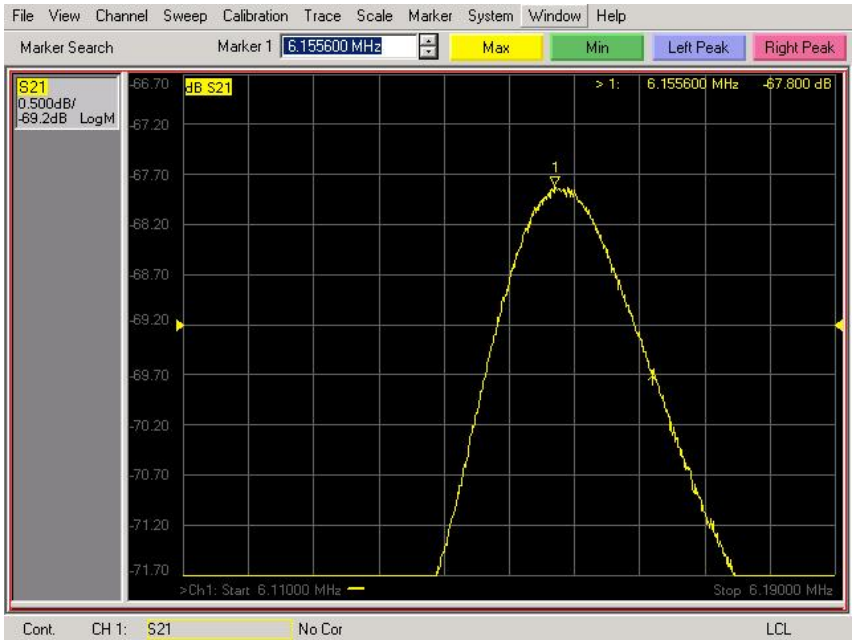

Figure 5. 32 Sensor Response 57.6%RH.

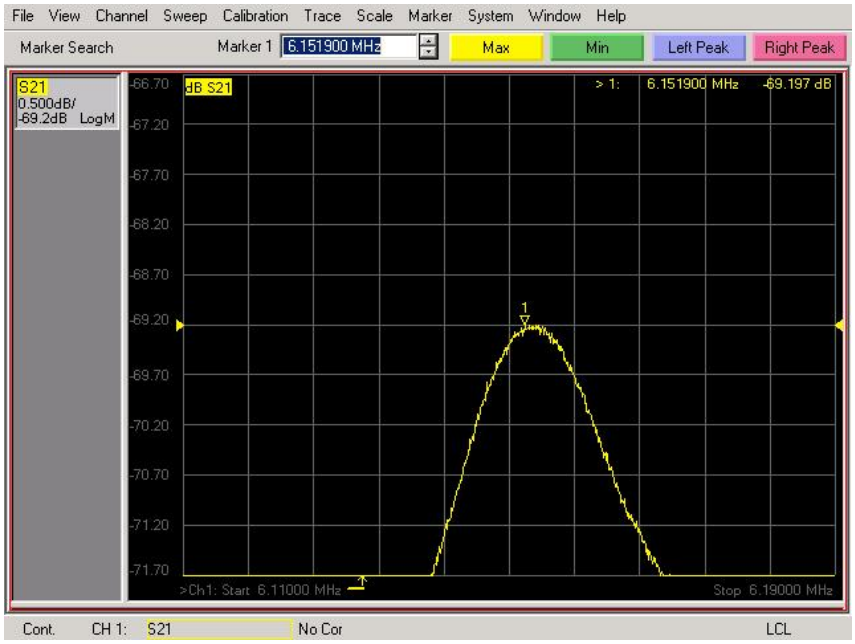

Figure 5. 33 Sensor Response 75.3%RH.

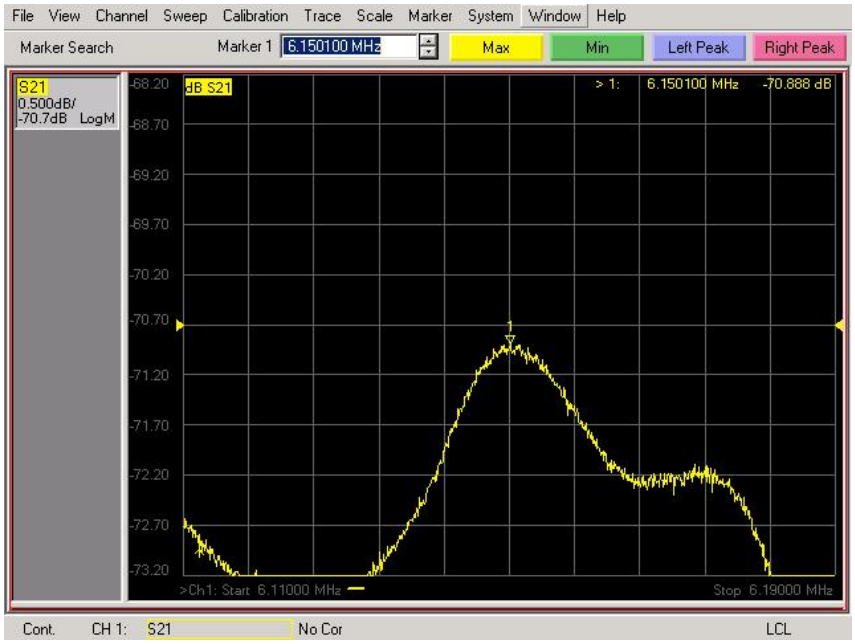

Figure 5. 34 Sensor Response 84.3%RH.

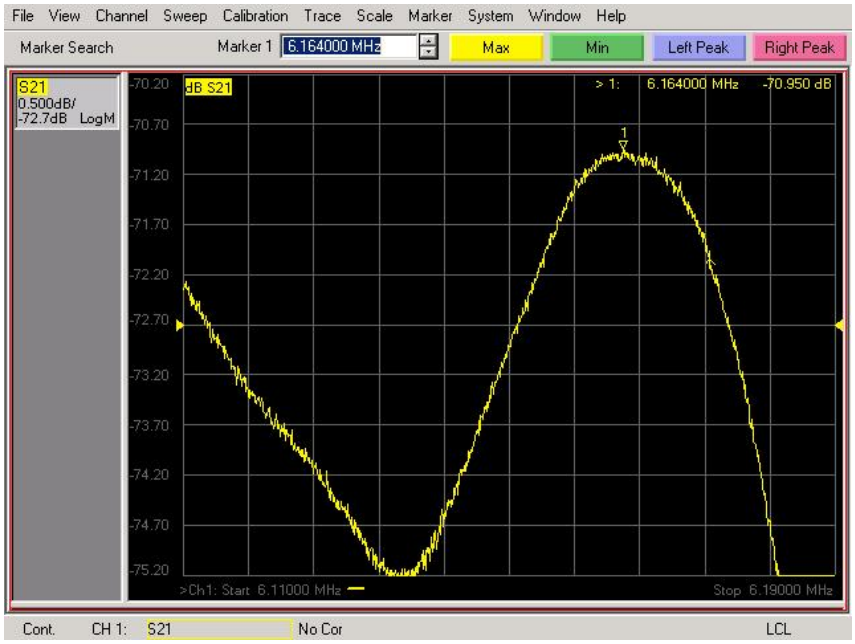

Figure 5. 35 Sensor Response 97.3%RH.

5.6.2 Parylene Packaging for SAW Sensor

Water vapor not only has impact on sensor response, but will also expedite the aging effect of the sensing material. Thus, it's necessary to build a moisture stopping layer on the sensor.

5.6.2.1 Humidity Performance for SAW Sensor Packaging

Parylene is a common used polymer served as moisture barrier. Thick parylene layer is also capable of blocking gas vapor. So parylene can be a great humidity resistance coating material for SAW sensor given the thickness is carefully selected. In our experiment, 500nm thick parylene layer is coated to build a porous hydrophobic layer that allow gas permeation while blocking water vapor. Parylene layer is coated by Specialty Coating Systems® PDS 2010. 1g parylene polymer powder is used and the resulted thin film is about 500nm thick.

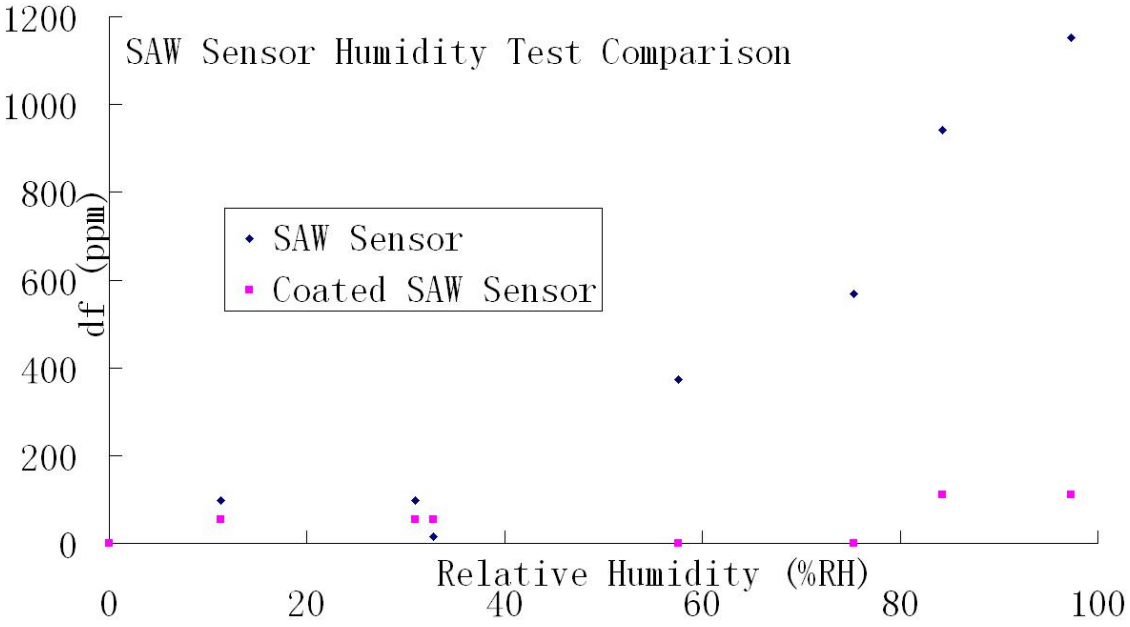

Figure 5. 36 SAW Sensor Humidity Response comparison after Parylene Coating.

As seen in Fig. 5.36, coated SAW sensor shows an order of magnitude smaller frequency shift compared with uncoated SAW sensor.

5.6.2.2 Parylene Coating Impact on SAW Sensor CO_2 Response

Although parylene at 500nm thickness is considered gas permeable, it's still necessary to test the gas response of coated SAW sensor.

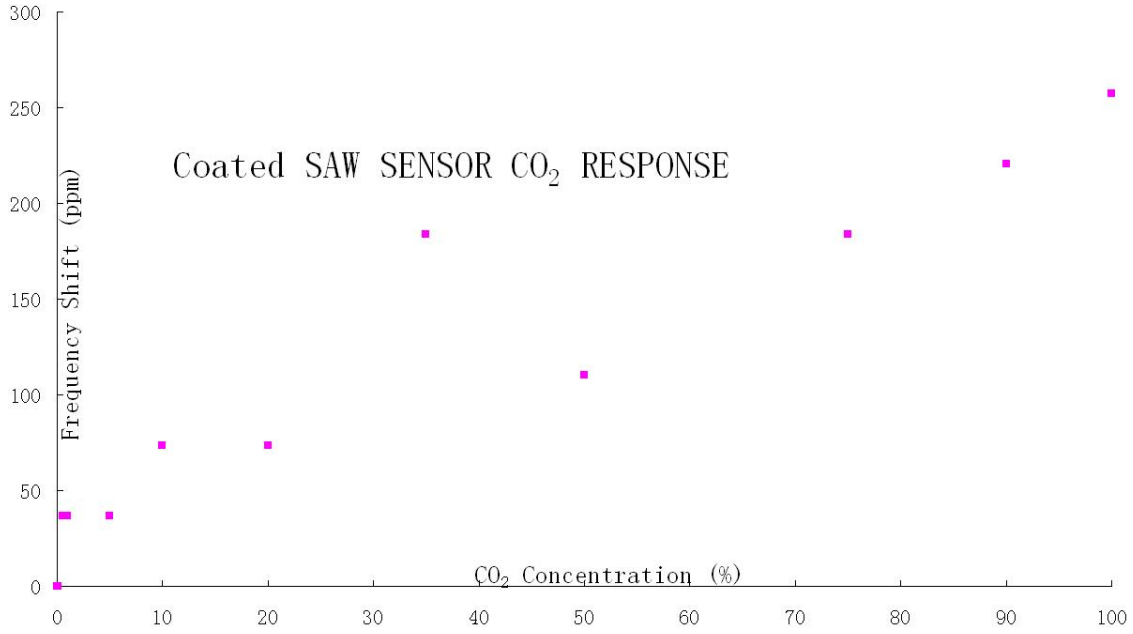

Figure 5. 37 Coated SAW Sensor gas response in linear scale.

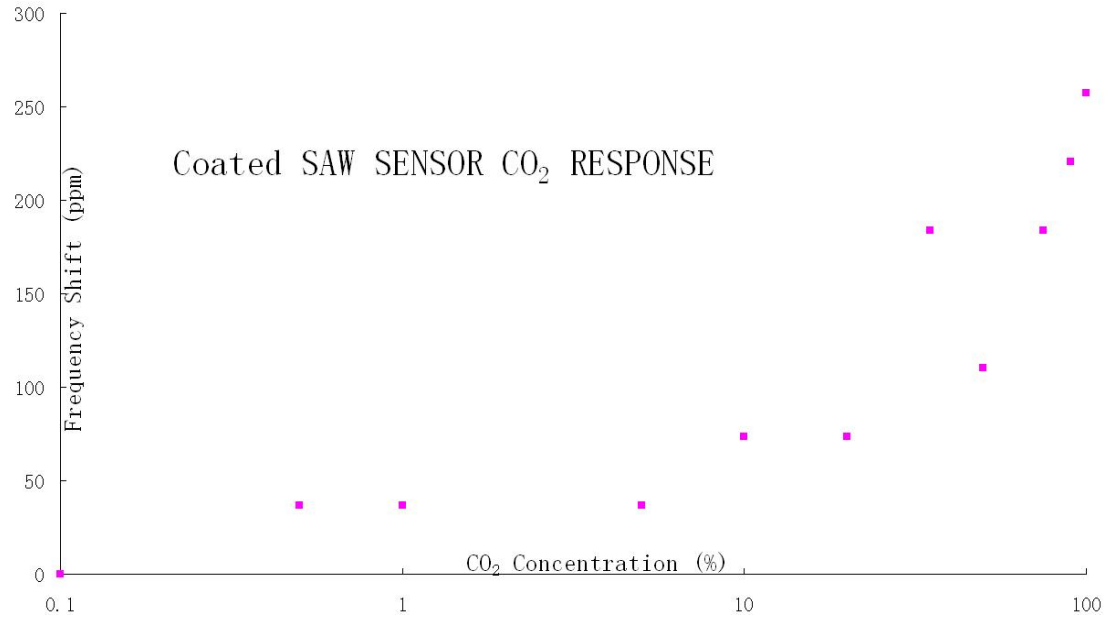

Figure 5. 38 Coated SAW Sensor gas response in log scale.

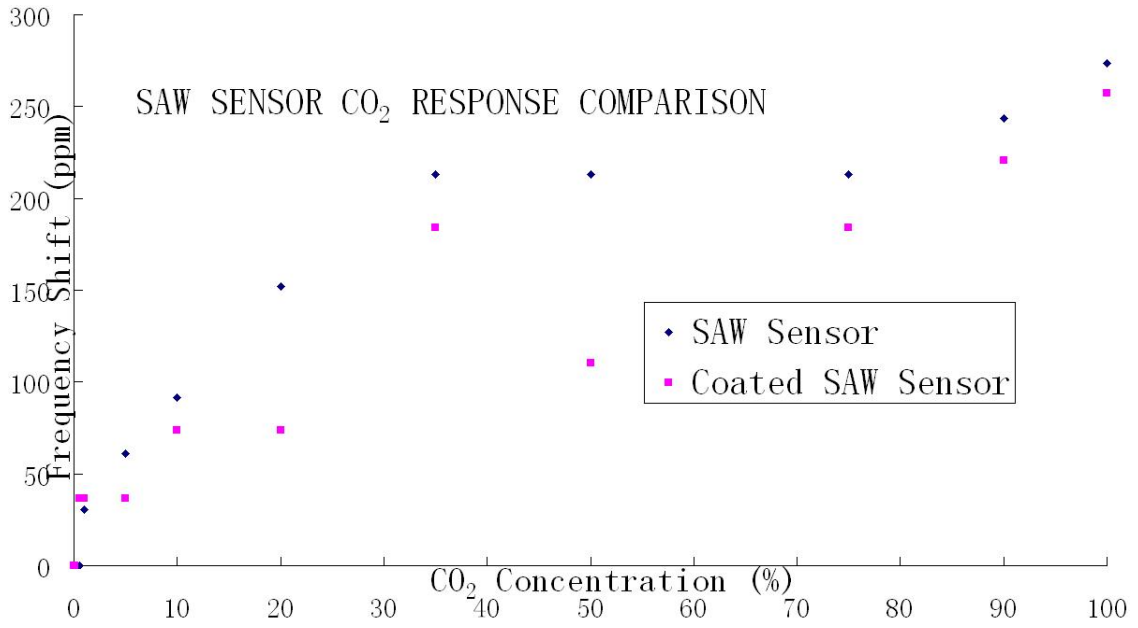

Figure 5. 39 SAW Sensor gas response comparison after coating in linear scale.

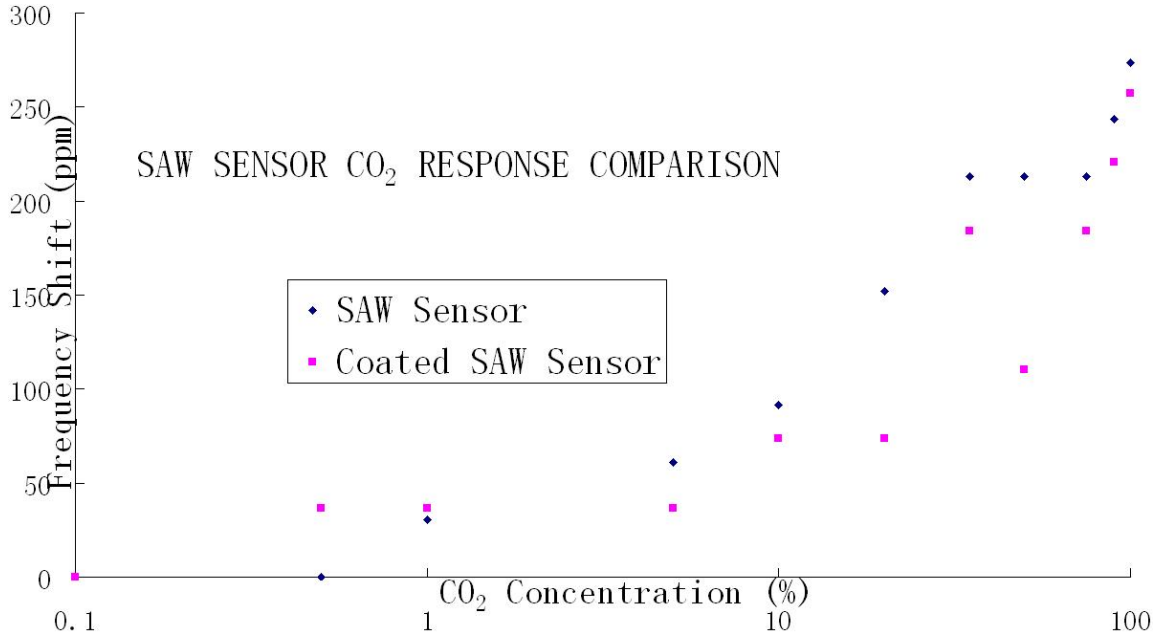

Figure 5. 40 SAW Sensor gas response comparison after coating in log scale.

Fig. 5.37 and Fig. 38 show the gas sensing response of coated SAW sensor in linear and log scale respectively. And Fig. 5.39 and Fig. 40 show the sensing performance comparison between uncoated and coated sensor in linear and log scale respectively.

It can be seen that coated sensor also respond to CO_2 concentration as low as 1% and the

frequency change at 1% is 36ppm, which is similar to the uncoated one. With the increase of CO_2 concentration, the frequency shift of coated sensor also shows similar trend while the response is generally slightly lower than that of the uncoated sensor. This proves that the coated parylene layer is gas permeable and does not hinder the sensing performance while improving the humidity resistance.

5.7 Conclusion

Gas testing system is constructed and the system is improved in turns of response time. CNT-PI thin film is tested under different gas concentrations and shows resistance change up to 0.4%, which will generate about 10ppm theoretical frequency change for pure CO_2. After reviewing the sensing mechanism of the nanocomposite, CNT-PEI-Starch structure is adopted and resistance test results show over 40 times higher response. Based on the relationship between thin film conductivity and frequency shift, the sensor is estimated to have frequency shift of over 1000ppm for pure CO_2. The test of SAW sensor with CNT-PEI-Starch sensing film shows comparable results, with similar response at concentration lower than 20% and 300ppm frequency change for pure CO_2. The sensor shows a detection limit of 1%, which is satisfying considering the situation in sequestration sites. Humidity factor is also considered in sensor performance evaluation. The SAW sensor undergoes 3 times greater frequency change when humidity changes than when only gas concentration changes. Parylene packaging is introduced and the humidity response is reduced to around 100ppm at 100%RH. In the mean time, the packaging shows minimum impact on gas sensing.

6.0 WIRELESS SENSING MODULE DESIGN AND CHARACTERIZATION

After the SAW sensor is successfully built with sensing limit of 1% CO_2 concentration and is prone to humidity change, it's necessary to integrate the sensor with wireless module so the sensing system can be used in real field application.

6.1 Introduction

As for wireless integration, the key component is a suitable antenna for SAW sensor with appropriate bandwidth and gain. Radio frequency microelectromechanical system (RF MEMS), electronic components of which moving sub-millimeter-sized parts provide RF functionality, have long been developed and studied [81]. RF functionality can be implemented using a variety of RF technologies. Besides RF MEMS technology, III-V compound semiconductor (GaAs, GaN, InP, InSb), ferrite, ferroelectric, silicon-based semiconductor (RF CMOS, SiC and SiGe), and vacuum tube technology are available to the RF designer. Each of the RF technologies offers a distinct trade-off between cost, frequency, gain, large-scale integration, lifetime, linearity, noise figure, packaging, power handling, power consumption, reliability, ruggedness, size, supply voltage, switching time and weight.

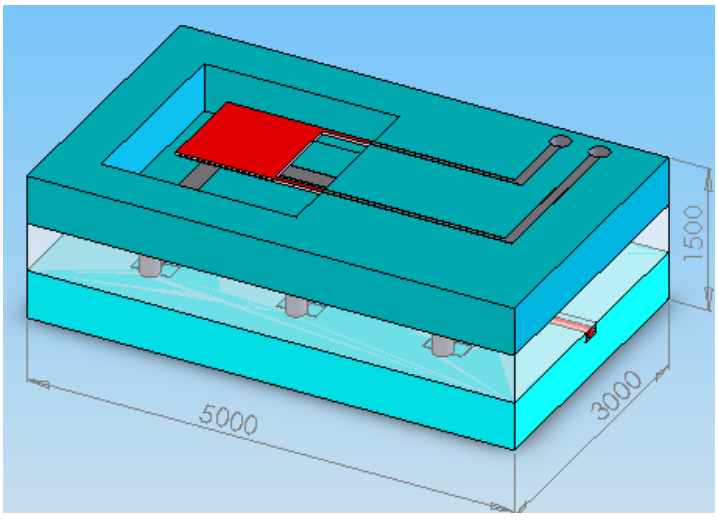

Figure 6. 1 Typical onchip antenna with simplified structure

Fig. 6.1 shows a typical antenna with simplified structure [82]. Fig. 6.2 and Fig. 6.3 shows two other on chip antennas with more turns in structure [83-84].

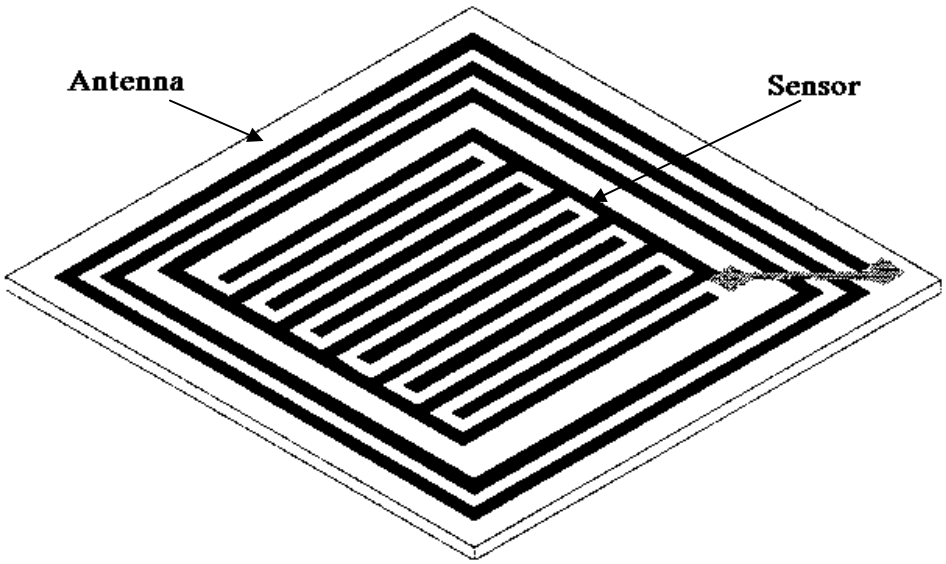

Figure 6. 2 Integrated Antenna surrounding the sensor.

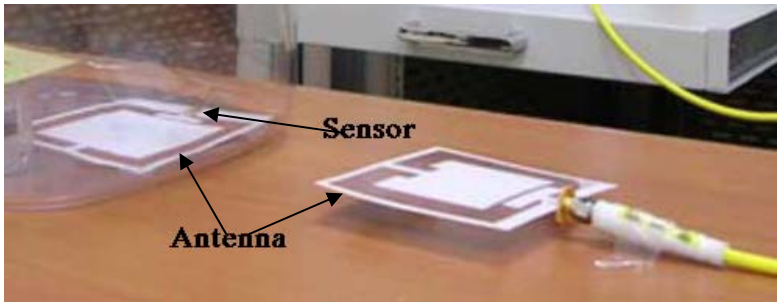

Figure 6. 3 On chip Antenna outside of the sensor.

As shown in Fig.6.1, one intuitive design is two-layer structure for wireless module implementation. The antenna module is right on top of the sensor module. Such structure is relatively complicated per fabrication wise and needs fine tuning before real application.

Considering manufacturing difficulty and antenna performance, the antenna structure similar to Fig. 6.3 will be adopted since separated antenna can offer manufacturing flexibility and reduce cost significantly.

The antenna can work with one turn only depending on the resonant frequency and gain requirement. Planar antenna is generally Omni directional or only weakly directional, which means the antenna can intercept radio signal from all directions.

MEMS type antenna normally works at high frequency since the resonant frequency of the LC

circuit can be calculated as $f_{resonant} = \frac{1}{2\pi\sqrt{LC}}$. So for lower resonant frequency, either the capacitance or the inductance of the circuit needs to be sufficiently large. Thus planar antenna is not recommended for system with resonant frequency lower than 400MHz.

6.2 Antenna Design

Due to fabrication limit, the maximum resonant frequency in our sensor design is below 100MHz, which means planar antenna is not the best choice so we turned to small scale macro size antenna.

The inductor we used in the project is 132-20SM_LB from Coilcraft®. The inductor has 20 turns of coils with 538nH conductance. And the coil can be connected to a capacitor in parallel to be used as resonant circuit. Two coil can be connected in series to double the inductance. Based on $f_{resonant} = \frac{1}{2\pi\sqrt{LC}}$, the required capacitance for the wireless module can be calculated accordingly.

For gas sensor with IDT from shadow mask, the design frequency is 6.45MHz. And the real measurement of one prepared sensor gives a resonant frequency between 6.114MHz and 6.116MHz, depending on the gas concentration. It can be calculated that for the design frequency, the desired capacitance is 1131.7uF. For the specific sensor, the desired capacitance is between 1258.7uF and 1259.5uF. For sensors with IDT from photolithography process, the design frequency is 66.7MHz, while the measured resonant frequency is 60.6MHz. The corresponding capacitance in the system is therefore 10.6uF and 12.8uF.

Due to the nature of the fabrication process, the fabricated IDT electrodes will have certain error for each batch of sensors. So the resonant frequency will have slight change between the sensors, which require tunable LC circuit, in this case, tunable capacitor.

The capacitor is from McMaster®. The size for 540-648uF capacitor is 2.75”H×1.44”D, and the size for 30-36uF capacitor is the same.

The transmission losses of the sensors vary between 30dB and 40dB. Since the network analyzer currently used in this project can measure signal that has transmission loss up to 90dB. So the total transmission loss caused by wireless module needs to be limited to about 60dB.

6.3 Antenna Construction

Fig. 6.4 shows a sample sensor with resonant frequency of 6.136328MHz and the insertion loss at resonant frequency of 39.974dB.

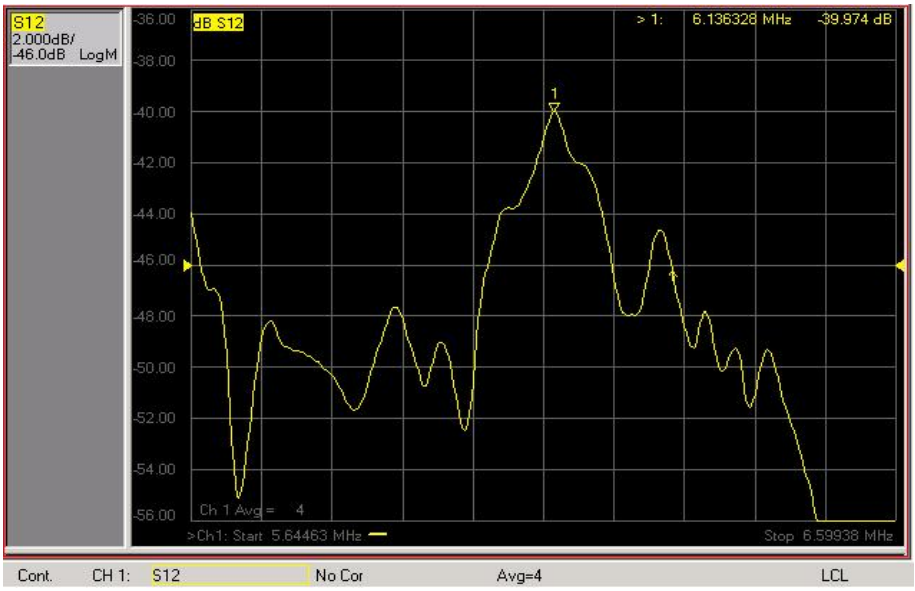

Figure 6. 4 Basic Sensor response of the sample sensor with wireless module (wireless module not connected).

A wireless module is constructed with a pair of antennas. The antenna used here is consisted of a capacitor in parallel connection with a double-coil, which is made of two coils in series connection. The purpose of the double-coil is to increase the overall inductance and thus reduce the capacitance required. The double coil used here has an inductance of 1076nH. So the capacitance used here is a tunable capacitor with range between 480pF and 650pF. The wireless module is then connected between the wireless port and the SAW sensor, as shown in Fig. 6.5.

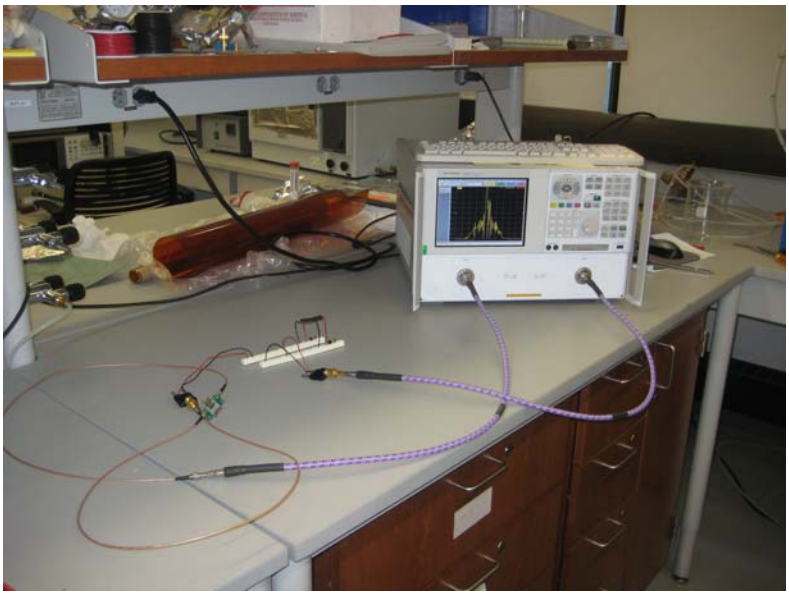

Figure 6. 5 Sample sensor connected with wireless module under measurement.

Fig. 6.6 shows the close look-up of the antenna.

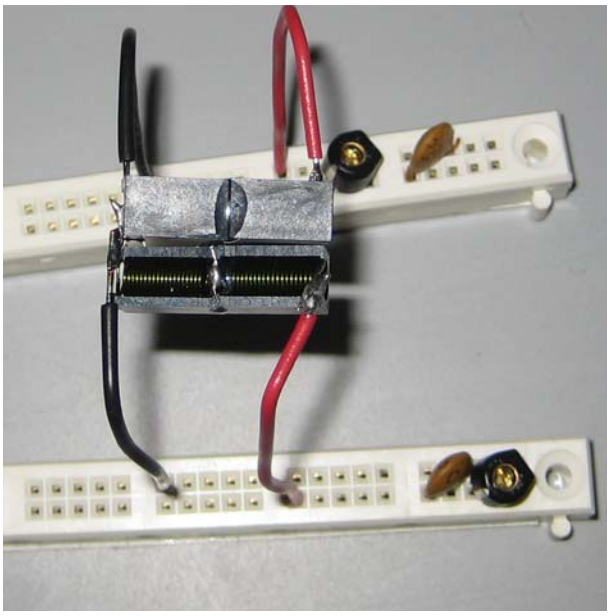

Figure 6. 6 Antenna consisting a double-coil and capacitor.

6.4 Antenna Characterization

As shown in Fig. 6.7, the wireless antenna is tested under two circumstances, series and parallel.

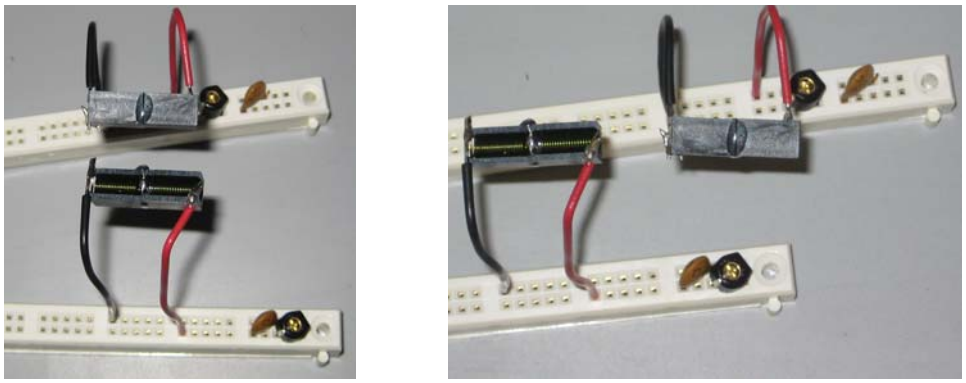

(A) (B)

Figure 6. 7 Antenna testing circumstances. (A) in series. (B) in parallel.

Fig. 6.8 to Fig. 6.11 shows the wireless sensor response at different distances in series configuration. Fig. 6.12 to Fig. 6.22 shows the wireless sensor response at different distances in parallel configuration.

Figure 6. 8 Sensor response with antenna in series configuration at 0mm distance.

Figure 6. 9 Sensor response with antenna in series configuration at 5mm distance.

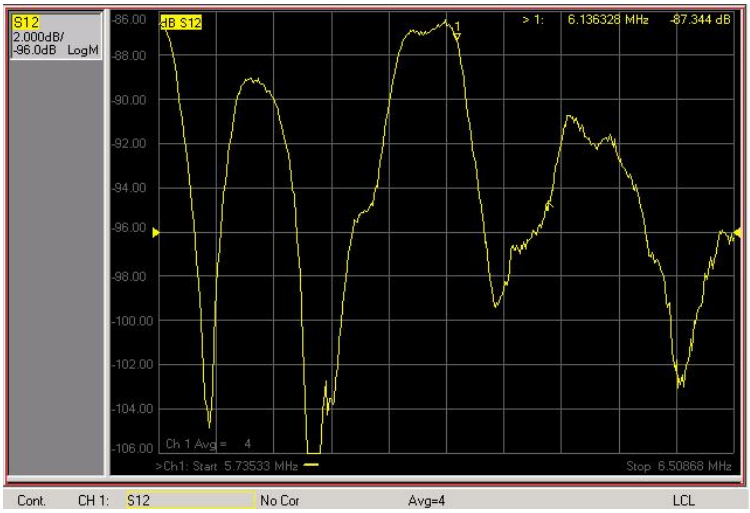

Figure 6. 10 Sensor response with antenna in series configuration at 10mm distance.

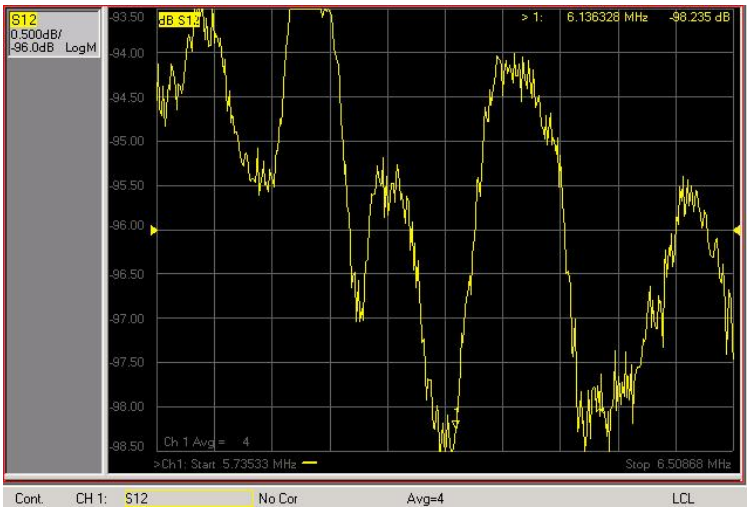

Figure 6. 11 Sensor response with antenna in series configuration at 15mm distance.

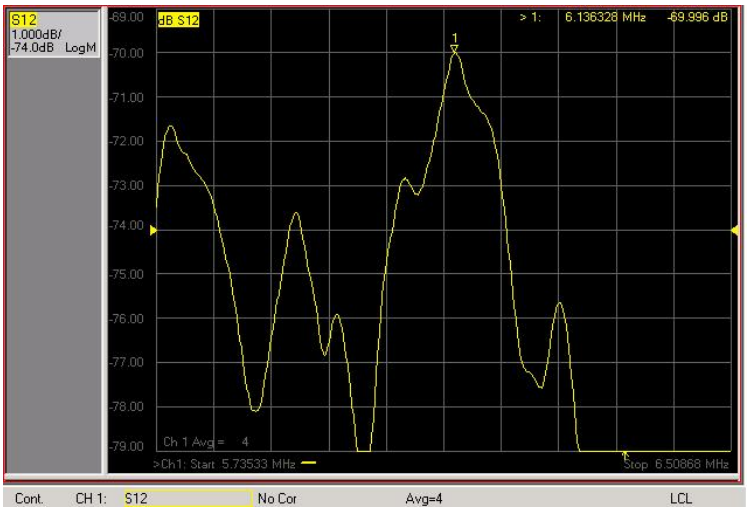

Figure 6. 12 Sensor response with antenna in parallel configuration at 0mm distance.

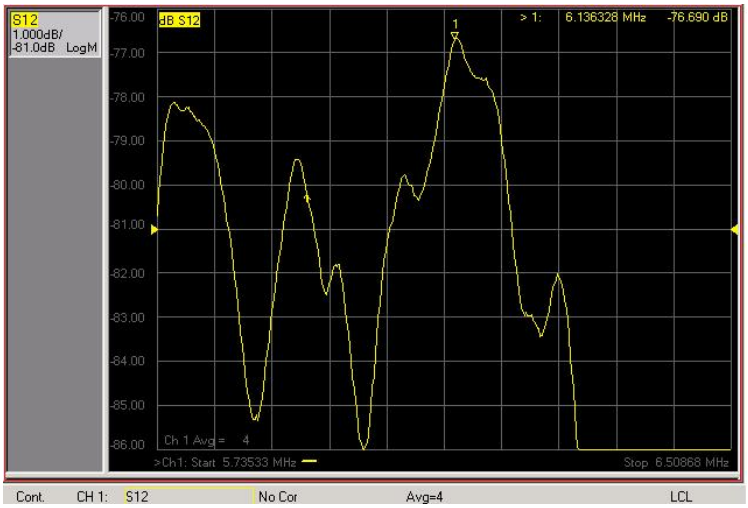

Figure 6. 13 Sensor response with antenna in parallel configuration at 5mm distance.

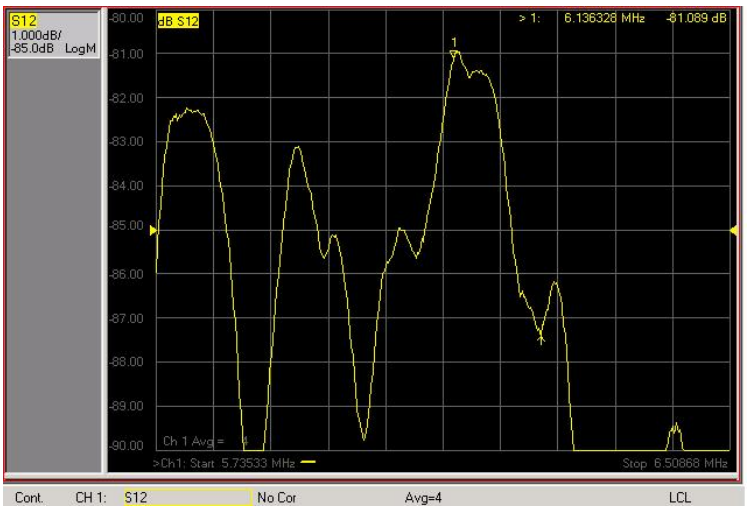

Figure 6. 14 Sensor response with antenna in parallel configuration at 10mm distance.

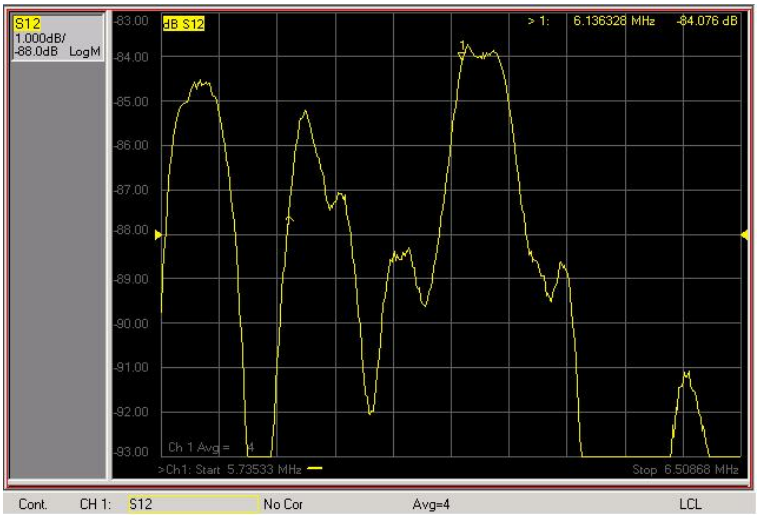

Figure 6. 15 Sensor response with antenna in parallel configuration at 15mm distance.

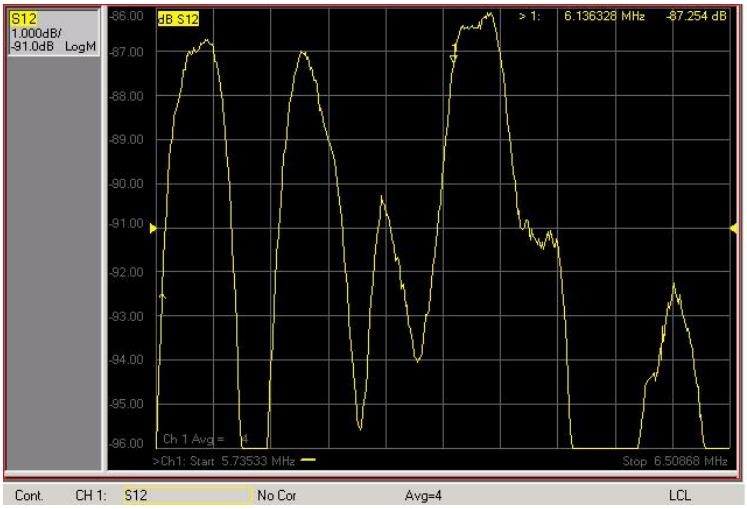

Figure 6. 16 Sensor response with antenna in parallel configuration at 20mm distance.

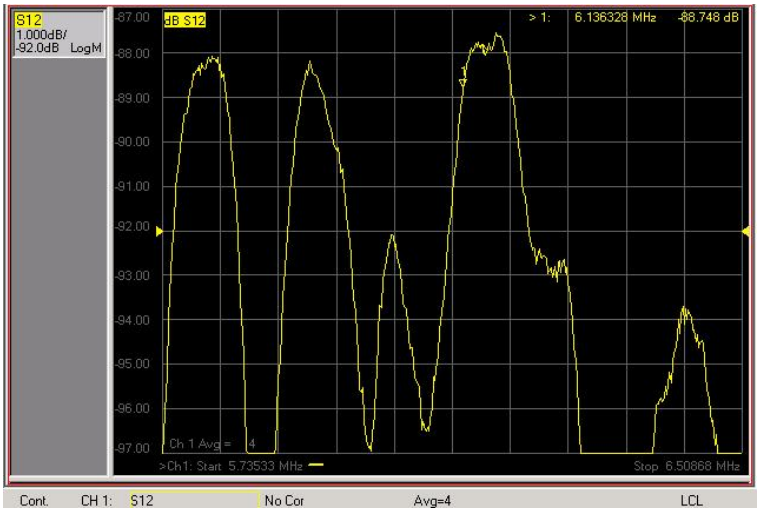

Figure 6. 17 Sensor response with antenna in parallel configuration at 25mm distance.

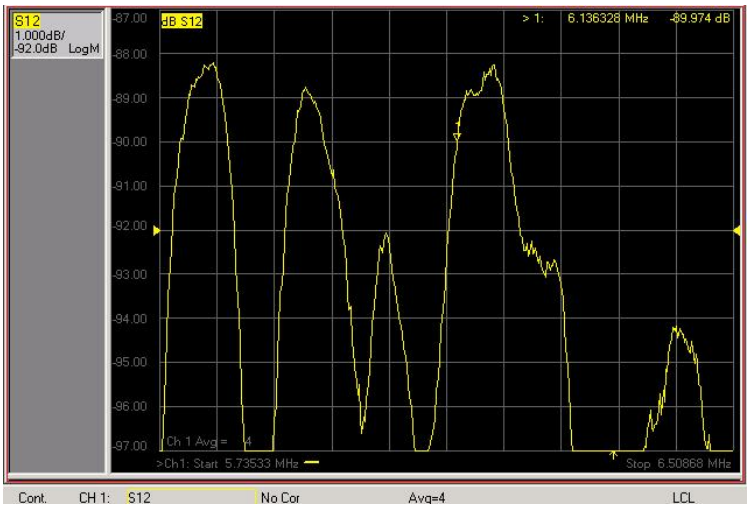

Figure 6. 18 Sensor response with antenna in parallel configuration at 30mm distance.

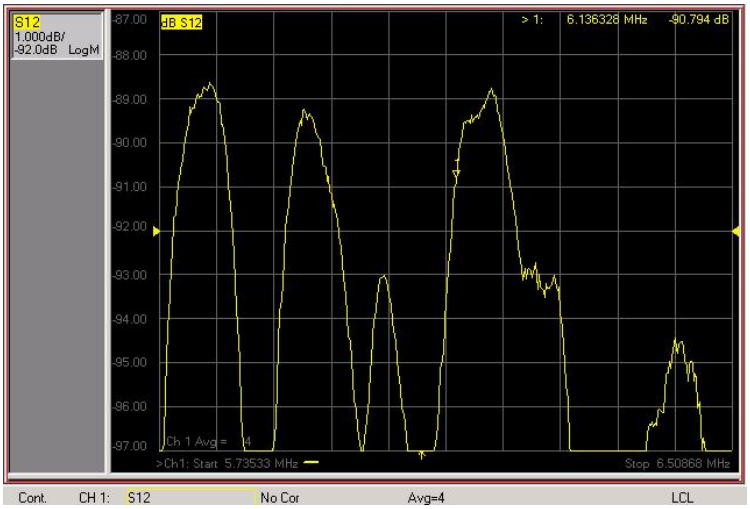

Figure 6. 19 Sensor response with antenna in parallel configuration at 35mm distance.

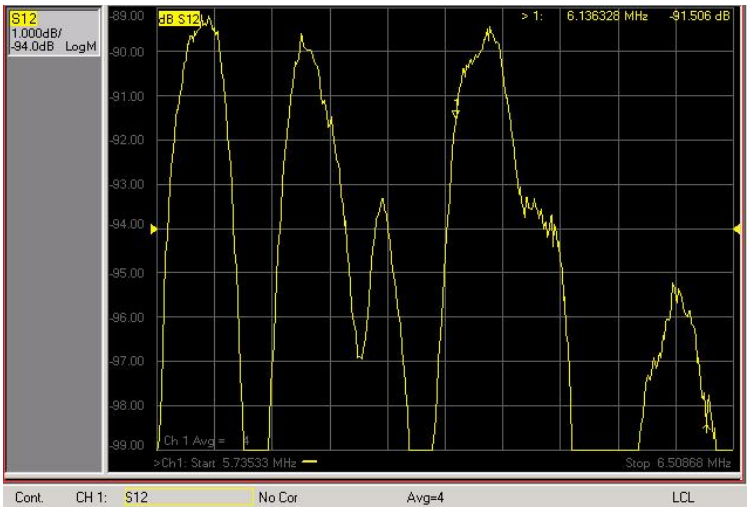

Figure 6. 20 Sensor response with antenna in parallel configuration at 40mm distance.

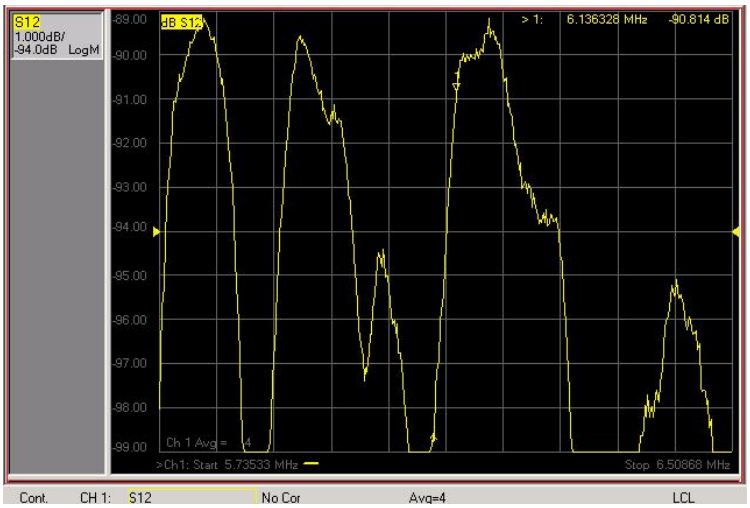

Figure 6. 21 Sensor response with antenna in parallel configuration at 45mm distance.

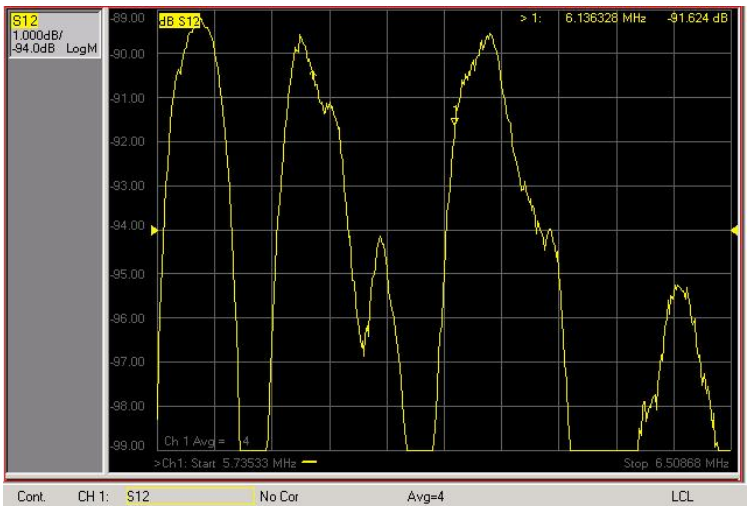

Figure 6. 22 Sensor response with antenna in parallel configuration at 50mm distance.

It can be seen from the sensor response curve that when the insertion loss is greater than 90dB, the resonant frequency shifts a lot and noise increases significantly. This is caused by the detection limit of the network analyzer. The change of insertion loss versus the distance between the antennas can be seen from Fig. 6.23.

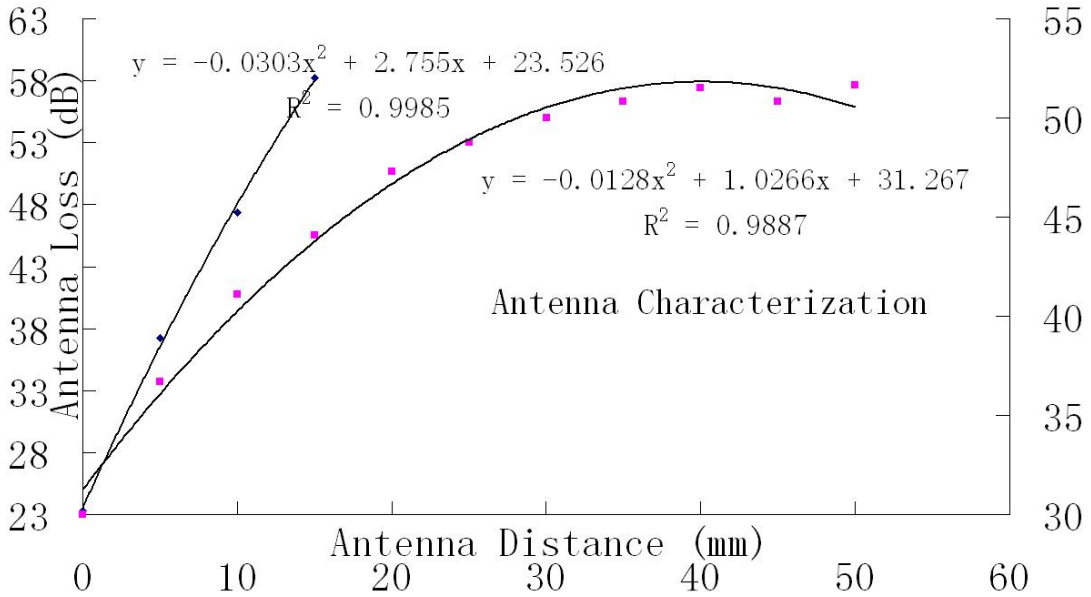

Figure 6. 23 Antenna performance summary.

It can be seen from Fig. 6.23 that the parallel configuration has lower antenna loss compared to the series configuration. It can also be seen that for a sensor with 23.633dB insertion loss, as mentioned in previous report, the maximum loss the antenna can have is about 68dB. In another word, that means the antenna range can be over one foot if properly oriented.

6.5 Conclusion

Due to fabrication limits, the SAW sensor operates at frequency well below 400MHz, thus ruling out the on-chip antenna and planar antenna. An antenna with tunable capacitor and coil is constructed and tested. Test results show that under parallel oriented condition, the antenna has working distance above one foot.

There are many ways to improve the antenna range, including adding separate power amplifier for antenna, increasing operating frequency, etc.

7.0 Conclusions

The overall goal of the proposed project was to fabricate SAW sensor with wireless component, use CNT nanocomposite as sensing element, meanwhile, and explore the application of SAW sensor and CNT nanocomposites for multifunctional applications. Toward that end, the following specific project objectives were set for work that was performed in response to the above goal:

Objective: Fabricate the SAW sensor and characterize the impact of different parameters on SAW performance
Achievement: SAW characteristic are studied during the construction of SAW flow sensor. The impact of the piezoelectric material properties on sensor performance, the effect of strain on sensor performance were all assessed. The results show linear relationship between the SAW delay time and flow rate, as predicted by simulation and theoretical calculation.

Objective: Fabricate the CNT nanocomposite and characterize the impact of different parameters on nanocomposite response
Achievement: The percolation threshold was studied. PI was first chosen in nanocomposite fabrication because of its resistance to harsh environment, especially high temperature, thus extending the sensor application range. Due to the nature of nanocomposite, the thin film is very sensitive to temperature change. Temperature test shows that the nanocomposite has temperature coefficient of about -1375ppm/℃. It's noted that due to the difference of thermal expansion coefficients in nanocomposite and SAW substrate, the temperature change will also induce thermal strain. Strain test of the nanocomposite suggests that thermal strain will change the resistance by 375ppm/℃. So the overall effect of temperature on the nanocomposite is -1000ppm/℃.

Objective: Evaluate the CNT nanocomposite gas response and characterize SAW sensor gas response
Achievement: The gas test proves that PI is not an ideal candidate for nanocomposite fabrication. The resistance change under pure CO_2 is only 0.4%. Based on SAW sensor characteristic, the expected frequency change would be about 10ppm for pure gas. Tracing the chemistry under the sensing mechanism provides a better choice with functional groups that are more active. PEI-Starch is then selected based on the chemical principle and the resulted nanocomposite gives a substantial resistance change of about 10% for pure gas. The estimated frequency change of the SAW sensor is promoted to around 1000ppm, about 100 times higher than the nanocomposite with PI. After the integration of SAW sensor and the sensing film, the measurement results come back as 300ppm frequency change for pure gas. Though lower than expected, the sensor performance is almost the same for gas concentration under 20% and the detection limit is about 1% gas concentration. Due to the complicated weather condition of the sequestration sites, the impact of humidity on the sensor is brought into consideration. Humidity test shows over

1000ppm frequency change for saturated water vapor, which is way greater than the gas response. Parylene is hence chosen as the sensor packaging material. Humidity test results for the SAW sensor with packaging shows less than 100ppm frequency for saturated water vapor while the gas response remains about 300ppm for pure CO_2. The parylene proves to greatly enhance the resistance to humidity while preserving the gas sensitivity and the detection limit.

Objective: Develop a novel CNT nanocomposite SAW sensor with wireless function
Achievement: Different wireless modules are studied and separated antenna is chosen based on cost effective standpoint. Due to fabrication limit of the sensor, the planar antenna is excluded and tunable capacitor with coil structure is chosen instead. Test results show large difference between parallel and series orientation of the coil, thus suggesting the existence of an optimum coil orientation. With current configuration, the wireless module is expected to work at over one foot distance. The working range, however, can be increased by many methods.

Overall, SAW gas sensor with wireless module is developed. Each component in the sensing system is investigated and improved for maximum performance. The system performance is in reasonable range and can be used for CO_2 geological sequestration sites monitoring.

8.0 REFERENCES

[1] America's Climate Choices. Washington, D.C.: The National Academies Press. 2011. p. 15. ISBN 978-0-309-14585-5.
[2] http://en.wikipedia.org/wiki/Global_warming
[3] EPA (2007). "Recent Climate Change: Atmosphere Changes". Climate Change Science Program. United States Environmental Protection Agency.
[4] http://en.wikipedia.org/wiki/Nondispersive_infrared_sensor
[5] http://en.wikipedia.org/wiki/Carbon_dioxide_sensor
[6] S. Neethirajan, D. S. Jayas and S. Sadistap. Carbon Dioxide (CO2) Sensors for the Agri-food Industry—A Review. Food and Bioprocess Technology. Volume 2, Number 2, pp.115-121.
[7] Cattrall, R. W. (1997). Chemical sensors. Oxford, UK: Oxford University Press.
[8] http://www.epa.gov/climatechange/emissions/co2_human.html
[9] http://en.wikipedia.org/wiki/Carbon_capture_and_storage
[10] http://www.slb.com/services/additional/carbon/projects.aspx#
[11] http://en.wikipedia.org/wiki/Carbon_dioxide_sensor
[12] Eiji Ohtaki and Tetsuji Matsui. Infrared device for simultaneous measurement of fluctuations of atmospheric carbon dioxide and water vapor. Boundary-Layer Meteorology.Volume 24, Number 1, pp.109-119.1982.
[13] http://www.habmigern2003.info/future_trends/infrared_analyser/ndir/ndir.htm
[14] R. Zhou, S. Vaihinger, K.E. Geckeler and W. Göpel. Reliable CO_2 Sensors Based with Silicon-based Polymers on Quartz Microbalance Transducers. Conf. Proc. Eurosensors VII, Budapest (H) (1993); Sensors and Actuators B, 18-19, 1994, 415-420.
[15] H.-E. Endres, R. Hartinger, M. Schwaiger, G. Gmelch, and M. Roth. A capacitive CO_2 sensor system with suppression of the humidity interference. Sensors Actuators B, vol. 57, pp. 83–87, 1999.
[16] M. S. Lee and J. U. Meyer. A new process for fabricating CO_2 sensing layers based on $BaTiO_3$ and additives. Sensors Actuators B, vol. 68, pp.293–299, 2000.
[17] S. Matsubara, S. Kaneko, S. Morimoto, S. Shimizu, T. Ishihara, and Y. Takita. A practical capacitive type CO_2 sensor using CeO_2/$BaCO_3$/CuO ceramics. Sensors Actuators B, vol. 65, pp. 128–132, 2000.
[18] J. F. Currie, A. Essalik, and J. C. Marusic. Micro machined thin film solid state electrochemical CO_2, NO_2, and SO_2 gas sensors. Sensors Actuators B, vol. 59, pp. 235–241, 1999.
[19] Lord Rayleigh. On Waves Propagated along the Plane Surface of an Elastic Solid. Proc. London Math. Soc. s1-17 (1): 4–11, 1885.
[20] http://en.wikipedia.org/wiki/Surface_acoustic_wave
[21] http://en.wikipedia.org/wiki/Carbon_nanotube
[22] Yun Wang and John T. W. Yeow. A Review of Carbon Nanotubes-Based Gas Sensors. Journal of Sensors. Volume 2009, pp.1-24, 2009.
[23] Hongbin Cheng, Jiping Cheng, Yunjin Zhang, and Qing-Ming Wang. Large-scale Fabrication

of ZnO Micro-and Nano-Structures by Microwave Thermal Evaporation-Deposition. Journal of Crystal Growth, Volume 299, Issue 1, 1 Feb. 2007, pp. 34-40.
[24] C. Sanchez, B. Julian, P. Belleville, and M. Popall. Applications of hybrid organic–inorganic nanocomposites. J. Mater. Chem., 2005.15: p.3559
[25] ShahD. Shah, P. Maiti, E. Gunn, D. F. Schmidt, D. D. Jiang, C. A. Batt, E. P. Giannelis. Dramatic Enhancements in Toughness of Polyvinylidene Fluoride Nanocomposites via Nanoclay-Directed Crystal Structure and Morphology. AdV. Mater., 2004. 16: p.1173.
[26] S. Manna, S. K. Batabyal, A. K. Nandi. Preparation and Characterization of Silver-Poly(vinylidene fluoride) Nanocomposites: Formation of Piezoelectric Polymorph of Poly(vinylidene fluoride). J. Phys. Chem. B, 2006.110: p. 12318.
[27] M. Moniruzzaman, K. I. Winey. Polymer Nanocomposites Containing Carbon Nanotubes. Macromolecules, 2006.39: p.5194.
[28] Q. Chen, Y. Bin, M. Matsuo. Characteristics of Ethylene-Methyl Methacrylate Copolymer and Ultrahigh Molecular Weight Polyethylene Composite Filled with Multiwall Carbon Nanotubes Prepared by Gelation/Crystallization from Solutions. Macromolecules, 2006.39: p.6528.
[29] B. K. Kuila, S. Malik, S. K. Batabyal, A. K. Nandi. In-Situ Synthesis of Soluble Poly(3-hexylthiophene)/Multiwalled Carbon Nanotube Composite: Morphology, Structure, and Conductivity. Macromolecules, 2007.40: p.278.
[30] S. M. Cho, Y. J. Kim, Y. S. Kim, Y. Yang, and S.-C. Ha. The application of carbon nanotube—polymer composite as gas sensing materials. Proceedings of IEEE Sensors, vol. 2, pp. 701–704, 2004.
[31] J. K. Abraham, B. Philip, A. Witchurch, V. K. Varadan, and C. Channa Reddy. A compact wireless gas sensor using a carbon nanotube/PMMA thin film chemiresistor. Smart Materials and Structures, vol. 13, no. 5, pp. 1045–1049, 2004.
[32] Y. Wanna, N. Srisukhumbowornchai, A. Tuantranont, A. Wisitsoraat, N. Thavarungkul, and P. Singjai. The effect of carbon nanotube dispersion on CO gas sensing characteristics of polyaniline gas sensor. Journal of Nanoscience and Nanotechnology, vol. 6, no. 12, pp. 3893–3896, 2006.
[33] L. Valentini, V. Bavastrello, E. Stura, I. Armentano, C. Nicolini, and J.M. Kenny. Sensors for inorganic vapor detection based on carbon nanotubes and poly(o-anisidine) nanocomposite material. Chemical Physics Letters, vol. 383, no. 5-6, pp. 617–622, 2004.
[34] M.Wienecke, M.-C. Bunescu, M. Pietrzak, K. Deistung, and P. Fedtke. PTFE membrane electrodes with increased sensitivity for gas sensor applications. Synthetic Metals, vol. 138, no. 1-2, pp. 165–171, 2003.
[35] K.H. An, S. Y. Jeong, H. R. Hwang, and Y.H. Lee. Enhanced sensitivity of a gas sensor incorporating single-walled carbon nanotube-polypyrrole nanocomposites. Advanced Materials, vol. 16, no. 12, pp. 1005–1009, 2004.
[36] B. Philip, J. K. Abraham, and A. Chandrasekhar. Carbon nanotube/PMMA composite thin films for gas-sensing applications. Smart Materials and Structures, vol. 12, pp. 935–939, 2003.
[37] J. Li, Y. Lu, and M. Meyyappan. Nano chemical sensors with polymer-coated carbon nanotubes. IEEE Sensors Journal, vol. 6, no. 5, pp. 1047–1051, 2006.

[38] A. Linford. Flow measurement and Meters. E.&F. N. Spon Ltd., London,.1949, pp. 69-177.
[39] N. Brook. Flow measurement of Solid-liquid mixtures using Venturi and other Meters. Hydraulic Plant and Machinery Group. Vol. 176, No. 6, pp. 127-140, 1962.
[40] O. Wigertz. A low-resistance flow meter for wide-range ventilatory measurement. Respiration Physiology. vol. 7, issue 2, pp. 263–270, August 1969.
[41] J. H. Preston. The three-quarter radius pitot tube flow meter. The Engineer. vol. 190, pp. 400-403, 1950.
[42] Roger C. Baker. Flow Measurement Handbook – Industrial Designs, Operating Principles, Performance, And Applications. Cambridge University Press. 2000, pp.428-431.
[43] Kazumitsu Nukui, Tatsuya Funaki, Kenji Kawashima, Toshiharu Kagawa. A study of Characteristics of Pitot Type Flow Meter. SICE 2003 Annual Conference. 2003, Fukui, Japan, pp. 846-849.
[44] M. Ashauer, H. Glosch, F. Hedrich, N. Hey, H. Sandmaier and W. Lang. Thermal flow sensor for liquids and gases based on combinations of two principles. Sensors and Actuators A: Physical. vol. 73, issue 1-2, pp. 7-13, 9 March 1999.
[45] G.N. Stemme. A monolithic gas flow sensor with polyimide as thermal insulator. IEEE transactions on Electron Devices. Vol. 33, Issue 10, pp.1470-1474, 1986.
[46] N.T. Nguyen, X.Y. Huang and K.C. Toh. Thermal flow sensor for ultra-low velocities based on printed circuit board technology. Measurement Science and Technology. Vol. 12, No. 12, pp. 2131-2136, 2001.
[47] E.G. Richardson. Hot-wire Anemometers. Journal of Scientific Instruments. Vol. 3, No. 9, pp. 323, 1926.
[48] M. Elwenspoek. Thermal flow micro sensors. Proceedings of 1999 International Semiconductor Conference. Sinaia, Romania, 1999, pp. 423-435.
[49] H.F. Stegall, R.F. Rushmer and D.W. Baker. A transcutaneous ultrasonic blood-velocity meter. Journal of Applied Physiology. Vol. 21, No. 2, pp. 707-711, 1966.
[50] C. Buess, P. Pietsch, W. Guggenbuhl and E.A. Koller. Apulsed diagonal-beam ultrasonic airflow meter. Journal of Applied Physiology. Vol. 61, No. 3, pp. 1195-1199, 1986.
[51] Richard S. Figliola and Donald E. Beasley. Theory and Design for Mechanical Measurements. 4th ed., John Wiley & Sons, New York, 2006, pp. 412-413.
[52] B.J. Chung, A. M. Robertson, and D.G. Peters. The numerical design of a parallel plate flow chamber for investigation of endothelial cell response to shear stress. Computational Structure. vol. 81, pp.535–546, May 2003.
[53] C.S. Yih. Fluid Mechanics, rev. ed. Ann Arbor, MI: West River Press, 1979.
[54] Lifeng Qin, Zijing Zeng, Hongbin Cheng and Qing-ming Wang. Acoustic wave flow sensor using quartz thickness shear mode resonator. IEEE Transactions on Ultrasonics, Ferroelectrics and Frequency Control. vol. 56, issue 9, pp. 1945-1954, September 2009.
[55] Haekwan Oh, Weng Wang, Keekeun Lee, Ikmo Park, and Sang Sik Yang. Sensitivity Improvement of Wireless Pressure Sensor By Incorporating A SAW Reflective Delay Line. Intl. J. on Smart Sensing and Intelligent Systems. vol. 1, pp. 940–954, Dec. 2008.
[56] Yu.N. Vlassov, A.S. Kozlov, N.S. Pashchin and I.B. Yakovkin. Precision SAW pressure

Sensors. Proceedings of 1993 IEEE international Frequency Control Symposium. Salt Lake City, USA, 1993, pp. 665-669.
[57] Q. Jiang, X.M. Yang, H.G. Zhou and J.S. Yang. Analysis of surface acoustic wave pressure sensors. Sensors and Actuators A. Vol. 118, Issue 1, pp. 1-5, 2005.
[58] H. Trang, R. Patrice, V. Marie-Helene, D. Jean-Sebastien, R. Philippe, B. Philippe and L. Pierre. Temperature Compensated Structure For Saw Pressure Sensor In Very High Temperature. IEEE Frequency Control Symposium, Joint with the 21st European Frequency and Time Forum. 2007, pp. 40-44.
[59] H.F. Tiersten. Perturbation theory for linear electroelastic equations for small fields superposed on a bias. Journal of Acoustic Soc. Am.. Vol.64, pp. 832–837, 1978.
[60] H.F. Tiersten, B.K. Sinha. A perturbation analysis of the attenuation and dispersion of surface waves. Journal of Applied Physics. Vol.49, pp. 87–95, 1978.
[61] M. Jungwirth, H. Scherr and R. Weigel. Micromechanical precision pressure sensor incorporating SAW delay lines. Acta Mechanica. Vol.158, No.3-4, pp.227-252, 2002.
[62] D.E. Cullen and T.M. Reeder. Measurement of SAW velocity versus Strain for YX and ST Quartz. Proceedings of IEEE 1975 Ultrasonics Symposium. Los Angeles, USA, 1975, pp.519-922.
[63] A.J. Ricco, S.J. Martin, and T.E. Zipperian. Sensors and Actuators 8, 319 (1985).
[64] Zdravko P. Khlebarov, Any I. Stoyanova, and Diana I. Topalova. Sensors and Actuators B. 8, 33 (1992).
[65] Hank Wohltjen. Sensors and Actuators 5 (4), 307 (1984).
[66] M. Bessonov and V. Zubkov. Polyamic Acids and Polyimides: Synthesis, Transformations, and Structure. (CRC, 1993).
[67] Kiril L. Levine and Jude O. Iroh. Journal of Porous Materials 11, 87 (2004).
[68] S. Iijima. Nature 354, 56 (1991).
[69] Jing Li, Yijiang Lu, Qi Ye, Martin Cinke, Jie Han, and M. Meyyappan. Nano Letters 3 (7), 929 (2003).
[70] David S. McLachlan, Cosmas Chiteme, Cheol Park, Kristopher E. Wise, Sharon E. Lowther, Peter T. Lillehel, Emilie J. Siochi, and Joycelyn S. Harrison. Journal of Polymer Science B. 43, 3273 (2005)..
[71] Sujay Deshmukh. TAMU. 2006.
[72] Siu-Ming Yuen, Chen-Chi M. Ma, Chin-Lung Chiang, and Chih-Chun Teng. Journal of Nanomaterials, 15 (2008).
[73] http://en.wikipedia.org/wiki/Percolation_threshold
[74] Kum-Pyo Yoo, Lee-Taek Lim, Nam-Ki Min, Myung Jin Lee, Chul Jin Lee, and Chan-Won Park. Sensors and Actuators B. 145, 120 (2010).
[75] http://hyperphysics.phy-astr.gsu.edu/hbase/tables/thexp.html#c1
[76] F. Pignatiello, M. De Rosa, P. Ferraro, S. Grilli, P. De Natale, A. Arie, S. De Nicola. Measurement of the thermal expansion coefficients of ferroelectric crystals by a moire interferometer. Optics Communications. Vol 277 (2007), pp.14–18.
[77] M.Bessonov, V.Zubkov, Polyamic Acids and Polyimides: Synthesis, Transformations, and

Structure. CRC, Florida, 1993.
[78] N.Hu, Y.Karube, M.Arai, T.Watanabe, C.Yan, Y.Li, Y.Liu, H.Fukunaga, Tunneling effect in a polymer/carbon nanotube nanocomposite strain sensor, Carbon N.Y. 48(2010)2929-2936.
[79] Antonio J. Ricco and Stephen J. Martin. Thin metal film characterization and chemical sensors: monitoring electronic conductivity, mass loading and mechanical properties with surface acoustic wave devices. Thin Solid Films. Vol. 206, pp94-101. 1991.
[80] A.J. Ricco, S.J. Martin, T.E. Zipperian. Surface acoustic wave gas sensor based on film conductivity changes.Sensors and Actuators.Volume 8, Issue 4, December 1985, pp.319-333.
[81] http://en.wikipedia.org/wiki/RF_MEMS
[82] F. J. O. Rodrigues, L. M. Gonçalves, P. M. Mendes. Electrically Small and Efficient On-Chip MEMS Antenna for Biomedical Devices. 2010 International Workshop on Antenna Technology (iWAT).Lisbon, Portugal.pp.1-4. 1-3 March 2010.
[83] Keat Ghee Ong, Kefeng Zeng, and Craig A. Grimes.A Wireless, Passive Carbon Nanotube-Based Gas Sensor.IEEE SENSORS JOURNAL. VOL. 2, NO. 2, pp.82-88. APRIL 2002
[84] Wen Wang, Chunbae Lim, Keekeun Lee, Sangsik Yang.Wireless surface acoustic wave chemical sensor for simultaneous measurement of CO_2 and humidity. J. Micro/Nanolith. MEMS MOEMS. Vol.8(3),pp.031306.1-6. Jul–Sep 2009.